Optical Profile and Nanostructure Effects in the Charge Carrier Transport and Performance of Photovoltaic Devices

Yingchi Liu

A dissertation submitted to the faculty of the University of North Carolina at Chapel Hill in partial fulfillment of the requirements for the degree of Doctor of Philosophy in the Department of Physics and Astronomy.

Chapel Hill
2013

Approved by

Dr. Rene Lopez

Dr. Edward T. Samulski

Dr. J. Christopher Clemens

Dr. Wei You

Dr. Alfred Kleinhammes

ABSTRACT

YINGCHI LIU: Optical Profile and Nanostructure Effects in the Charge Carrier Transport and Performance of Photovoltaic Devices
(Under the direction of Prof. Rene Lopez)

Charge carrier plays a significant role in energy harvesting in photovoltaic devices. Due to recombination, the inadequate charge carrier transport length prevents the devices from achieving efficient absorption by increasing active layer thickness. Fundamental research on the charge transport is important as it is a critical factor to determine the optimal device structures. In this thesis, the charge carrier transport process is studied in photovoltaic devices by linking local characteristic light absorption profiles to photocurrent measurements. Local light absorption profile can be approximated as the free charge generation profile, which determines the average charge transport distance. Together with incident light wavelength, illumination direction effectively controls the generation profile and hence the charge transport distance. And this charge transport distance is demonstrated to relate to recombination that can be measured from photocurrent. Therefore, the charge carrier transport length can be estimated.

On the other hand, the potential of the nanostructured solar cells as a key to solve the problem lies between adequate light absorption and efficient charge carrier collection. In this thesis, the discussion focuses on the nanostructured bulk heterojunction (BHJ) organic photovoltaics (OPVs). As photonic crystal nanostructures have been proposed to

increase the light trapping effects without increasing the volumes of the active materials, intuitively, it is believed that the nanostructure will affect only the optical absorption. However, in this thesis it is demonstrated that there is a tradeoff between light trapping enhancement and charge carrier collection deterioration due to the nanopatterning effects. Furthermore, the nanopatterning process is shown to affect the material composition in BHJ OPVs as well. Improvement of BHJ OPVs' performance by nanostructures is not a simple task of increasing light absorption. Comprehensive considerations are demonstrated necessary for design of optimal device structures.

ACKNOWLEDGEMENT

First and foremost, I would like to thank Prof. Rene Lopez and Prof. Edward Samulski for their guidance during my time as a graduate student. They have offered countless suggestions and comments regarding my experiments, presentations, and manuscripts since I began research on solar cells in the summer of 2009. They provided me great recourses and a free atmosphere where I could develop intellectually on my own. Especially, I want to express my sincere gratitude to Prof. Lopez who taught me lots of experimental skills hand by hand and offered many valuable career advices. I also would like to thank my committee members, Prof. Clemens, Prof. Kleinhammes, Prof. Qin and Prof. You for being on my committee and their support.

Secondly, I sincerely appreciate the experience of working with Dr. John Tumbleston, a former graduate student in our group, who has been quite kind and helpful to me. A big part of the thesis has been published as a joint effort between us.

Finally, I thank the many people who offered contributions, help and suggestion on this work. I thank two of the former graduate students, Dr. Emily Ray and Dr. Rudresh Ghosh, for their help in the lab when I just joined the group, Carry Tippets for the hard work on running simulations, Prof. Sorin Mitran and Dr. Christoph Kirsch for the simulation program and fruitful discussions, Dr. Muki Aryal for teaching my nano-fabrication techniques, and all the other group members, Dr. Kristen Alexander, Dr.

Eugenii Donev, Dr. Abay Gadisa, Dr. Yukihiro Hara, Dr. Alibabaei Leila, and Tim Garvey for their help and discussions. The helps from Dr. Carrie Donley, Dr. Bob Geil, Dr. Amar Kumbhar and Dr. Wallace Ambrose for the assistance with CHANL equipment are greatly appreciated too.

Personally, I am very grateful to my parents for being supportive. And thanks to all my friends, especially Dr. Haijing Wang from Physics Department who helped me a lot when I just arrived UNC. I also thank Simi Wang who makes a wonderful life of mine.

Table of Contents

LIST OF TABLES

LIST OF FIGURES

LIST OF SYMBOLS AND ABBREVIATIONS

a	electron-hole pair distance
AFM	atomic force microscope (microscopy)
APCE	absorbed photon-to-electron conversion efficiency
Ag	silver
Al	aluminum
Au	gold
BHJ	bulk heterojunction
Cu_2O	Copper (I) oxide
d	layer thickness
D_e	electron transport distance
D_h	hole transport distance
E_g	band gap
EQE	external quantum efficiency
IPCE	incident photon-to-electron conversion efficiency
FF	fill factor
G	exciton (electron-hole pair) generation rate
GIWAXS	grazing incidence wide angle X-ray scattering
HOMO	highest occupied molecular orbital
HTL	hole transport layer
IQE	internal quantum efficiency
ITO	indium tin oxide
J_{dark}	dark current
J_{light}	light current
$J_{n(p)}$	electron or hole current
J_{photo}	photocurrent density
J_s	reverse saturation current density

J_{sat}	saturated photocurrent density
J_{sc}	Short circuit current density
k	extinction coefficient
k_B	Boltzmann constant
L	diffusion length
LUMO	lowest unoccupied molecular orbital
MDMO-PPV	poly(2-methoxy-5-(3'-7'-dimethyloctyloxy)-1,4-phenylenevinylene
n	electron density
NEXAFS	near edge X-ray absorption fine structure
NIL	nanoimprint lithography
OPV	organic photovoltaic
p	hole density
P	probability of electron-hole pair dissociation
P3HT	poly(3-hexylthiophene)
PBHJ	parallel bulk heterojunction
PbS	lead (II) sulfate
PC	photonic crystal
$PC_{60}BM$	phenyl-C61-butyric acid methyl ester
$PC_{70}BM$	phenyl-C71-butyric acid methyl ester
PCDTBT	poly((9-(1-octylnonyl)-9H-carbazole-2,7-diyl)-2,5-thiophenediyl-2,1,3-benzothiadiazole-4,7-diyl-2,5-thiophenediyl)
PCE	power conversion efficiency
PEDOT:PSS	poly(3,4-ethylenedioxythiophene):poly(styrenesulfonate)
PFN	poly [(9,9-bis(3 ´-(N,N-dimethylamino) propyl)-2,7-fluorene)-alt-2,7-(9,9–dioctylfluorene)]
PFPE	perfluoropolyether
PLD	pulsed laser deposition
P_{light}	incident light intensity

PTB7	Poly[[4,8-bis[(2-ethylhexyl)oxy]benzo[1,2-b:4,5-b']dithiophene-2,6-diyl][3-fluoro-2-[(2-ethylhexyl)carbonyl]thieno[3,4-b]thiophenediyl]]
PV	photovoltaic
q	elementary charge
R	Recombination Rate
R_{sh}	shunt resistance
R_s	series resistance
SCLC	space charge limited current
SEM	scanning electron microscopy
STXM	scanning transmission x-ray microscopy
T	absolute temperature
TCO	transparent conducting oxide
t_R	recombination time
t_{sw}	sweep-out time
U	net generation rate
V	Voltage
V_0	the applied voltage at $J_{photo} = 0$
V_{app}	applied voltage
V_{mp}	voltage at maxim power point
V_{oc}	open circuit voltage
x	depth
XRD	X-ray diffraction
w	depletion width
WO_3	tungsten trioxide
α	monochromatic absorption coefficient
λ	wavelength
η	charge collection efficiency
η_{BR}	bimolecular recombination efficiency

μ	mobility
τ	lifetime
φ	the flux of incident photons
ψ	electric potential

CHAPTER 1
INTRODUCTION

1.1 Motivation: World's Energy Needs

Fossil gas and oil currently constitute our principal sources of energy worldwide. Their rising costs and finite abundance have driven interest in renewable alternatives since the 1970s. Despite recent development in shell gas extraction, the interest in alternative energy has kept growing as the emissions of burning fossil fuels such as carbon dioxide and other green-house gases have been extensively associated with a large number of undesirable environmental and climatic consequences. Taking all new developments and policies into account, the world is clearly failing to put the global energy system onto a sustainable path.[1] The search for alternative energy sources is more pressing than ever.

Solar energy is simply the most abundant and clean resource the world has. This has long motivated research in photovoltaic and photo-electrochemical technologies. Photovoltaic devices convert solar radiation directly to usable electrical energy when hit by light. The power conversion efficiency (PCE) of these devices has improved to > 25% level in industrial application[2] by using crystalline semiconductor materials such as silicon and gallium arsenide. However, the primary limitation of photovoltaics is their relatively high cost compared to fossil fuels. Even a device that operated at near the

theoretical limit of efficiency would not provide the needed technology unless it is cost-effective.[3] This conundrum has led to research not only on improvements in efficiencies of current solar cells, but also on alternative photovoltaic material and thin film technologies that seek to reduce the cost of solar cells production and installation. Promising photovoltaic inorganic compounds, such as copper (I) oxide (Cu_2O) and lead (II) sulfate (PbS), were proposed to meet the cost-effective requirement based on their electricity production potential and minimum cost per watt of electricity.[4] Another avenue to lower the cost of photovoltaic devices is the development of semiconducting and conducting organic polymers that can be processed from solution, hence the possibility of simple roll-to-roll printing processes, leading to inexpensive, large scale production.[3,5] In addition, the organic photovoltaic (OPV) could be beneficial for the applications where mechanical flexibility and disposability are important.[3]

In this thesis, the discussion will focus on the charge transport issues and device architectures in two types of the promising photovoltaic systems: Cu_2O and organic photovoltaics. It is organized in the following way: in the rest of this chapter, we will discuss the progress of Cu_2O and organic photovoltaic devices, fundamental physics and characterization of solar cells, importance of charge carrier transport and nanostructures application; in chapter 2 we will go in depth into the relationship between charge carrier transport and carrier collection and applications of absorption profiles in characterizing these properties. Chapter 3 will deal with optical, electrical and morphological effects due to patterning in nanostructured OPVs. The thesis ends with conclusions on what we have learned about these materials and the potential of alternative materials in general to become a substantial contributor to our clean energy supply.

1.2 Potential Novel Photovoltaic Materials

1.2.1 Copper (I) oxide (Cu_2O)

In recent years, the need for sustainable energy technologies with increasing emphasis placed on balancing cost and performance invigorated a renewal of interest in solar cells based on copper (I) oxide (Cu_2O) as the active layer because this semiconductor shows many important characteristics useful for solar cells production. These include low raw material cost, a direct energy gap (~2.1eV), nontoxicity, long term stability, and it is amenable to low cost scalable fabrication process such as electrodeposition.[6] However, the fundamental limitations of Cu_2O, one of the earliest semiconductors to be studied, have not been overcome. In particular, the difficulty of fabricating n-type Cu_2O, homojunctions remains a barrier to the realization of Cu_2O based solar cells. More recently transparent conducting oxide (TCO)/Cu_2O heterojunction solar cells have been pursued, especially the ZnO/Cu_2O solar cells. Although the theoretical limit of the power conversion efficiency of Cu_2O based solar cell is about 18%,[7] the highest efficiency of ZnO/Cu_2O device reported is 1.28%.[6] An inadequate minority carrier transport length has been implicated as an important factor behind this poor performance.[8–10]

1.2.2 Organic Photovoltaic Device

The polymers can be doped to have electrical properties which range from insulating to metallic and retain the flexibility as plastic materials. The first modern organic photovoltaic (OPV) device is attributed to C.W. Tang.[11] It consisted of a bilayer of hole conducting copper phthalocyanine and an electron transporting perylene tetracarboxylic derivative. The PCEs of the reported devices were around 1%. Ten years later, the concept of bulk heterojunction (BHJ) was introduced, which is a mix of donor and

acceptor materials in solution. This revolutionary idea circumvented the short exaction (electron and hole pair) diffusion length with distributed donor/acceptor interfaces throughout the BHJ layer.[12,13] Moreover, it allows solution processing of active layer instead of thermal evaporation under vacuum, which makes mass productions much cheaper. These results jumpstarted expansive research and inspired the possibility of making solar cells using simple processing techniques from plastic, lightweight, and flexible materials. By 2005, with the development of materials and processing techniques, the PCE had risen to 4.4%, using an electron donor polymer, poly-3-hexylthiophene (P3HT), and electron acceptor molecule, phenyl-C61-butyric acid methyl ester ($PC_{60}BM$).[14] Today, this material system are the most studied and well-understood BHJ solar cell system. But, device performance did not stop there as efficiency has been improved to > 9% by 2012.[15] Besides the fast development of OPV materials, characterizations of the photon absorption, free charge generation and charge carrier collection process have also drawn great attentions.[16–20] These boost development of the characterization techniques to study new materials emerging and guide material engineering towards desired features to reach high efficiencies as well.

1.3 Light Absorption and charge generation in Solar Cells

Semiconductors are characterized by a band gap, E_g. E_g is the difference between valence and conduction bands of inorganic semiconductors, while it is the difference between the highest occupied molecular orbital (HOMO) and lowest unoccupied molecular orbital (LUMO). Note that in a disordered system, like an organic solar cell, the band gap will not be a rigorously defined quantity due to the Gaussian density of states of both the acceptor and the donor materials.[21] Photons with energy above E_g can

be absorbed when light hitting the material thereby promoting electrons from valence band to conduction band or from HOMO to LUMO. Excited electron will relax either non-radioactively or by emitting a photon with energy of E_g. An electric field or gradient in carrier concentration will help to extract the current in the device.

Formally, the complex index of refraction is denoted by $\hat{n} = n + ik$, where n is the refraction index and k is the extinction coefficient. The absorption coefficient at a given wavelength λ of the material is $\alpha_{abs} = \frac{4\pi k}{\lambda}$. k will be zero at wavelengths where the energy above E_g and hence the α_{abs} is zero there. For a single thick absorbing material like Cu_2O, the profile of absorption of photons or generation rate of excitons follows a function of the depth (x) in the film which is given by $G(x) = \varphi(1-R)\alpha e^{-\alpha x}$, where φ is the number of incident photons in unit area and R is reflection. However, for thin film organic device, the film thickness is thinner than optical depth and the layer of interest is sandwiched by electrode layers so thin film interference plays a significant role in light absorption. Reflection and transmission happen at each material interface, which results in a wavelength-dependent compound effect of constructive and destructive interferences. The light absorption profile deviates from simple exponential dependence (see Fig. 1.1).

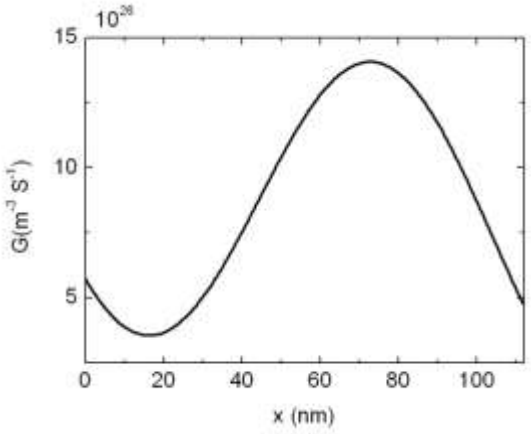

Figure 1.1 Example of light absorption/charge generation profile of a 112 nm thick P3HT:$PC_{60}BM$ blend layer in a working device with full electrodes.

After a photon is absorbed, an excited state is generated, which is an electron and hole pair. In most of the inorganic solar cells, such as Si and Cu_2O,[22] this electron and hole pair or exciton breaks by the thermal vibration because its binding energy is usually small compared to k_BT at room temperature, where k_B is Boltzman constant and T is absolute temperature. Therefore, after absorption, free carrier is generated. Cu_2O is a p-type semiconductor where the hole is dominant and easy to move. Hence, the charge collection mainly depends on the minority carrier, the electron.

The situation is more complicated in BHJ OPVs. The exciton's binding energy is large compared to k_BT. The electron and hole pair will not break right away. There are different models that exist to explain the free carrier generation and collection in BHJ OPV devices. One of the most established and well accepted models is presented by Koster et al. in 2005.[21] The model describes the OPV device by the metal-insulator-metal picture. In this picture, the device comprises of one semiconductor with LUMO of the acceptor and HOMO of the donor as the conduction and valence bands. After a photon is

absorbed, an exiton is created. The exciton dissociates across the donor-acceptor interface and yields a bound electron-hole pair. The dissociation of this bound electron-hole pair generates free charge carriers. The dissociation of exciton is driven by the difference between the LUMO levels of the two materials, which is assumed to be field independent, while the bounded electron-hole pair's dissociation is considered as field and temperature dependent because it is metastable (up to milliseconds at 80 K).[21]

In Koster's model,[21] the generation of free carriers was explained by geminate recombination theory of Onsager[23] with the refinement by Braun[24]. The bound electron-hole pair may dissociate into free carriers or decay to the ground state with a decay rate k_f. And the dissociation with a rate k_{diss} is competing with recombination rate R. In Braun's model, the probability of electron-hole pair dissociation is given by $P(a,T,F) = \frac{k_{diss}(a,T,F)}{k_{diss}(a,T,F) + k_f(T)}$, where a is electron-hole pair distance and F is electric field strength. The recombination is considered as bimolecular recombination and with rate $R = \gamma(np - n_{\text{int}}^2)$. γ is the recombination strength and $n_{\text{int}} = N_c \exp(-E_{gap} / 2V_t)$, where $V_t = k_B T/q$ and q is the elementary charge. The whole progress from absorption of photons to sweep-out of free carriers is described in Fig. 1.2.

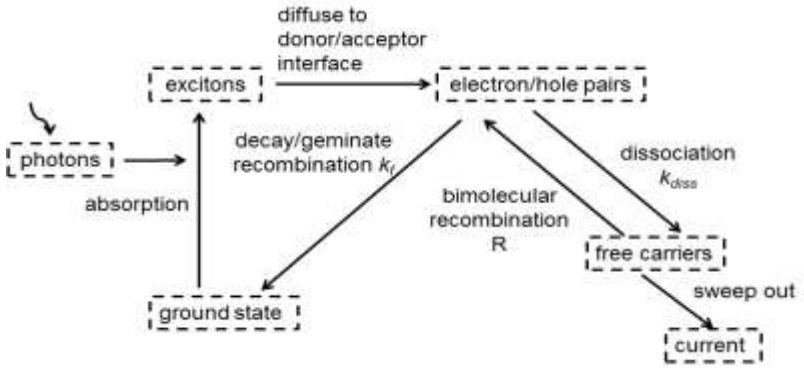

Figure 1.2 Progress from absorption of photons to generation of free carriers. Upon absorption, excitons are created and diffuse to the donor/acceptor interface where the electrons are transferred to the acceptor and bound electron-hole pairs are formed. The bound pair may either dissociate and become free carriers or decay to the ground state. The dissociation also competes with recombination.[21]

Recent years, there has been an intense argument about the field dependency of free charge carrier generation in BHJ OPVs. In 2012, Heeger group propose a new mechanism of charge generation.[19] Previous femtosecond transient absorption studies have demonstrated that the appearance of charges faster than the 100–200 fs time resolution of the experiments in polymer:fullerene blends with optimized composition and morphology.[25–31] Admitting the fact that charge transfer occurs within 100 fs or even less, exciton diffusion to the polymer/fullerene interface also happens within the same time scale. This limits the distance of exciton diffusion to 0.1~0.2 nm, according to published exciton diffusion coefficients.[32,33] However, the typical length scale is estimated to be about 10 ~ 20 nm in optimized bulk heterojunctions by structural characterization in optimized morphologies.[34–39] Besides, experimental observation demonstrated that nanoscale (~10 nm, not less) phase separation is necessary for efficient bulk heterojunction photovoltaics.[40,41] Thereby, the distance that an exciton can diffuse is much shorter than the distance that it needs to diffuse for charge separation at the

interface in 100 fs. This is in contrast with the previous picture of bound excition formation upon photon absorption. Heeger group then proposed an alternative picture of free carrier generation that the delocalized and/or mobile electrons and holes are formed directly in the conduction and valence bands after the interband absorption rather than the relaxed excitons which are localized by structural relaxation of the polymer and bound by the Coulomb interaction. Hence, the primary excitation can reach the interface faster than an exciton, which could account for the ultrafast charge separation. The charge separation does not rely on electric field or other thermal vibration because there is excess energy in the system. Therefore, they suggested it is very possible that charge transfer from the polymer to the fullerene directly yields free charge carriers. Recombination in BHJ solar cells should be bimolecular or trap-based, instead of geminate.

1.4 Equations of Charge Carrier Collection

After the exciton or electron-hole pair separates, excess charges are created in the polymer and fullerene domains due to photoexcitation and subsequent charge transfer, as discussed in the previous section. Mobile (free) carriers must then be generated and collected at opposite electrodes prior to recombination. Despite the argument of free carrier generation, the free carrier collection process can be described by basic equations below:

$$\frac{\partial^2}{\partial x^2}\psi(x) = \frac{q}{\varepsilon}[n(x) - p(x)] \tag{1.1}$$

where ε is the dielectric constant. This equation relates the potential $\psi(x)$ to the electron and hole densities $n(x)$ and $p(x)$. Another set of equations are the current continuity equations

$$\frac{\partial}{\partial x} J_n(x) = qU(x) \tag{1.2}$$

$$\frac{\partial}{\partial x} J_p(x) = -qU(x) \tag{1.3}$$

where $J_{n(p)}(x)$ is the electron (hole) current density and $U(x)$ is the net generation rate, i.e., the difference between generation of free carriers and recombination of free carriers.

In order to solve those basic equations, a set of equations is needed to relate the current densities to the carrier densities and the potential. Incorporating both drift and diffusion of charge carriers, one has

$$J_n = -qn\mu_n \frac{\partial}{\partial x}\psi + qD_n \frac{\partial}{\partial x} n \tag{1.4}$$

$$J_p = -qn\mu_p \frac{\partial}{\partial x}\psi - qD_p \frac{\partial}{\partial x} p \tag{1.5}$$

where $D_{n,p}$ are the carrier diffusion coefficients, which are assumed to obey the Einstein relation[21]

$$D_{n,p} = \mu_{n,p} k_B T / q \tag{1.6}$$

1.5 Basic Characterization of Solar Cell Devices

1.5.1 J-V measurement and Power Conversion Efficiency

When a solar cell is illuminated with light and placed under short-circuit (i.e. applied voltage (V_{app}) = 0 V), photocurrent is produced in the external circuit. This point is labeled as the short-circuit current (J_{sc}) on the standard current density vs. voltage (J-V) measurement (Fig. 1.3). An internal electric field points from cathode to anode under short-circuit conditions due to the energy level difference of the electrodes, which drives photocurrent extraction. Typically, the current density can be further increased by

applying negative bias across the device that raises the internal electric field strength. If the current under illumination (J_{light}) is subtracted from the current in the dark (J_{dark}), then this amount, the photocurrent (J_{photo}), will saturate to a level proportional to the amount of light absorbed in the BHJ layer. As V_{app} is increased to positive bias, then the extraction of carriers decreases in part due to a decrease in the internal field, but also due to increased injection of holes from the anode and electrons from the cathode (i.e. J_{dark}). Under open-circuit conditions, the internal field is very weak and $J_{light} = 0$. With even more application of bias, the current increases rapidly until it becomes linear with a slope controlled by the series resistance (R_{sr}) of the device. The power conversion efficiency (PCE) of the solar cell is calculated as

$$\text{PCE}=\frac{J_{sc}\cdot V_{oc}\cdot FF}{I_{1sun}} \tag{1.7}$$

where the AM 1.5 solar power 1 sun=100 mW/cm^2 and FF is fill factor which is defined as,

$$FF=\frac{J_{MPP}\cdot V_{MPP}}{J_{sc}\cdot V_{oc}} \tag{1.8}$$

The J_{mpp} and V_{mpp} are the current density and voltage at maxim power point, respectively.

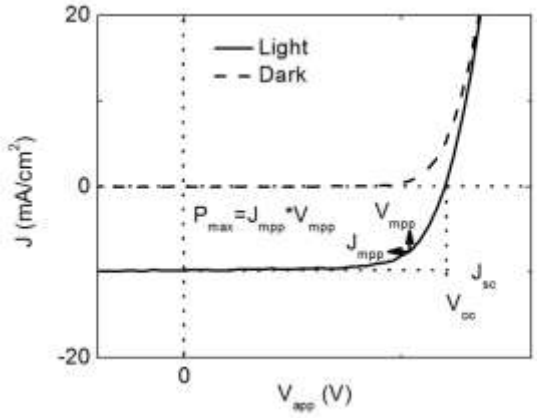

Figure 1.3 J-V under dark and illumination of one solar cell device.

1.5.2 Quantum Efficiencies

A solar cell's quantum efficiency (QE) value indicates the amount of current that the cell will produce when irradiated by photons of a particular wavelength. If the cell's quantum efficiency is integrated over the whole solar electromagnetic spectrum, one can evaluate the amount of current that the cell will produce when exposed to sunlight. The ratio between this energy-production value and the highest possible energy-production value for the cell (i.e., if the QE were 100% over the whole spectrum) gives the cell's overall energy conversion efficiency value. Note that in the event of multiple exciton generation, quantum efficiencies of greater than 100% may be achieved since the incident photons have more than twice the band gap energy and can create two or more electron-hole pairs per incident photon.

Two types of solar cell quantum efficiency are often considered. External Quantum Efficiency (EQE, also known as incident photon-to-electron conversion efficiency, IPCE) is the ratio of the number of charge carriers collected by the solar cell to the number of

photons of a given energy shining on the solar cell from outside (incident photons). It is defined as

$$EQE = \frac{electrons/\sec}{photons/\sec} = \frac{J_{photo}}{P_{light}} \times \frac{h\,\lambda}{q\,c} \tag{1.9}$$

where P_{light} is incident light intensity, h is plank constant and c is light speed.

Internal Quantum Efficiency (IQE, also known as Absorbed photon-to-electron conversion efficiency, APCE) is the ratio of the number of charge carriers collected by the solar cell to the number of photons of a given energy that shine on the solar cell and are absorbed by the cell. The IQE is always larger than the EQE. A low IQE indicates that the active layer of the solar cell is unable to make good use of the photons. To measure the IQE, one first measures the EQE of the solar device, then measures its transmission and reflection, and combines these data to infer the IQE.

1.6 Active Layer Thickness: A Trade-off

The major challenge in photovoltaic/solar cell technology dwells in achieving an efficient absorption of photons with an effective carrier extraction. The vast majority of solar cells try to maximize their photon capture by simply increasing the thickness of the absorbing layer. However, in addition to rising materials cost, this is extremely detrimental to charge harvesting since carriers are more likely to recombine before reaching contact points. At different scales this problem is present in all types of solar cells. For instance, light absorption in silicon cells is very weak due to its indirect band-gap. This results in the need of a very thick active layer which has to be made of high quality (and expensive) crystalline material in order to transport the carriers over tens of microns. In the case of polymer cells, which could have an economic edge due to their

low fabrication costs, the dilemma is remarkably similar. They are strong light absorbers, capable of almost total light-absorption with a thin 200 nm layer, but their carrier mean free paths are considerably shorter. The resulting efficiency is reportedly still too low to be practical.

1.7 Nanostructure and Application

Nanostructure has been frequently applied to solve the problem that lies in the incompatible lengths scale of optical absorption and charge carrier collection.[9,10,42–50] For instance, Musselman et al. proposed ZnO nanowires to reduce the charge carrier transport distance in ZnO/Cu_2O solar cells.[9,10] Some of the others seek for optical improvement. The photonic crystal (PC) nanostructures is one of the most intensively studied techniques to increase light trapping effects which could counteract the inadequate charge carrier transport.[42–44,47,50,51] PC structuring makes full usage of light's intrinsic length scale, its wavelength, to manipulate light behavior by scattering and interference. Although this is a revolutionary concept in optical devices, nature has been employing photonic designs in many bio-structures for millions of years. The majority of insects and birds with metallic-like colorations obtain their looks using structures that have layers of alternately high and low refractive index. This leads to optical scattering and interference that enhances the coloration. For example, in iridescent blue Morpho rhetenor butterflies, ultralong-range visibility of up to half a mile is attributed to photonic structures formed by discrete multi-layers of cuticle and air.[52] In other families of nature's photonic structures, the designs result in a quite efficient light absorption system,[53] antireflection[54] and other types of light management.[55] In this thesis, the design rule will be discussed

towards nanostructures in photovoltaic devices and it will focus on the application of photonic crystal structures in OPVs.

1.8 Importance of Transport

There are two important distances in photovoltaic materials: charge carrier transport length and the charge carrier transport distance. The former length is the capability of the carriers to transport across the material. The latter is the distance that the charge carrier needs to travel to be collected. The charge carrier transport remains critical factor which determines the solar cells' efficiency, even though the nanostructures can increase the total light absorption or reduce the charge carrier transport distance. Characterization of transport length helps the design of nanostructure to achieve the efficiency enhancement. For instance, the nanowires can reduce the electron transport distance.[10] But, if a nanostructure scale less than this critical length, it will not bring additional benefits and could have a detrimental effect given the numerous potential interface defects that scale as the heterojuntion contact area increases, in itself a big concern responsible for the less than expected V_{oc}. Additionally, in nanostructured OPV devices, the changes of electric field and optical absorption profile will affect the charge carrier transport length and the charge carrier transport distance as well. Therefore, application of nanostructures in photovoltaic devices is not a simple task. Comprehensive design with consideration of optical absorption and charge carrier transport is required.

CHAPTER 2
CHARACTERIZE CHARGE CARRIER TRANSPORT BY MANIPULATING ABSORPTION PROFILE

2.1 Introduction

As discussed in the previous chapter, the local light absorption profiles are close related to charge generation profiles/distributions in all kinds of photovoltaic devices. The characteristic local light absorption profile in the photoactive layer can be utilized to control the carrier transport distance to the electrode where the carrier exits.[8,56] Regular devices are started with transparent front electrode (such as indium tin oxide, ITO) and completed with metal back electrode, such as silver (Ag), aluminum (Al) or gold (Au). Using semi-transparent back electrodes in devices allows for illumination from either side of the devices. Along with the excitation wavelengths, choice of illumination side offers the control of the local absorption profile in the photoactive layer. The profile of exciton (electron-hole pair) generation (G) from light absorption has approximately the same distribution of the profile of free carrier creation. G effectively controls the distance that carriers must travel in the active layer in order to be extracted and hence affect the collection of free carriers and photocurrent. By measuring the photocurrents under illumination from both sides, we are able to relate the experimental results to carrier transport process by using an appropriate model for each kind of devices and probe the carrier transport information such as transport length. If the free carriers generated

beyond the transport length, they are not able to be collected by electrodes. Therefore, the transport length is obliviously the factor limiting thickness of the planar active layer. In addition, the photonic crystal solar cell should be designed mindful of charge carrier transport as mentioned previously. In this thesis, minority carrier transport length in Cu_2O was probed by this method.[8] A nanostructure scale less than the critical length will not bring additional benefits and could have a detrimental effect given the numerous potential interface defects that scale as the heterojunction contact area increases. In the case of BHJ OPVs, a similar method was applied to reveal the relation between charge generation profile and the recombination mechanism, an important process during charge carrier transport. The product of mobility and lifetime of the carrier was estimated.[56] This technique were used in transient photocurrent measurements and we revealed the physical process of electron and hole transport and demonstrated the potential of measuring mobility and lifetime.

2.2 Minority Carrier Transport Length in Cu_2O/ZnO Solar Cell

To estimate the minority carrier (i.e electron) transport length in Cu_2O, the Cu_2O/ZnO device was made. ZnO film on glass substrate was prepared by pulsed laser deposition (PLD) using 99.99% purity ZnO target. To get good conductivity ZnO film with a surface receptive to Cu_2O to growth, two layers of ZnO was deposited sequently under different conditions. A ZnO layer ~200 nm thick is deposited on glass substrate at 200 ^oC with 10 mTorr O_2 and it is followed by ZnO of ~500 nm deposited at room temperature under 200 mTorr O_2. The Cu_2O layer was electrodeposited in an aqueous solution onto precoated ZnO/glass substrate. The solution contains 0.2 mol/l copper sulfate hydrate and 3 mol/l lactic acid, while the pH is adjusted to 12.5 with a 1 mol/l KOH aqueous solution.

The electrodeposition is performed with a current density of -0.9 mA/cm^2 at 40 ^{o}C. A total electric charge of 2 C/cm^2 corresponds to the film thickness of ~1.6 μm. To complete the device, a semitransparent gold layer of ~20 nm was sputtered on Cu_2O as anode contact. The whole device was later annealed on for 1 hr at 200 ^{o}C.

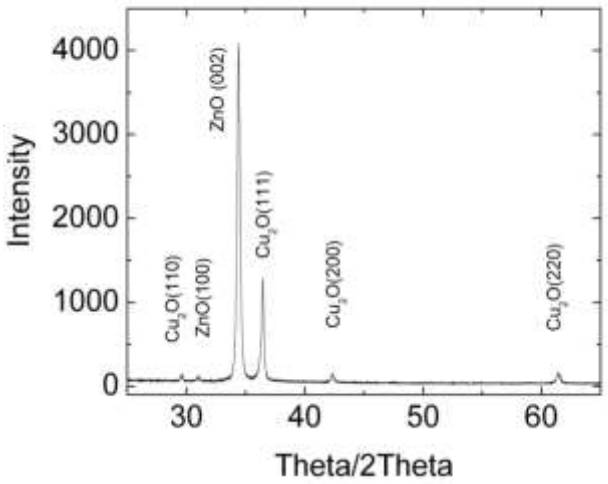

Figure 2.1 X-Ray diffraction of the ZnO/Cu_2O solar cell.

Fig. 2.1 shows X-Ray diffraction measurements which confirm only Cu_2O is formed on the ZnO without trace of CuO. A scanning electron micrograph (SEM) of the cross section of the device is shown in Fig 2 where the thickness of each layer of the device is assessed. In Figure 2.3, the solar cell has been also characterized by J-V scan, both in dark and under AM 1.5 conditions (front illumination). From where, J_{sc} = 3.16 mA/cm^2 and a V_{oc} = 0.11V are measured. The efficiency is low because of the thin gold electrode which reduced the light absorption and increased the series resistance. Fig. 2.3 shows the IPCE measurements with illumination from both back and front of the cell. The J_{sc} of 3.49 mA/cm^2 calculated from the IPCE with front illumination is consistent with our J-V measurement.

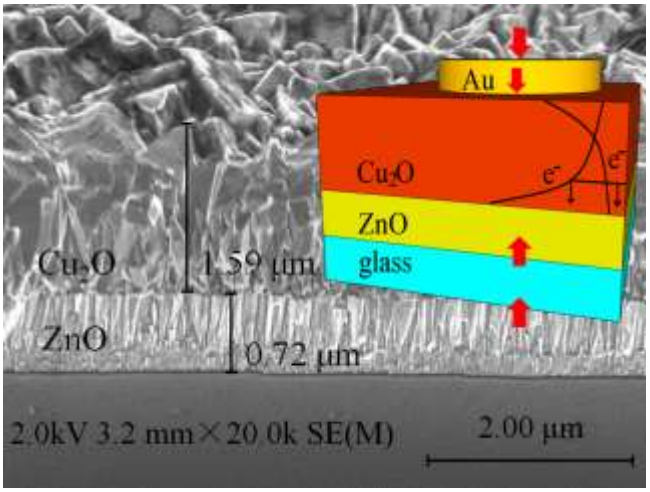

Figure 2.2 Cross-sectional SEM (45 °tilt) of the ZnO/Cu2O solar cell. Inset: schematic of the complete device solar cell and electron generation profiles for front and back illumination. Reprinted with permission from Ref. 8. Copy Right 2011, American Institute of Physics.

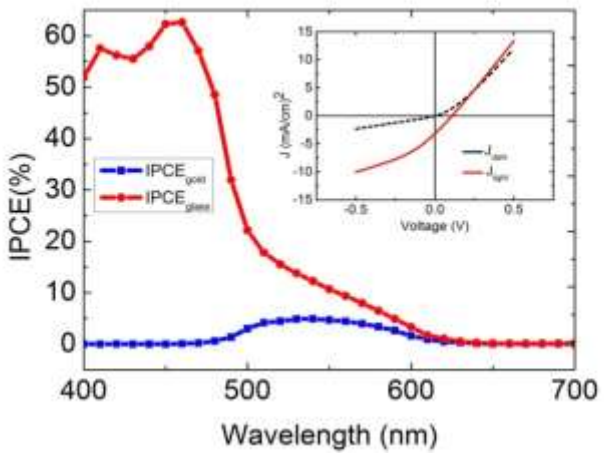

Figure 2.3 IPCE measurements with illumination from both sides. Solid circle is glass side illumination while solid square is from gold side. Inset is J-V measurement under dark and AM 1.5 conditions. Dash line is dark current and solid line is light current. Adapted with permission from Ref. 8. Copy Right 2011, American Institute of Physics.

Previously studies[22,57] estimated the electron diffusion length in Cu_2O ranging from 2 to 12μm using Gärtner's model[58] for the photocurrent density. This would be an overestimation for electrodeposited Cu_2O given the typical low photo currents obtained

in these devices. To probe the transport length in electrodeposited Cu_2O, we have modified Gärtner's model following the work of Södergren et al.[59] All of the parameters are obtained from the IPCE measurements and known optical constants.

As shown in Gärtner's model, [58] the photo current is given by,

$$J = J_{DL} + J_{DIFF} \tag{2.1}$$

where J_{DL} is the drift current density due to carriers generated inside the depletion layer, and J_{DIFF} is the diffusion current density of minority carriers generated outside the depletion layer in the bulk of Cu_2O and diffusing into the depletion region.

$$J_{DL} = q\int_0^w G(x)dx \tag{2.2}$$

where w is width of depletion layer, $x = 0$ is at the interface of ZnO and Cu_2O and q is element charge. J_{DIFF} is determined by Eq. (2.2) for the excess concentration of electrons $n(z)$.

$$D_0 \frac{\partial^2 n(x)}{\partial x^2} - \frac{n(x)}{\tau_0} + G(x) = 0 \tag{2.3}$$

The boundary conditions are $n(w) = 0$ and corresponding to a total carrier sweep and negligible electron current toward the anode, respectively.[60] d is the thickness of Cu_2O layer. This last condition is used instead of Gärtner's $n(\infty) = 0$ which is only appropriate for a bulk semiconductor and is not adequate for thin electrodeposited devices.

As discussed in previous chapter, Cu_2O film is thick and hence $G(x)$ for gold and glass sides illumination can be approximated by:

$$G_{Au}(x) = \varphi T_{Au} \alpha e^{-\alpha(d-x)} \tag{2.4}$$

$$G_{glass}(x) = \varphi T_{glass/ZnO} \alpha e^{-\alpha x} \tag{2.5}$$

φ is the flux of incident photons and is α the monochromatic absorption coefficient. Here T_{Au} and $T_{glass/ZnO}$ are the transmittance through gold and glass/ZnO to Cu_2O, respectively. They are measured independently by spectroscopic optical transmittance of the individual layers.

Solving Eq. (2.2) with *G(x)* for back and front illuminations offers the excess electron concentration in the Cu_2O film. JDIFF is proportional to the gradient of *n(z)* at $x = w$. The IPCEs (J/φ) for gold and glass sides are given by:

$$IPCE_{gold} = e^{-d\alpha}\left(-1+\frac{2e^{\frac{d+w+dL\alpha}{L}}L^2\alpha^2 + e^{w\left(\frac{2}{L}+\alpha\right)}(-1+L\alpha) - e^{\frac{2d}{L}+w\alpha}(1+L\alpha)}{(e^{\frac{2d}{L}}+e^{\frac{2w}{L}})(-1+L^2\alpha^2)}\right)T_{Au} \tag{2.6}$$

$$IPCE_{glass} = (1-\mathrm{e}^{-w\alpha} + \frac{\mathrm{e}^{-(d+w)\alpha}L\alpha(-2\mathrm{e}^{\frac{d+w+Lw\alpha}{L}}L\alpha + \mathrm{e}^{d\left(\frac{2}{L}+\alpha\right)}(-1+L\alpha) + \mathrm{e}^{\frac{2w}{L}+d\alpha}(1+L\alpha))}{(\mathrm{e}^{\frac{2d}{L}}+\mathrm{e}^{\frac{2w}{L}})(-1+L^2\alpha^2)})T_{glass/ZnO} \tag{2.7}$$

where L is the diffusion length. For long wavelengths (λ) where *α(λ)* is small (literature values[57]) and $\alpha L << 1$, one can obtain approximated expressions neglecting those small terms following the work of Lindquist et al.[61] A useful feature of this limit is that one can obtain an estimate of the depletion layer width at short circuit conditions:

$$\frac{w}{d} = \frac{IPCE_{\mathrm{glass}}}{T_{glass/ZnO}} \quad (\text{at } \lambda \text{ where } \frac{IPCE_{\mathrm{gold}}}{T_{Au}} \text{ is maximum}) \tag{2.8}$$

In our case, the $IPCE_{gold}/T_{Au}$ reaches its maximum at λ =540 nm (Fig. 2.3), where α is small6 and we can estimate w ~ 269 nm, using the film thickness (~1600 nm) obtained

from SEM (Fig. 2.2) cross section. *L* can now be assessed from the ratio of the $IPCE_{gold}$ to the $IPCE_{glass}$.

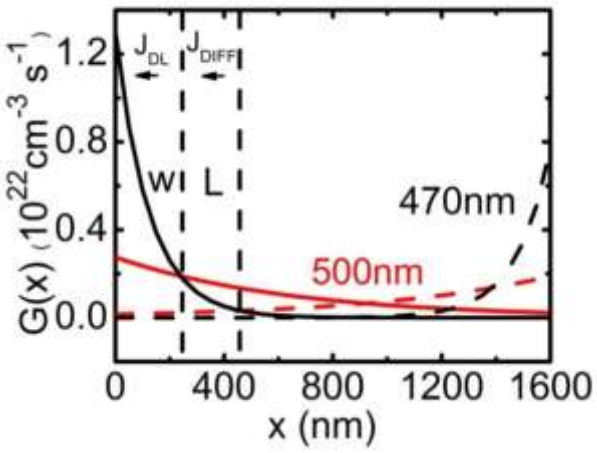

Figure 2.4 Generation profile G(x) (red λ= 500 nm, black λ = 470 nm). Solid lines are glass side illumination. Dashed lines are gold side illumination. Adapted with permission from Ref. 8. Copy Right 2011, American Institute of Physics.

In Fig. 2.5, we plot the both experimental and simulated IPCE ratios. Fig. 2.4 shows *G(x)* at 470 nm and 500 nm with illumination for both sides. As we can see, more electrons are generated close to where light enters the Cu_2O layer and the generation decays exponentially through the film. At short wavelength, α is large and the difference of generation profiles between the two illumination directions is huge. On average, only electrons within a distance $\leq L + w$ to the ZnO interface can be collected. For a relatively short *L*, at short wavelengths most electrons can reach the interface for front illumination. In contrast most carriers generated from back illumination are too far away from the interface to be collected. At long wavelengths the difference in *G(x)* becomes less significant as α gets smaller and the collection of electrons is almost independent of illumination direction. Therefore, the ratio of the IPCEs is small at short wavelengths and

increase to the ratio of incident light intensity on Cu_2O from the two illumination directions at long wavelengths. In Fig. 2.5 if *L* increases, the electron collection becomes more independent on the direction of illumination for all wavelengths, and the ratio of IPCEs is determined mainly by the ratio of transmittances. From Fig. 2.5, *L* is estimated to be ~ 160 nm. As shown, our model provides a good fit to the IPCE ratio. Therefore, only photogenerated carriers within the distance of $L+w$ (~430 nm) have a faire chance of being collected.

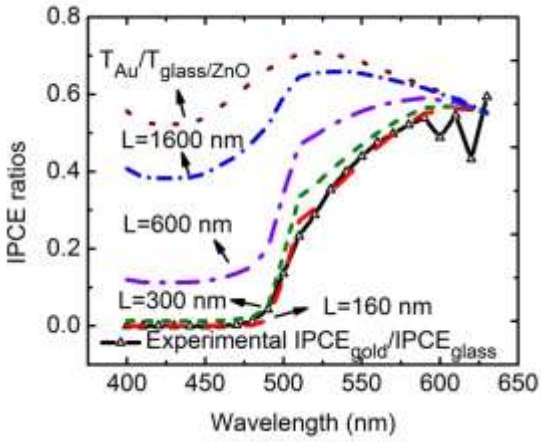

Figure 2.5 Experimental (open triangles) and simulated IPCE ratios with different proposed diffusion lengths (L = 160 nm, 300 nm, 600 nm and 1600 nm). Limit to IPCE ratio is set by the ratio of transmittances of gold to that of glass/ZnO. Adapted with permission from Ref. 8. Copy Right 2011, American Institute of Physics.

The diffusion length found here is significantly shorter at least by one order of magnitude than the values reported previously.[5,6] Moreover, when those values are applied with the classical Gärtner's model to the gold side illumination alone, they resulted in a negative $IPCE_{gold}$ at short wavelengths which is not observed experimentally. One should note that those previous diffusion lengths were obtained from studying the

IPCE of a Cu/Cu_2O solar cell which may have a different, and presumably better, crystalline structure. Nevertheless, such long *L* values would be in conflict with the low photocurrents obtained from electrodeposited Cu_2O. Furthermore, a qualitative inspection of the SEM cross section in Fig. 2.2, points to numerous microcrystalline defects that most likely should limit the free scattering path to submicron lengths.

2.3 Charge Transport and Recombination in Organic Photovoltaic Device

2.3.1 Background

The dilemma between light absorption and charge carrier collection is similar in OPVs. Organic polymers are strong light absorbers, capable of almost total light-absorption with a layer of only 200 nm, but their carrier mean free paths are considerably shorter. The resulting efficiency is reportedly still not high enough to be practical. The characterization of charge carrier transport in bulk heterojunction (BHJ) organic solar cells has been a central component to improving the power conversion efficiency (PCE). Using a suite of steady-state and transient techniques, a complex picture of the underlying physical mechanisms leading to photocurrent generation has emerged that has helped guide the design of higher performing materials and devices.[62,63] This development has been coincident with empirical evidence refining the optimal processing conditions for the ever-growing number of organic photoactive materials. One such empirical guideline is that the active layer thickness (d_{active}) must be kept on the order of 100 nm so that transport distances remains short enough to avoid free carrier recombination. However, this comes at the expense of light absorption efficiency, which generally increases with d_{active} and dictates the maximum achievable photocurrent.[64,65]

Traditionally, the loss of free carriers has been described as non-geminate (recombined electron and hole originate from different excited states) and bimolecular (second order recombination rate that depends on the square of the free carrier density).[21] While the loss of free carriers is intuitively non-geminate, bimolecular recombination can only be linked to free carrier loss if it depends on the distances that electrons and holes are required to travel to reach their respective exit contacts. While this has been inferred from comparisons of separate devices where d_{active}[66] or carrier mobilities[17,67] are varied, such comparisons may convolve unintentional morphological changes from altered processing conditions. In the recent work,[16] it was shown that an indirect link between bimolecular recombination and the distance required for carriers to transit the active layer, but again comparisons were made between different samples with different d_{active} and electron/hole transport interlayers. Finally, device models[21,68] have also predicted that increasing d_{active} will lead to greater bimolecular recombination,[69] but this effect is to be expected since free carriers are assumed to be lost only through this process. Establishing a solid experimental basis between bimolecular recombination and carrier transport distances would provide new insight to this loss mechanism that critically influences the open-circuit voltage[70,71] and also describes the dark injected current.[72]

Similarly, as applied to Cu_2O solar cell, the characteristic local generation profile in the active layer were utilized to control the carrier transport distance in semi-transparent devices. Along with the excitation wavelength, choice of illumination side (glass or Al herein) offers control of the local absorption or exciton generation rate (G) profile in the photoactive layer. The profile of exciton generation from light absorption can be assumed as approximately equal to the profile of free carrier creation (assuming ~10 nm exciton

diffusion length) that occurs after exciton diffusion and charge separation at the internal donor/acceptor interfaces. Therefore, *G* effectively controls the distance carriers must travel in the active layer in order to be extracted, which will later be related to bimolecular recombination losses. We perform this experiment to three polymer/fullerene systems, P3HT, poly(2-methoxy-5-(3'-7'-dimethyloctyloxy)-1,4-phenylenevinylene (MDMO-PPV), and poly((9-(1-octylnonyl)-9H-carbazole-2,7-diyl)-2,5-thiophenediyl-2,1,3-benzothiadiazole-4,7-diyl-2,5-thiophenediyl) (PCDTBT), each blended with $PC_{60}BM$ They cover a broad range of known morphological characteristics (e.g. polymer crystallinity), quantum efficiency, and device performance.

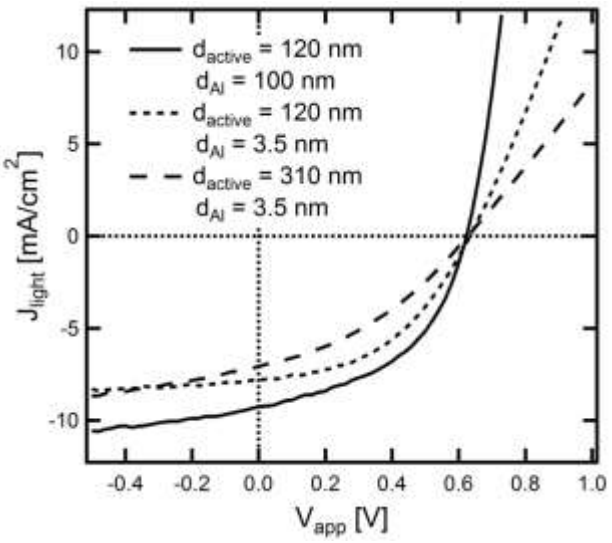

Figure 2.6 Current-voltage characteristics under 1 Sun illumination for P3HT:$PC_{60}BM$ with thin (d_{Al} = 3.5 nm) and thick (d_{Al} = 100 nm) aluminum cathodes with varying active layer thickness, d_{active}. Both the J_{sc} and FF are reduced due to a marginal drop in light absorption and increase in serial resistance, respectively, from the use of semi-transparent aluminum electrodes. The V_{oc} remains essentially unchanged. Reprinted with permission from Ref. 56 Copy Right 2012, WILEY-VCH Verlag GmbH & Co. KGaA, Weinheim.

2.3.2 Electro-optical Performance of Semi-transparent Devices

PCE under 1 Sun illumination comparable to previous reports was obtained for all three polymer/fullerene combinations using the standard device configuration of indium tin oxide (ITO)/poly(3,4-ethylenedioxythiopene):poly(styrenesulfonate) (PEDOT:PSS) / active layer/Al. In order to control the carrier transport distance, semi-transparent cathodes were employed that allow for illumination from either the glass or Al side of the device. Semi-transparent electrodes have been previously demonstrated for BHJ solar cells using non-traditional electrode materials,[73–78] but in this work, we incorporate thin layers (~5 nm) of Al. Even with such thin layers, reasonable device performance is achieved with high open-circuit voltage (V_{oc}), where the primary losses originate from a reduction in light absorption and increase in serial resistance. Each of these result in marginal drops in short-circuit current (J_{sc}) and fill factor (*FF*), respectively. Figure 2.6 shows 1 Sun device performance for P3HT:$PC_{60}BM$ devices with d_{active} = 120 nm and Al cathode thickness (d_{Al}) of 100 and 3.5 nm. The PCE drops from 2.8% to 2.2% for devices with d_{active} = 120 nm and d_{Al} = 100 nm and 3.5 nm, respectively, due to the reductions mentioned above. Also shown in Fig. 2.6 are device performances for solar cells with d_{active} = 310 nm and d_{Al} = 3.5 nm (PCE = 1.6%), where the serial resistance increases compared to devices with d_{active} = 120 nm and d_{Al} = 3.5 nm. Use of thicker active layers is critical to measurement of recombination losses as will be discussed below. Similar trends in PCE are noted for MDMO-PPV:$PC_{60}BM$ and PCDTBT:$PC_{60}BM$ solar cells (see Figure 2.7) when using thick active layers. Since the primary reductions in performance for semi-transparent devices originate from reductions in J_{sc} (due to partial transmission of incident light) and *FF* (due to increase in resistance of the contact), we presume that active layer morphology, materials properties, and interfaces are respectable for each

device configuration in spite of the drop in PCE. Furthermore, PCEs of 3.4%, 1.2%, and 4.5% were demonstrated for P3HT:$PC_{60}BM$, MDMO-PPV:$PC_{60}BM$, and PCDTBT:$PC_{60}BM$, respectively, when thin active layers were used and calcium interlayers were added between the active layer a standard, thick aluminum cathode.

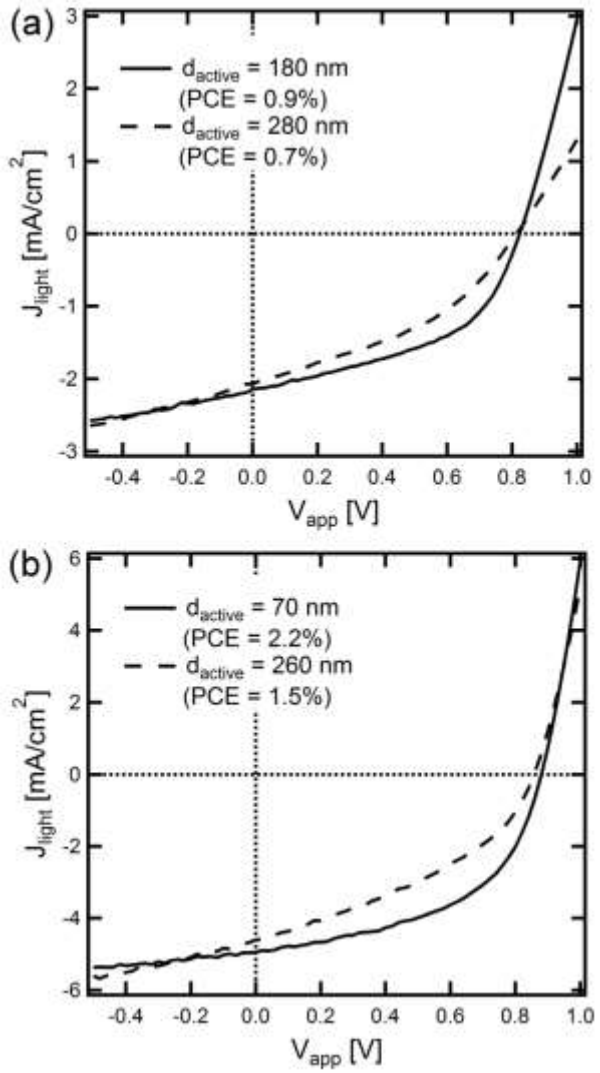

Figure 2.7 Current-voltage characteristics under 1 Sun illumination from glass side for semi-transparent devices with thin (< 10 nm) Al cathodes and (a) MDMO-PPV:$PC_{60}BM$ and (b) PCDTBT:$PC_{60}BM$ active materials with varying active layer thickness, d_{active}. For both device types (including P3HT:$PC_{60}BM$ from Figure 2.6), an increase in d_{active} causes a corresponding increase in series resistance and drop in the fill factor. Reprinted with permission from Ref. 56 Copy Right 2012, WILEY-VCH Verlag GmbH & Co. KGaA, Weinheim.

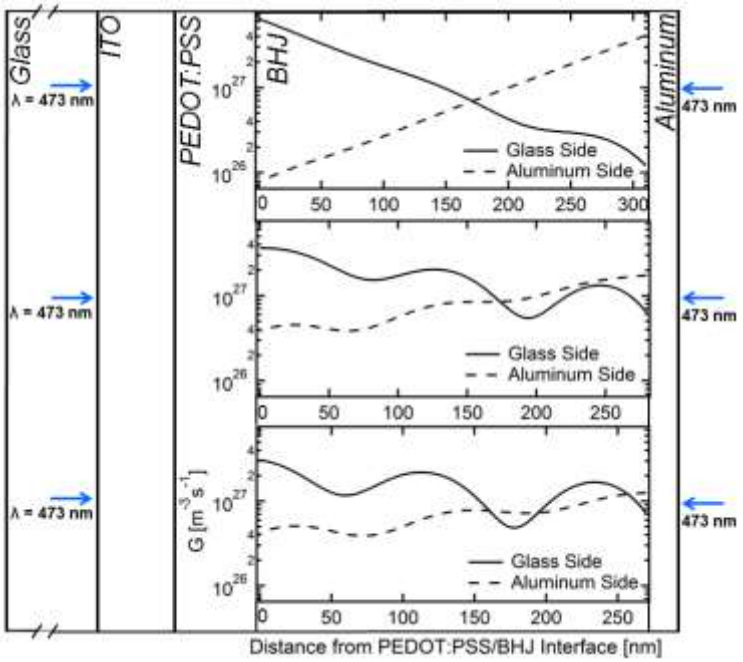

Figure 2.8 Local absorption or exciton generation rate (G) profiles in the active layer for devices with P3HT:$PC_{60}BM$ (top), MDMO-PPV:$PC_{60}BM$ (middle) and PCDTBT:$PC_{60}BM$ (bottom). For λ = 473 nm illumination, the profile is weighted more heavily close to or far from the PEDOT:PSS/BHJ interface for glass side and Al side illumination, respectively. All curves correspond to an incident intensity of 25 mW/cm^2, typical of subsequent photocurrent measurements. Reprinted with permission from Ref. 56. Copy Right 2012, WILEY-VCH Verlag GmbH & Co. KGaA, Weinheim.

2.3.3 Local Absorption Profiles and Transport Distances

As mentioned above, local absorption profiles are determined using an auxiliary optics simulation that takes into account optical interference due to subsequent reflection and transmission of light at each internal device interface. Fig. 2.8 shows *G* of the three active materials under normal incidence of λ = 473 nm excitation wavelength when illuminating from the glass or semitransparent Al side of devices. *G* drops by around an order of magnitude across the active layer when illuminating from either side in P3HT:$PC_{60}BM$ device, because of its high absorption coefficient of at this wavelength, while *G* decreases across the active layer for each illumination side but to a lesser extent

in devices with MDMO-PPV:$PC_{60}BM$ and PCDTBT:$PC_{60}BM$, due to the lower absorption coefficients of these two blends. The significant difference between absorption profiles depending on illumination side can be characterized in terms of the carrier transport distance, $D_{e,h}$, i.e. average distance from electrons and holes are created to their respective electrode to exit. For glass side illumination, $D_{e,h}$ takes the form,

$$D_h = \frac{\int_0^{d_{active}} x\,G\,dx}{\int_0^{d_{active}} G\,dx} \tag{2.9}$$

$$D_e = \frac{\int_0^{d_{active}} (d_{active} - x)\,G\,dx}{\int_0^{d_{active}} G\,dx} = d_{active} - D_h \tag{2.10}$$

Where x is the distance from the PEDOT:PSS/active layer interface. Similar expressions are used for Al side illumination.

We demonstrate the effect of both excitation wavelength and illumination side on $D_{e,h}$ in Fig. 2.9 In general, there is a larger difference in D_h when comparing glass and Al side illumination at wavelengths where the polymer blend has the largest intrinsic absorption. In particular, for λ > 600 nm where intrinsic material absorption is weakest, D_hs for both illumination sides tend toward $d_{active}/2$. In the case of P3HT:$PC_{60}BM$ devices with d_{active} = 310 nm, for λ = 473 nm glass side illumination, D_e = 237 nm and D_h = 73 nm, which results in a transport distance for electrons as more than three times as for holes. Simply by illuminating from the Al side, the values of D_e and D_h are flipped thereby forcing holes to travel longer and electrons shorter distances prior to extraction. As the active layer thickness is decreased, the absorption profile or generation profile becomes uniform and hence $D_{e,h} \rightarrow d_{active}/2$ (see Fig. 2.10 for P3HT:$PC_{60}BM$ with d_{active} = 120 nm), which

causes the transport to become insensitive to the illumination side. While this technique is similar to one previously reported,[16] it does not require the use of both standard and inverted devices to achieve long D_e and D_h, respectively, which could cause changes in device function due to the use of different electrode materials. The ability to control the distance electrons and holes travel during transit simply by changing the incident wavelength and illumination side offers a straightforward method to probe the dependence of bimolecular recombination on carrier transport lengths in BHJ organic solar cells.

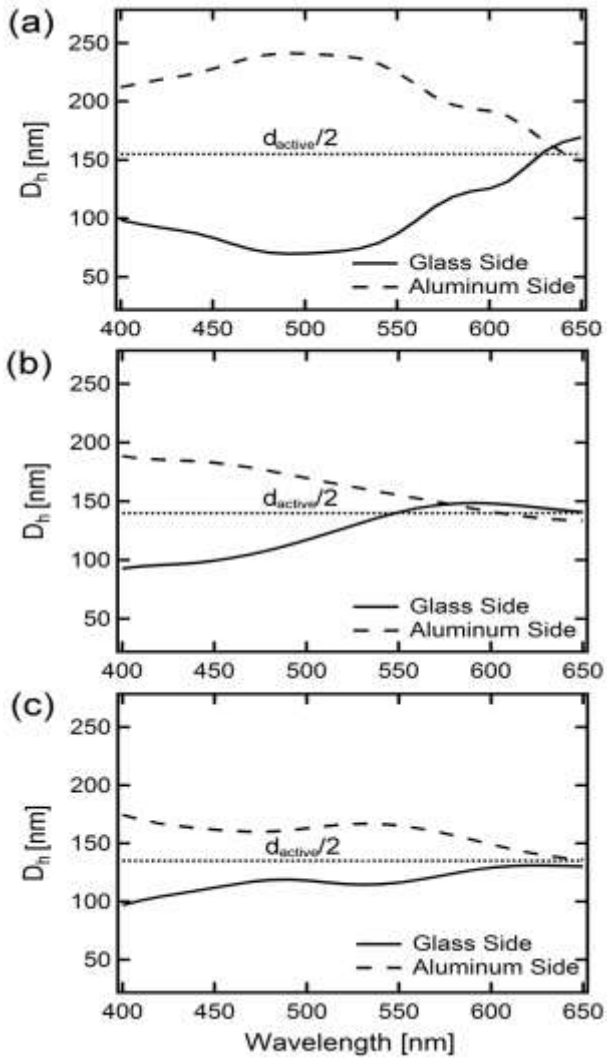

Figure 2.9 Average distance holes are created from the anode, D_h, as dictated by the local absorption profile for (a) P3HT:$PC_{60}BM$, (b) MDMO-PPV:$PC_{60}BM$, and (c) PCDTBT:$PC_{60}BM$ solar cells with d_{active} = 310 nm, 280 nm, and 270 nm, respectively. Dashed lines indicate D_h for constant G, where $D_h = d_{active}/2$. Reprinted with permission from Ref. 56 Copy Right 2012, WILEY-VCH Verlag GmbH & Co. KGaA, Weinheim.

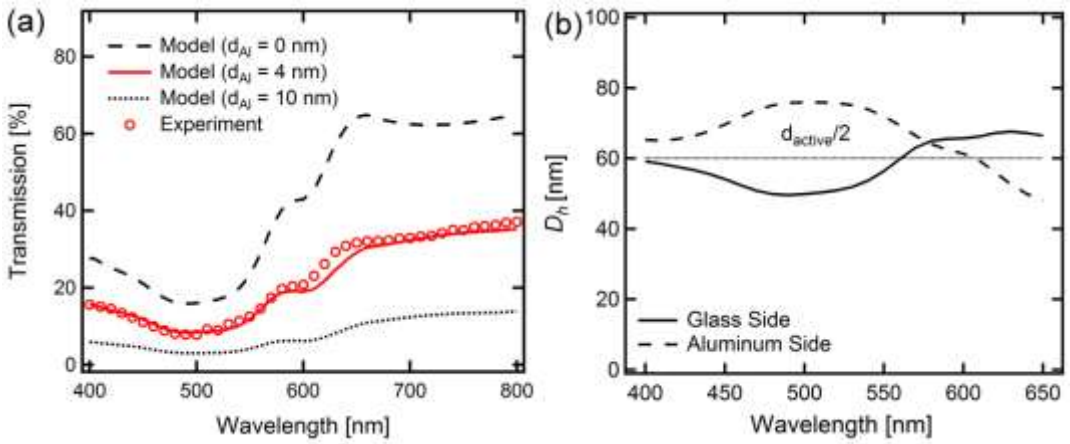

Figure 2.10 (a) Device transmission and (b) D_h for P3HT:PCBM device with d_{active} = 120 nm. As with the thicker d_{active} = 310 nm device the transmission is very sensitive to d_{Al}. In terms of D_h, there is a less significant difference between glass and Al side illumination compared to the thicker device. Due to the minimal bimolecular recombination measured for this device for both illumination sides, it is concluded that the D_h and D_e values are less than those required to instigate bimolecular recombination for this sample. Reprinted with permission from Ref. 56. Copy Right 2012, WILEY-VCH Verlag GmbH & Co. KGaA, Weinheim.

2.3.4 Dependence of Photocurrent on Absorption Profile

In Fig. 2.9, it is apparent that illuminating the device from different sides of the photoactive layer have the significant effect on changing $D_{e,h}$ values. In order to demonstrate any effect of $D_{e,h}$ on bimolecular recombination, one of the most important process during charge transport, we measure the photocurrent ($J_{photo} = J_{light} - J_{dark}$) under variable light intensity using a blue (λ = 473 nm) laser. The light intensity experiment results of all three device types are shown in Fig. 2.11. Differences between the curve shapes of J_{photo} vs. V_{app} under different sides of illumination are observed for all three device types in terms of fill factor (FF) and applied voltage (V_{app}) where J_{photo} reaches a saturation level. The largest differences in J_{photo} are found in the P3HT:PC_{60}BM device while the least variation is observed for the PCDTBT:PC_{60}BM solar cells. For the

P3HT:$PC_{60}BM$ device illuminated from the Al side, J_{photo} saturate at a greater reverse bias, which means a higher internal electric field is required to force out all the generated carrier. However, P3HT:$PC_{60}BM$ device's *FF* is markedly improved and J_{photo} approaches a saturation level at a lower reverse bias corresponding to a weaker electric field upon illumination from the glass side. The experimental results will be discussed in terms of local absorption profiles upon glass and Al side illumination, which correspond to D_h values of 73 nm and 238 nm, respectively. For MDMO-PPV:$PC_{60}BM$ device performance is better for Al side illumination where D_h = 106 nm compared to glass side illumination (D_h = 178 nm), while PCDTBT:$PC_{60}BM$ device performance shows similar performance regardless of illumination side. The observed differences in J_{photo} indicate that recombination of photo generated current is dependent on the local absorption profile as quantified by De,h. Importantly, measurements for each sample type are performed on the same device, so comparisons between separate devices are not required that may exhibit differences in active layer morphology or layer interfaces.

It should be noted that in order to appropriately compare J_{photo} for different illumination sides, controlled light intensities are used that produce approximately equivalent carrier densities. This is checked by comparing the saturated photocurrent levels under high reverse bias. Light intensities are controlled using an appropriate choice of optical filter that equalizes the photon flux to the active layer due to increased reflection when illuminating from the Al side. This optical loss equates to a factor of ~2, as indicated by the ratio of light intensities in Fig. 2.11. Equalization of photon flux is important, because photocurrent losses such as bimolecular recombination depend on the density of free carriers, which is proportional to the saturation level of J_{photo}. Therefore,

illumination from opposite sides produces approximately the same number of free carriers. By comparing the saturated J_{photo} under laser illumination and under 1 Sun illumination, we deduce that the carrier densities are ~3/4 their 1 Sun values at highest light intensity.

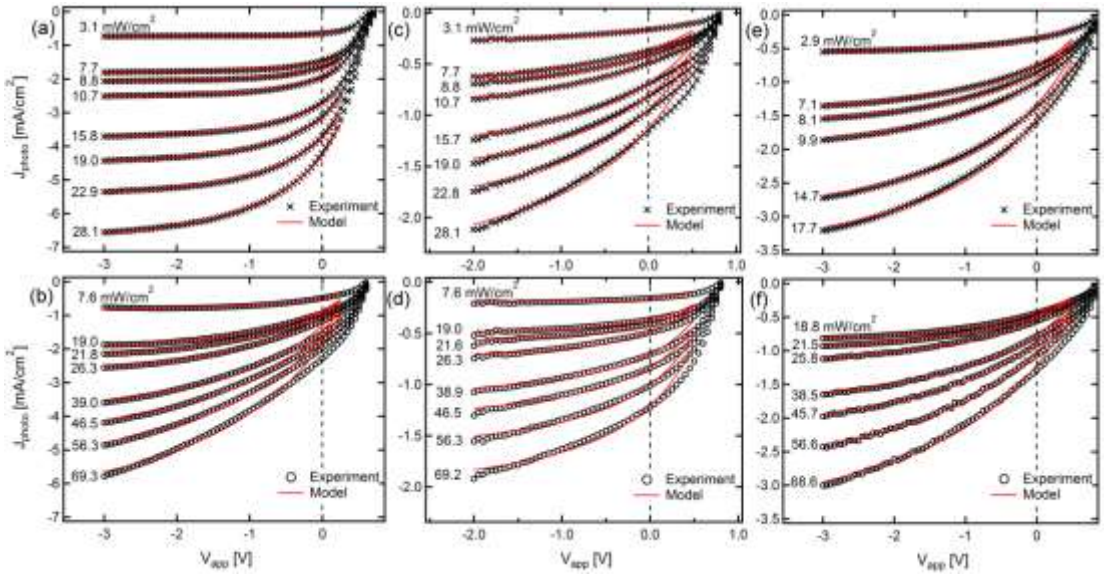

Figure 2.11 Photocurrent (J_{photo} = J_{light} − J_{dark}) under various light intensities when illuminating with λ = 473 nm from (a,c,e) glass side and (b,d,f) Al side for devices with (a,b) P3HT:$PC_{60}BM$, (c,d) MDMO-PPV:$PC_{60}BM$, and (e,f) PCDTBT:$PC_{60}BM$ as the photoactive layer. Model lines are fits to the Hecht equation where the mobility lifetime product is determined as shown in Figure 2.13. Reprinted with permission from Ref. 56. Copy Right 2012, WILEY-VCH Verlag GmbH & Co. KGaA, Weinheim.

While we have shown that the local absorption profile has a significant impact on J_{photo}, it is not clear which loss mechanisms are affected, since multiple recombination processes may be dependent on V_{app}. Monomolecular recombination in the form of free carrier charge trapping[79–81] or inefficient charge transfer state dissociation at the donor/acceptor interface[82,83] are possible candidates along with bimolecular recombination of free carriers, where each has been argued to depend on the internal

electric field. Loss of excitons during diffusion to the donor/acceptor interface is excluded as the excitons should be charge neutral and not influenced by the internal field. The multitude of loss processes at work makes it difficult to determine which recombination mechanisms are affected by the local absorption profile and prompt differences in J_{photo}. However, the scaling exponent, α, of the photocurrent with light intensity is a measure of bimolecular recombination and can help disentangle this loss process from the mix of possible mechanisms. This is especially important for MDMO-PPV:$PC_{60}BM$ devices, where J_{photo} is known to reach saturation photocurrent levels as $V_{app} \rightarrow$ -10 V, presumably due to monomolecular recombination in the form of charge transfer state dissociation.[83] The scaling exponent is determined from the following expression:

$$J_{photo} = \beta P_{light}^{\alpha} \tag{2.11}$$

Where P_{light} is the light intensity and β is a constant. Scaling exponents as functions of V_{app} are shown in Figure 2.12 for all three device types (corresponding to data and light intensities from Figure 2.11) including a P3HT:$PC_{60}BM$ solar cell with d_{active} = 120 nm. For all traces, the scaling exponent decreases as V_{app} increases, due to a decrease in internal electric field and corresponding reduction in carrier sweep out and increase in carrier density. In this work, we interpret higher scaling exponents that are closer to unity to indicate lower bimolecular recombination. It should be noted that α = 1 as observed under high reverse bias does not negate this loss process completely as recently shown.[84,85] However, we do assert that α is a measure of bimolecular recombination and that its deviation from unity is an indicator of the strength of this process. As a final note, serial resistance can change the shape of the photocurrent for higher V_{app} approaching

V_{oc}[86] and hence skew the scaling exponent in this voltage range.[87] Series resistance is more prevalent for these semi-transparent devices due to the thin Al cathode, but the primary conclusions drawn from the data occur for lower voltages outside of this regime.

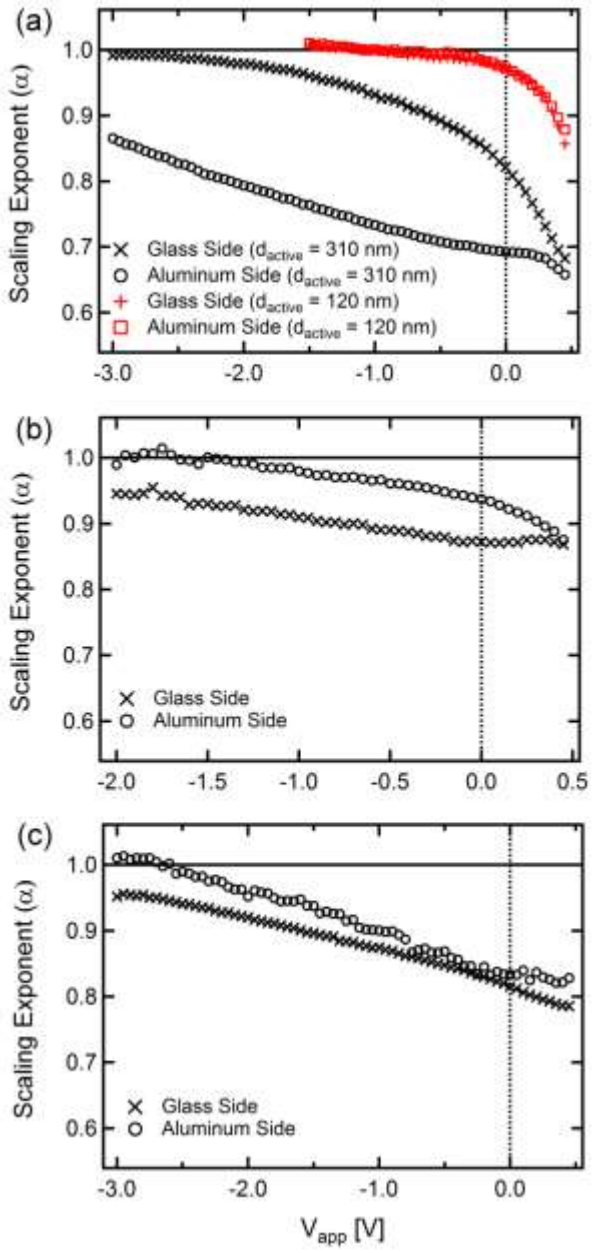

Figure 2.12 Scaling exponent of photocurrent with light intensity for (a) d_{active} = 120 nm and 310 nm P3HT:$PC_{60}BM$, (b) d_{active} = 280 nm MDMO-PPV:$PC_{60}BM$, and (c) d_{active} = 270 nm PCDTBT:$PC_{60}BM$ devices. Reprinted with permission from Ref. 56. Copy Right 2012, WILEY-VCH Verlag GmbH & Co. KGaA, Weinheim.

In terms of the different devices, for the P3HT:$PC_{60}BM$ solar cells with d_{active} = 120 nm, α is identical for both illumination directions and close to unity at short-circuit and in reverse bias. This is similar to previous results for optimized P3HT:$PC_{60}BM$ solar cells.[85] However, as d_{active} is increased to 310 nm, α remains higher under glass side compared to Al side illumination. Since under glass side illumination, D_e = 237 nm and D_h = 73 nm, while under Al side illumination these values are flipped, we propose that the differences in recombination are due to changes in the average distances holes and electrons must travel in order to be extracted. Since there is greater recombination when D_h is large, we argue that holes are the restricted carriers that determine the onset of bimolecular recombination. The opposite is true for MDMO-PPV:$PC_{60}BM$ where larger α values are noted for Al side illumination (D_e = 102 nm; D_h = 178 nm) compared to glass side illumination (D_e = 174 nm; D_h = 106 nm).This would signify that electrons are the more restricted carrier that determines the onset of recombination. Finally, PCDTBT:$PC_{60}BM$ does not show clear differences in α with illumination side for glass side (D_e = 153 nm; D_h = 117 nm) and Al side (D_e = 110 nm; D_h = 160 nm) illumination. However, the contrast between $D_{e,h}$ for the different illumination sides is not as significant for this BHJ blend compared to P3HT:$PC_{60}BM$ and MDMO-PPV:$PC_{60}BM$ (see Fig. 2.9).

In order to estimate the transport lengths of the restricted carrier for each device type (as deduced from Fig. 2.12), we fit the mobility-lifetime product in the Hecht expression to J_{photo} from Figure 2.11. Even though transient methods exist to measure this product more accurately,[88] we only wish to show how the local absorption profile impacts estimation of this product within the framework of the Hecht expression. Recently, this model has been used to describe the photocurrent of BHJ solar cells[80] but for the case of

negligible bimolecular recombination. However, this simple model is still applicable here as it describes carrier transport in an electric field where it is applied herein primarily in the reverse bias regime. This is the transition region for these devices where the scaling factor of Fig. 2.12 drop below unity and bimolecular recombination becomes a significant loss of photocurrent. The model is as follows:

$$J_{photo} = \frac{J_{sat}\,\mu\tau\,(V_0 - V_{app})}{d_{active}\,D_{e,h}}\{1\text{-}\exp[\frac{-d_{active}\,D_{e,h}}{\mu\tau\,(V_0 - V_{app})}]\} \qquad (2.12)$$

where J_{sat} is the saturated photocurrent, V_0 is the applied voltage where $J_{photo} = 0$, and $\mu\tau$ is the mobility-lifetime product of the restrictive carrier species. Either D_e or D_h is chosen depending on whether electrons or holes are determined to have the shorter intrinsic transport length as described above. This model is slightly different compared to the one employed by Street et al.[81] in that we incorporate the optical generation profile through $D_{e,h}$ whereas a constant local absorption profile has been previously used. For the model fits, J_{sat} is also a fit parameter as it only controls the saturation level of J_{photo} and does not influence the shape of the curves. Values for V_0 are taken from the experimental data.

Fig. 2.13 displays $\mu\tau$ as functions of the average generation rate in the photoactive layer, $\langle G \rangle$, for each device type corresponding to the fits from Fig. 2.11. Values of $\langle G \rangle$ are calculated from the fitting parameter, J_{sat}, using the expression, $J_{sat} = q\langle G \rangle\, d_{active}$, where q is the elementary charge. Here, $\langle G \rangle$ is proportional to the density of free carriers depending on the efficiency of exciton diffusion and charge separation that will vary for different blends. Illuminating from different sides of the same device ensures that these processes leading to the creation of free carriers will be equivalent when comparing the photocurrent for glass and aluminum side illumination. By using filters to

ensure that J_{sat} is the same for different illumination sides (see Fig. 2.11) the prevalence of bimolecular recombination can be appropriately compared for different illumination directions. For all cases, $\mu\tau$ drops as $<G>$ increases as predicted for devices with significant bimolecular recombination.[81] This follows intuition, because as the density of free carriers increases as light intensity increases, so does the probability of recombination. In spite of the simplicity of this model, it does exhibit predictive power. First, regardless of illumination side, $\mu\tau$ is roughly the same even with the differences in J_{photo}. This occurs, because $D_{e,h}$ used in Eq. (2.9 and 2.10) is different for opposite illumination sides and results in overlap of $\mu\tau$ vs $<G>$. In the example of P3HT:PC_{60}BM, D_h = 73 and 238 nm for glass and Al side illumination, respectively. On the other hand, if it is assumed that $D_h = d_{active}/2$, as would be the case for a uniform generation profile, then $\mu\tau$ no longer overlap. This occurs for each device type even though $D_{e,h}$ and $d_{active}/2$ are more similar for MDMO-PPV:PC_{60}BM and PCDTBT:PC_{60}BM solar cells. The agreement of $\mu\tau$ for different illumination sides supports that $\mu\tau$ is an intrinsic property of each BHJ and demonstrates the influence of the optical generation profiles on the results of this model.

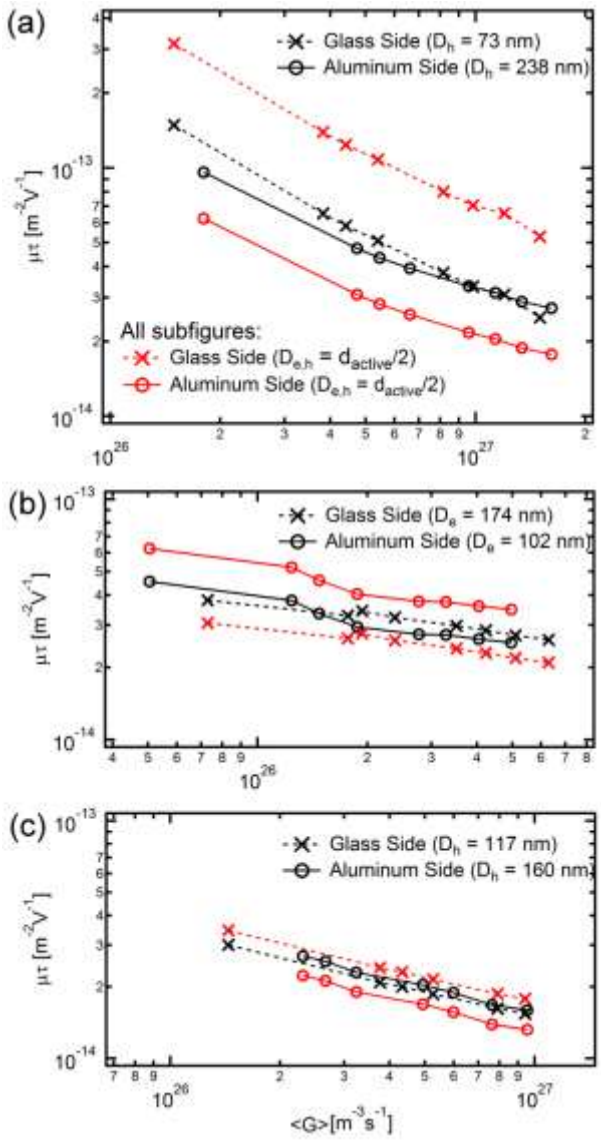

Figure 2.13 Mobility-lifetime product of restricted carrier species, $\mu\tau$, as a function of average exciton generation rate as determined from fits to the Hecht equation to photocurrent data from Fig. 2.11. When using D_e or D_h in Equation 4 depending on whether the restricted carriers are electrons or holes, respectively (as deduced from Fig. 2.12), similar values of $\mu\tau$ are obtained for glass and Al side illumination (black data points). On the other hand, setting $D_{e,h} = d_{active}$ /2 in Eq. 4, as is the case for a uniform local absorption profile, causes disagreement in $\mu\tau$ (red data points). Lines are guides to the eye. Reprinted with permission from Ref. 56. Copy Right 2012, WILEY-VCH Verlag GmbH & Co. KGaA, Weinheim.

In spite of the success of this model in estimating $\mu\tau$ for each device type there are drawbacks due to its simplicity and the known complex properties of BHJ solar cells. First, the model does an increasingly poor job fitting the data close to open-circuit. For this reason, the models are only fit from reverse bias up to ~0.2 V less than V0. This is believed to be due to significant space charge that is not included in the model where the internal electric field is assumed to be uniform. For example, the model works well for P3HT:PC_{60}BM with glass side illumination where there is minimal recombination and presumably low space charge build-up. On the other hand, the model breaks down when fit to Al side illumination where there is significantly higher recombination. This speculation is checked by performing drift/diffusion simulations that include space-charge effects[21] using both strongly decaying and constant generation profiles (not shown here). Even when electron/hole mobilities are assumed to be equal, a strongly decaying profile causes poor device performance due to significant bimolecular recombination that is reminiscent of space charge limited photocurrent[89] as was observed in previous work.[16]

2.3.5 Wavelength Dependence of Bimolecular Recombination

Thus far, we have controlled G by changing the illumination side using a single excitation wavelength, λ = 473 nm. From Fig. 2.9, it is evident that the illumination direction provides a greater change in $D_{e,h}$ compared to the excitation wavelength. However, there should still be a measurable change in recombination depending on the illumination wavelength, because the wavelength also changes G and modifies $D_{e,h}$. Fig. 2.14 shows the bimolecular recombination efficiency, η_{BR}, determined using a recently demonstrated lock-in light bias technique[85,90] for the P3HT:PC_{60}BM device with d_{active} = 310 nm. Values of D_h show the largest change for this device (see Fig. 2.9a). Compared

to the photocurrent method used above, the modulated signal of a monochromatic light source, λ_{mod}, is measured under short-circuit in response to varying levels of light intensity illumination. White light bias is incident on the glass side, while the modulated monochromatic light is illuminated from either the glass or Al side of the device.

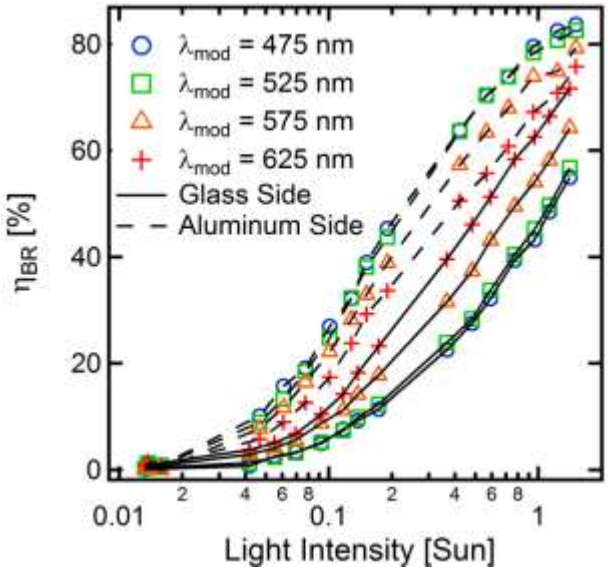

Figure 2.14 Bimolecular recombination efficiency (η_{BR}) under solar simulated light bias (glass side) when simultaneously illuminating a monochromatic modulated light (λ_{mod}) from either the glass or Al side of the device. Data corresponds to P3HT:PC_{60}BM device with d_{active} = 310 nm. The largest recombination is noted for shorter λ_{mod} with Al side illumination (i.e. long D_h) while the least recombination occurs for glass illumination with shorter λ_{mod} (i.e. short D_h). Lines are included to guide the eye. Reprinted with permission from Ref. 56. Copy Right 2012, WILEY-VCH Verlag GmbH & Co. KGaA, Weinheim.

From this experiment, it is evident that the largest amount of bimolecular recombination occurs for shorter wavelengths when λ_{mod} is shone from the Al side. As λ_{mod} is increased causing a reduction in D_h, η_{BR} drops accordingly. When the illumination direction is flipped to glass side, the longer wavelengths have the highest recombination where the shorter wavelengths have the least. This follows the results from the J_{photo}

measurements where high values of D_h show greater recombination than shorter ones. Final evidence for this comes in the form of J_{photo} measurements using a λ = 633 nm laser where it is evident that recombination is not affected by the illumination side since D_h is nearly equivalent (see Fig. 2.15).

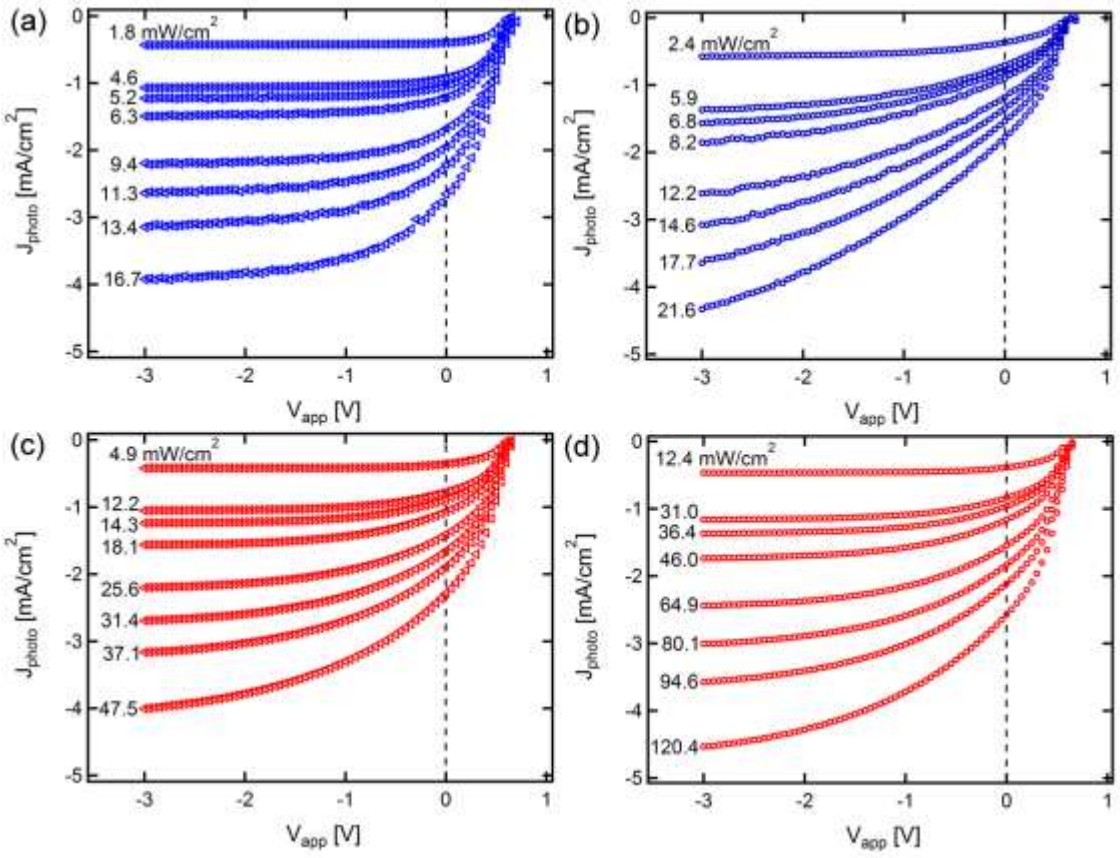

Figure 2.15 Photocurrent under various light intensities for P3HT:PCBM device with d_{active} = 310 nm when illuminating under the following wavelengths and illumination directions: (a) λ = 473 nm, glass side; (b) λ = 473 nm, aluminum side; (c) λ = 633 nm, glass side; (d) λ = 633 nm, aluminum side. There are significant differences in the photocurrent when illuminating with λ = 473 nm due to drastic differences in $D_{e,h}$ depending on illumination side. For λ = 633 nm, the photocurrent is almost identical due to $D_{e,h} \approx d_{active}/2$ = 155 nm. Reprinted with permission from Ref. 56. Copy Right 2012, WILEY-VCH Verlag GmbH & Co. KGaA, Weinheim.

2.3.6. Discussion and Implications for Device Performance

The dependency of bimolecular recombination on both the illumination side and incident wavelength strongly link this loss process to the distance carriers must travel in order to be extracted. Thus far, we have focused on single-wavelength measurements to achieve greater control of the absorption profile. However, under 1 Sun illumination, the absorption profile will be a convolution of all wavelengths weighted by both the wavelength-dependent absorption in the active layer and the wavelength-specific solar irradiance. Fig. 2.16 shows calculations of D_h for the full spectrum 1 Sun local absorption profile for each BHJ blend studied herein using d_{Al} = 100 nm. Ratios are taken of $d_{active}/2$ to D_h where the deviation from unity as d_{active} increases demonstrates the transition from uniform to non-uniform local absorption profiles. For all devices with d_{active} ~ 100 nm, the assumption of a uniform profile is a reasonable approximation. Below 100 nm, deviation from unity is noted, but this corresponds to very short $D_{e,h}$ values, so the absolute difference between D_h and $d_{active}/2$ is < 10 nm. Furthermore, the device with P3HT:$PC_{60}BM$ undergoes greater deviation from a uniform profile due to the higher absorption coefficient for this blend compared to MDMO-PPV:$PC_{60}BM$ and PCDTBT:$PC_{60}BM$. In all cases, light absorption becomes more concentrated toward the PEDOT:PSS/BHJ interface as d_{active} increases. This occurs even though $D_h \sim d_{active}/2$ for longer wavelengths (see Fig. 2.9).

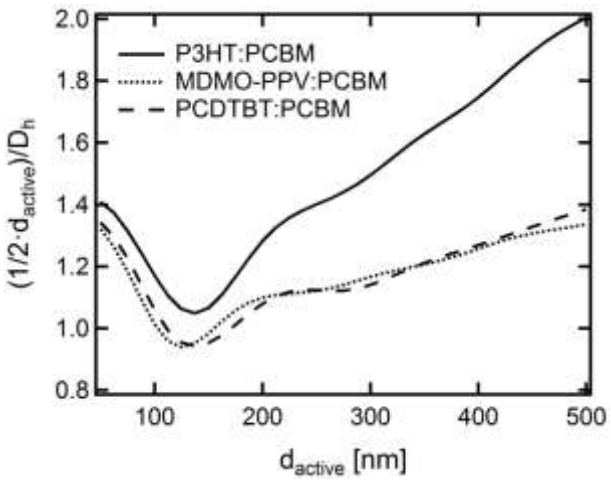

Figure 2.16 Calculated ratio of $d_{active}/2$ to D_h for 1 Sun illumination as a function of d_{active} for the three BHJ blends studied herein. Greater deviation from unity as d_{active} increases indicates a local absorption profile becoming less uniform and more weighted toward the PEDOT:PSS / BHJ interface in the photoactive layer. Reprinted with permission from Ref. 56. Copy Right 2012, WILEY-VCH Verlag GmbH & Co. KGaA, Weinheim.

Pairing this result with the determination of the restricted carrier species has important implications for devices performance. For P3HT:PC_{60}BM, long D_h values, opposed to long De values, trigger bimolecular recombination. This indicates that hole transport is more critical in determining the extent of bimolecular recombination, possibly due to the previously noted lower hole mobility compared to electron mobility for this system.[17] On the other hand, MDMO-PPV:PC_{60}BM shows greater recombination when D_e, not D_h is longer, which is contrary to previous mobility measurements for this blend,[91] but agrees when these mobilities are integrated into morphological-dependent modeling of carrier extraction for this blend.[92] The final system, PCDTBT:PC_{60}BM, shows not as strong a preference between electrons or holes being the restricted carrier species. It may then be postulated that electron and hole transport is more balanced for this system, which has also been proposed for this polymer when blended with

$PC_{71}BM$.[65] Combining these results with those from Fig. 2.16, potentially explains high performance that has also been achieved for standard P3HT:$PC_{60}BM$ devices with $d_{active} >$ 200 nm.[14,66] The fact that hole transport dictates the onset of bimolecular recombination indicates that a local absorption profile more weighted toward the anode will assist holes in reaching their exit contacts. This agrees with our previous findings for P3HT:$PC_{60}BM$ where greater recombination was noted for inverted devices where the local absorption profile is weighted more heavily toward the cathode thereby forcing holes to travel long distances in order to be extracted.

Along with these specific systems, these results contribute to the ongoing debate involving the nature of photocurrent generation in BHJ solar cells. Determining the root cause of the reduction of photocurrent that occurs between reverse bias and open-circuit conditions is central to this discussion. Given the linearity of observed photocurrent with light intensity for many high performing systems, it is argued that bimolecular recombination is not a significant loss mechanism at short-circuit[85] or even up to maximum power point.[81,90,93,94] The voltage-dependence of the photocurrent is then ascribed to a monomolecular mechanism either in the form of charge transfer state dissociation at the donor/acceptor interface[82,83] or non-geminate free carrier charge trapping.[79–81] However, it has been recently shown that a linear photocurrent scaling does not guarantee the absence of bimolecular recombination[84] where photocurrent models based solely on bimolecular recombination adequately reproduce device performance.[92,95,96] Furthermore, the generation of free carriers has been shown to be independent of the applied electric field,[18] which would preclude a charge transfer state dissociation mechanism causing the photocurrent voltage-dependence. On the other hand,

non-geminate recombination has been shown to depend on applied bias[97] as we observe here with the voltage-dependence of the scaling exponent. Likewise, even though higher levels of bimolecular recombination are noted in the devices studied herein compared to those in other studies due to their non-optimal thickness, it is demonstrated that this loss process depends on the distance carriers must travel in order to be extracted. Therefore, bimolecular recombination is clearly related to the loss of free carriers, where it is important to consider the intrinsic carrier transport lengths for different BHJ materials in conjunction with the local absorption profile when designing high-performance devices. This is especially important for novel polymers where large d_{active} is used to boost light absorption and the potential for photogenerated current. For instance, good device performance was recently achieved using d_{active} ~1000 nm.[98] Determining the extent of carrier recombination with respect to each carrier species will become increasingly important for these high-absorbing devices. The method presented here using semi-transparent solar cells offers a simple means to discriminate between electron and hole contributions to bimolecular recombination by utilizing the local absorption profile in the photoactive layer.

2.4 Absorption Profile in Transient Photocurrent Measurement

2.4.1 Transient Photocurrent Experiment in OPVs

Transient photoconductivity is a common technique typically used to study the kinetics of sweep-out and recombination in low mobility materials. The technique was applied to perform on organic solar cells, but interpretation of its results is not easy. Optical absorption and generation of electron-hole pairs occur throughout the active layer. Both electron and holes are swept out by internal electric field and collected at the

electrodes, making it difficult to distinguish the transient responses of electrons and holes. Cowan et al. described the transient process in OPVs by a simply two-carrier (fast and slow) transport model. However, that model is not able to identify whether the electron or hole is the fast carrier. Herein, with the knowledge of absorption profile, we manipulated the two carriers transport distances in transient photocurrent experiment by changing the illumination direction as discussed in previous sections. This provided more information about charge carrier transport than one side illumination in the transient photocurrent experiment.

Photoinduced charge separation via electron and hole transfer happens very fast, within a time scale of subpicoseconds.[79] Then, some of those initially generated carriers (i.e. electrons and holes) form bound interfacial charge transfer excitons[81,99] or fall into interfacial traps, which can lead to recombination.[28,100–103]At longer times, mobile charge carriers are either swept out and collected at the electrodes by the internal electric field or recombined during the sweep-out process. The photocurrent of the solar cell is thus a competition between sweep-out and recombination.

The internal electric field is determined by active layer thickness and the internal voltage (V_{int}) that is the difference between the built-in voltage (V_{BI}) across the active layer and the applied voltage (V_{app}), $V_{int} = V_{BI} - V_{app}$. V_{oc} (at total current density $J_{light} = 0$) is slightly less than V_{BI}, where photocurrent density $J_{photo} = 0$.[79] Thus, at short circuit, the internal voltage can be approximated as the open circuit voltage, $|V_{int}| \approx |V_{BI}| \approx |V_{oc}|$. As the V_{app} approaches V_{oc}, the $|V_{int}| \rightarrow 0$. The decay of the transient photocurrent is dominated by the sweep-out of free carriers when $V_{app} \leq 0$ (V_{int} is high) and by

recombination when V_{app} approaches V_{oc} (V_{int} is low). In the simplest analysis, carriers diffusion is assumed to be negligible relative to drift current.[79]

To monitor two carrier sweep-out and recombination, transient photocurrent measurements were performed on solar cells fabricated from P3HT:$PC_{60}BM$. A Continuum Minilite laser excitation source that emits a pulse of ~ *5* ns duration with a frequency f =10 Hz at λ = 532 nm was used. The wavelength is within the absorption band of the P3HT:$PC_{60}BM$ material. Laser pulses without focusing are directed into the organic devices (area ~0.1 cm^2). A current transient was observed after each pulse. Such current was monitored with a fast oscilloscope as the voltage drop across a 50 ohm resistor (see Fig. 2.17). This value of the resistor was chosen as a compensation to have measurable signal while limiting the *RC* (~0.2 μs, product of circuit resistance and capacitance) response time of the circuit to a level that does not largely affect the results. The current transients were measured at different values of the applied voltage and recorded after averaging 8 measurements. The total collected charges $q_{col} = \int_0^\infty J(t)dt$ should be lower than 20% of value of *CV* (~10^{-9} C).[79] Therefore, the pulsed light intensity was adjusted to be ~0.08 μJ/cm^2 for glass side illumination, while it was adjusted to produce a similar level of current when illuminated from through the metal.

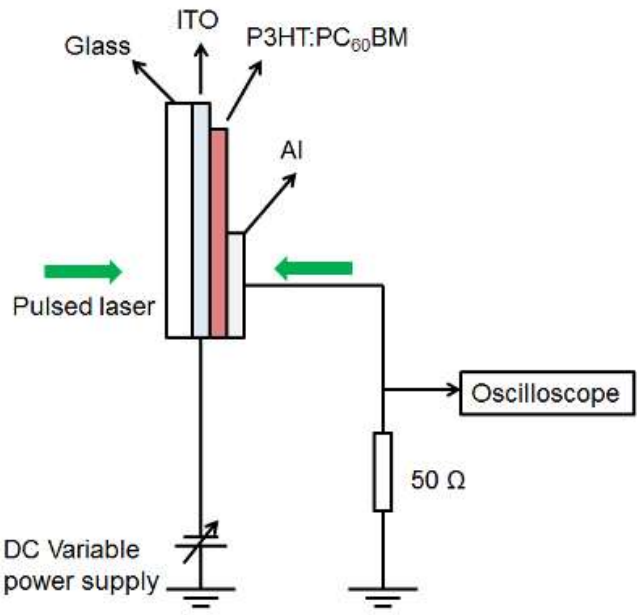

Figure 2.17 Diagram of transient photocurrent experimental set up. The device can illuminated from either side by a pulsed laser.

The solar cells were made intentionally thicker (~250) nm than optimal processing conditions would dictate in order to reduce the internal capacitance of the cell and enhance the difference between absorptions under illumination from two sides of the cell. Because the calcium is not used, relatively low device efficiency ~1.2% are achieved, with V_{oc} ~ 0.5V, J_{sc} 6~7 mA/cm^2 and FF ~0.4. Fig 2.18 shows measured transient photoconductance (I/V_{int}) under illumination from glass side with different applied voltage. The initial conductance (prior to sweep-out or recombination) is nearly independent of applied voltage, which implies that built in voltage (V_{BI}) is well defined at beginning.[65,93] As shown in Fig 2.15, the photocurrent response becomes faster as V_{app} increases which agrees with previous reported results.[79] One can also notice an initial fast decay in the current is followed by a slower response, and there is no well-defined carrier sweep-out time when the current drops to zero.

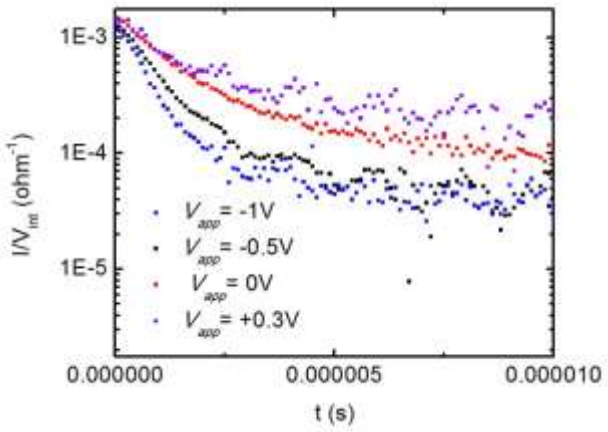

Figure 2.18 Transient photoconductance (I/V_{int}) vs time measured under different V_{app}. V_{BI} is estimated from V_{oc} to be 0.5V.

2.4.2 Identification of Free Carrier Transport Process in Transient Measurement

As it is clear to see there are two decay processes of the current in a semi-log plot (Fig. 2.18), Cowan et al. suggested a two-carrier transients model,[79] where the transient photocurrent can be characterized as contributions from fast and slow carrier drift currents. In that model, a uniform generation profile was assumed even though the active layer is relatively thick (~200nm).[79] Besides, only glass side illumination was considered and hence one could not distinguish hole and electron transport from the so called fast and slow responses. However, the model can be modified by including generation profile *G*, and is changed as

$$J(t)_{glass} = \int_{\mu_n Et}^{d} G_{glass}(x - \mu_n Et)\frac{e\mu_n \mathrm{E}}{d}dx + \int_{0}^{d-\mu_p Et} G_{glass}(x+\mu_p Et)\frac{e\mu_p \mathrm{E}}{d}dx \qquad (2.13)$$

$$J(t)_{metal} = \int_{\mu_n Et}^{d} G_{metal}(x - \mu_n Et)\frac{e\mu_n \mathrm{E}}{d}dx + \int_{0}^{d-\mu_p Et} G_{metal}(x+\mu_p Et)\frac{e\mu_p \mathrm{E}}{d}dx \qquad (2.14)$$

where glass and metal represent where the light comes in and μ_n and μ_p are electron and hole mobilities. These equations describe the case of conventional devices as holes are collected at the glass side while the electrons are collected at the metal side. Fig. 2.19a shows the simulated transient photocurrents under illumination from both sides of a conventional device with electron mobility greater than the hole's. Since in most cases one carrier is much faster than the other, the initial drop of the current is dominated by one carrier sweep-out.[79] Assuming the electron is faster than the hole, the photocurrent drops faster when light come in through the metal side due to generation of electron is closer to the metal electrode. However, in the case of inverted devices, the result is the opposite as the electron needs to exit from the glass side (see Fig 2.19b). The experimental results of both conventional and inverted devices of P3HT:PC_{60}BM are shown in Fig 2.20, which identifies the electron as the faster carrier in P3HT:PC_{60}BM devices.

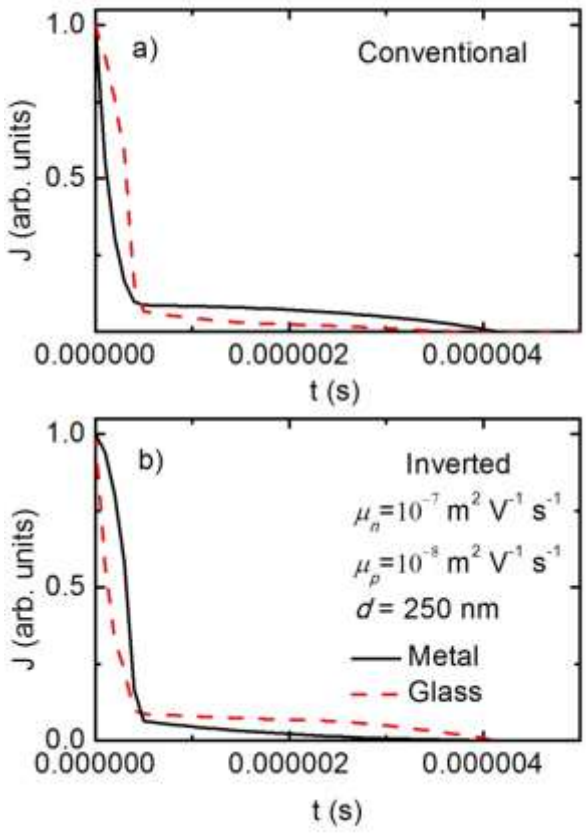

Figure 2.19 Simulated transient response with illumination from both either side of the device. a) conventional device and b) inverted device. The generation profile is calculated in a device with the configuration of ITO/PEDOT:PSS/P3HT:PC_{60}BM/Al (conventional) and ITO/ZnO:Al/P3HT:PC_{60}BM/WO3/Al (inverted).

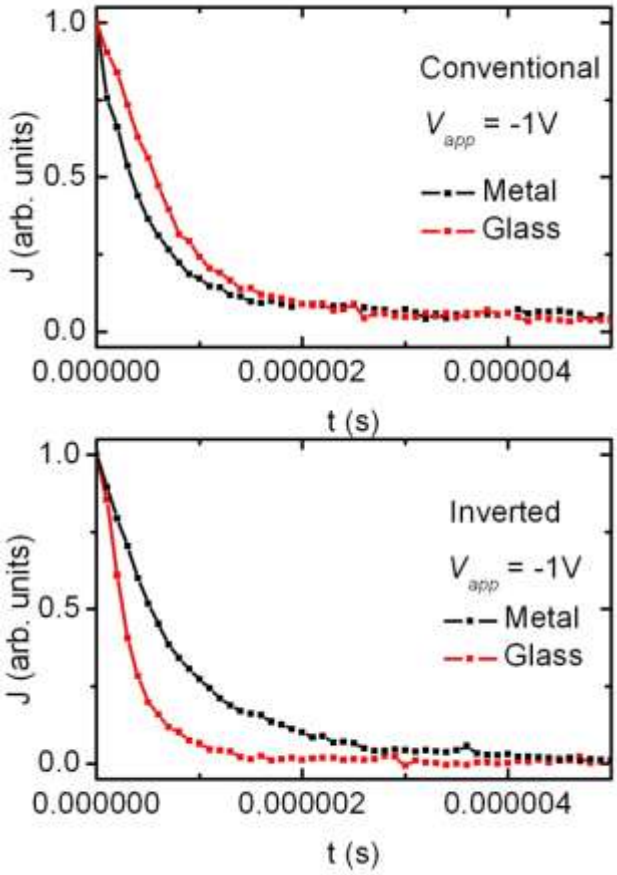

Figure 2.20 Measured transient response with illumination from both either side of the device. a) conventional (ITO/PEDOT:PSS/P3HT:PC_{60}BM/Al) device and b) inverted device (ITO/ZnO:Al/P3HT:PC_{60}BM/WO3/Al).

2.4.3 Estimation of Mobility

Following Cowan et al. work, the mobility of the faster carrier (i.e. electron) can be estimated from the responses time ($t_{1/e}$) and sweep-out time (t_{sw}), which is defined as the point of 1/e signal decay. A $t_{1/e}$ vs. $1/V_{int}$ plot of electron sweep-out process can be obtained for either side of the illumination in Figure 2.21. Cowan et at. applied equation $t_{1/e} \approx t_{sw} = d^2/2\mu V_{int}$ to estimate the motility.[79] Due to the non-uniform generation profile, half of the active layer thickness ($d/2$) used in Cowan's equation should be replaced by

the average generation distance ($D_{e,h}$) defined by Eq. (2.9) and (2.10). When illuminating the device from the glass side, D_e=168 nm and D_h = 82 nm in the conventional device. When illuminating the device from the metal side, D_e=77 nm and D_h = 173 nm in the conventional device. Therefore, the μ_n is estimated to be ~8×10^{-8} m^2 $V^{-1}s^{-1}$ from data obtained from both side illuminations. Similar estimation can be applied to the hole mobility. However, as shown from Fig. 2.19 when the hole is an order of magnitude slower than the electron, the initial process is dominated by the electron. It will not easy to separate hole sweep-out from electron sweep-out until the total current decay to 1/10 of the initial value, around where sweep-out process should become faster under glass side illumination (as shown in Fig 2.19a), due to holes are averagely generated closer to the electrode under glass side illumination. However, because of the low signal, the noise becomes significant and makes it hard to see the slope changing point predicted in the model. Hence, the estimation of $t_{1/e}$ is started from 1/e of the peak signal. And the hole mobility is approximated to be 2×10^{-8} m^2 $V^{-1}s^{-1}$ from metal side illumination data and 1×10^{-8} m^2 $V^{-1}s^{-1}$ from glass side illumination data. The greater mobility value estimated from data taken under metal side illumination is possibly due to the contribution from electron sweep-out to current decay is not negligible in that time. Nevertheless, the results roughly agree with previous reported mobilities. Furthermore, a lifetime $t_R \approx 1.5$ μs is obtained from measuring the 1/e of the current decay at forward bias[79] (see Fig. 2.22), under which the internal field is weak and the signal follows exponential decay as recombination time (t_R) is shorter than t_{sw}.[79]

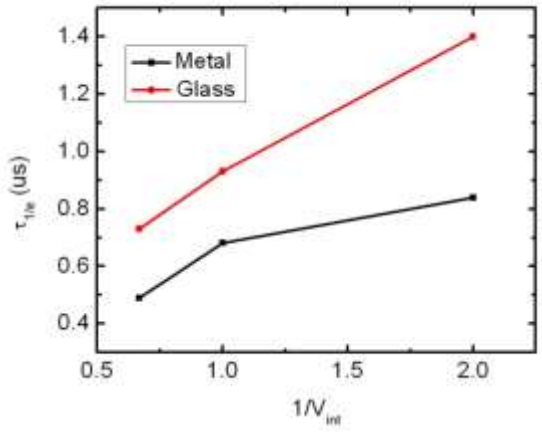

Figure 2.21 Estimated sweep-out time of the faster carrier (i.e. electron) vs. the inverse of the internal voltage in both cases of metal and glass side illumination. In sweep-out limit (high internal voltage), the mobility may be extracted from a linear fit of the data according to the drift equation $t_{sw}= d\ D_e/\mu_e V_{int}$

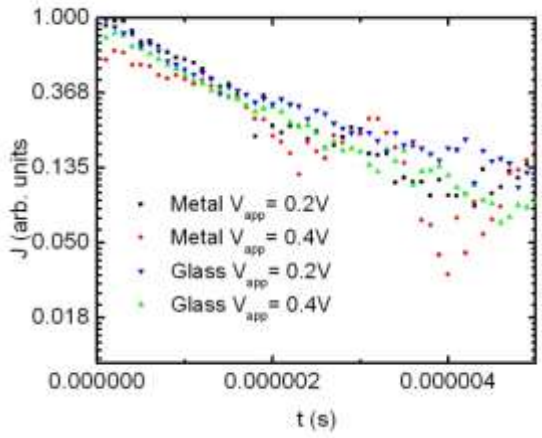

Figure 2.22 Transient current under forward bias (V_{app} >0) in both cases of metal and glass side illumination. The lifetime can be estimate from the time of signal decay to 1/e.

Fig. 2.23 shows simulated transient photocurrent under illumination from either side of the device with 3 sets of mobilities. A better fit by using electron mobility to be ~ 3×10^{-8} m^2 $V^{-1}s^{-1}$ rather than the value estimated above by using average transport distance. This value is also smaller than previous reported electron mobility for P3HT:$PC_{60}BM$.[79] However, as shown in Fig. 2.23, greater mobility predicts sharper photocurrent decay

than experiment measured results. The discrepancy can be resulted from the simplicity of the drift model which did not include internal voltage changes with carrier sweep-out or the sensitivity of the set-up.

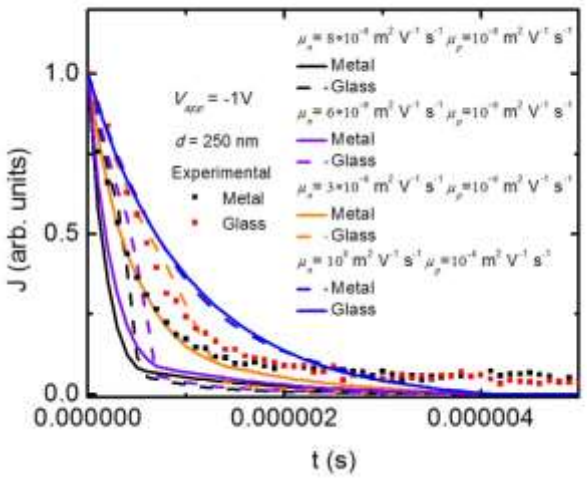

Figure 2.23 Simulated transient photocurrent with different sets of electron/hole mobilities.

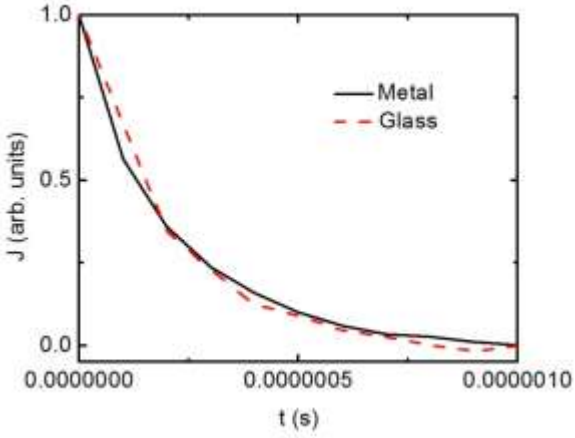

Figure 2.24 Transient photocurrents under bias of V_{app} = -2 V with illumination from metal and glass sides.

As discussed above, another discrepancy from predicted transient response is that the experiment results did not clearly show the changing point of the curve slope where the

hole current is become significant. It is simply because the noise to signal ratio is too big since the current is small. And it can be supported as the changing point is become more observable at a greater applied reverse bias (e.g. V_{app} = -2V, See Fig. 2.24), as it will more the cross over point to an earlier time while at higher current level.

2.5 Conclusion

In this chapter, we discussed the applications of characteristic absorption profiles to characterization of charge transports in Cu_2O/ZnO and organic solar cells. A value of ~430 nm for transport length of electron in electrodeposited Cu_2O is estimated by linking IPCE measurement to a simple drift and diffusion model. For a 1600 nm thick absorption layer, only photo generated carriers within this distance have a fair chance of being collected. The scale of nanostructures in this kind of solar cells should be designed with consideration of this critical length.

The utility of the local absorption profile in probing transport and recombination mechanisms was demonstrated in three OPV systems. From steady state light intensity measurements, the carrier that is restricted and causes the onset of recombination was determined. The mobility-lifetime product of the restricted carrier can then be estimated where similar values are achieved regardless of the generation profile. In transient photocurrent measurements, the two carrier transport process was demonstrated and the slow and fast carriers were distinguished by a simple model. Mobilities of both carriers were estimated. This work may inspire the broader usage of the local absorption profile to probe carrier transport properties and recombination mechanism in photovoltaic devices, especially those with thick active layers.

CHAPTER 3
NANOSTRUCTURED ORGANIC PHOTOVOLTAIC DEVICES

3.1 Background

As discussed previously, the nanostructured photovoltaic devices have the potential to solve the problem lies between adequate light absorption and efficient charge carrier collection. Recent years, photonic crystal nanostructures have been intensely studied in order to achieve additional light trapping in the OPV devices.[5,42,44,45,104–110] Many patterning techniques have been developed.[5] For example, nano-imprint lithography (NIL), a low cost method to fabricate large areas with submicron features, has been experimentally explored to create nanostructures in OPV devices.[5,42,44,106,111,112] Others have reported the use of laser interference lithography to pursue light trapping structures in OPV devices.[45,107]

In general, enhancements from nanostructures in OPV are frequently advanced. Most notably, Li et al. recently reported reported an increase from 7.59% to 8.79% in PCE of a low band gap material system using dual plasmonic nanostructures and an enhancement to 8.38% was achieved with a simple grating structure.[44] However, most of the previous results were reported by comparing nanostructured devices to non-optimized regular planar cells. For instance, OPV devices based on P3HT:$PC_{60}BM$ were one of the most

intensely studied BHJ systems in the last ten years. This material system had an average reported efficiency of 3.0% through 2010, but the bulk of reports in the past few years reported efficiencies between 3.8% and 4.0% with more than one hundred publications reporting efficiencies above 4%.[113] Despite these findings, all previous reported patterned OPVs were compared to control samples with efficiencies of only 2%~3.5%.[106,107,110,114–117] Very few researchers describe efforts to optimize flat control devices nor do they report results from a statistically significant number of samples in order to account for performance variability. The validation derived from such poor comparisons frequently rests on a normalized fabrication process for both patterned and flat cells, which at first glance, appears to be a fair test. In reality such comparisons are not sufficient to make the case for nanopatterning OPV devices. Patterned devices need to outperform the best flat devices.

Moreover, in addition to the inadequate comparisons, most of the previous works have focused on only light trapping while overlooking changes in charge transport that might result from patterning OPV devices. There is an unjustified assumption that pure light trapping structures will lead to OPV device enhancement. Only a few reports briefly mentioned the effect of patterning on electrical properties of the devices,[44,117] but the underlying causes were not studied in depth. Recently, Vervisch et al. suggested that there is a tradeoff between light trapping and uniformity of electric field distribution, which could be a key problem limiting the ultimate enhancement of pattering OPVs.[118] Besides, the effects on morphology inside the materials due to the patterning were not adequately studied. The morphologies may be changed from that in planar devices during the patterning process.

In this thesis, the patterned OPVs were fabricated by NIL techniques. Comparisons were performed among over 100 patterned OPVs and flat control devices made under multiple fabrication conditions. Tradeoff between light trapping and electrical deterioration was demonstrated. And the discussion was followed a complete electro-photonic simulation, which reveals the details of changes made by patterned structures. Additional discussion on morphology changes during patterning process were discussed as well.

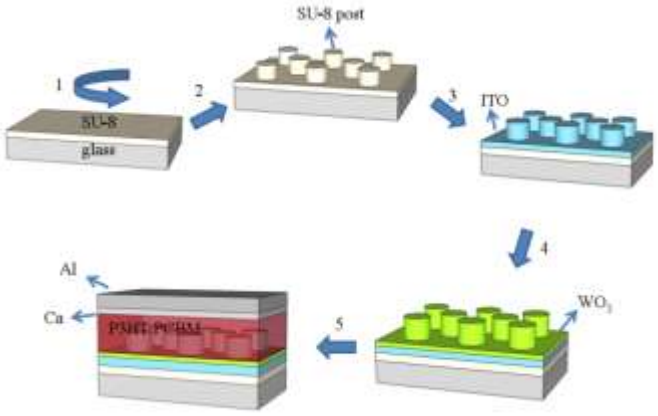

Figure 3.1 Schematic procedure of nanoimprinted OPV devices fabrication: 1. spin-coating SU-8 on glass substrate. 2. Emboss SU-8 by PFPE mold to form nanostructures. 3 Deposit ITO thin film on top of nanoimprinted SU-8 by PLD. 4. Evaporate WO_3 layer. 5. Spin-coat active materials and evaporate Ca/Al as electrode to complete the device. Reprinted with permission from Ref. 129. Copy Right 2013, IOP.

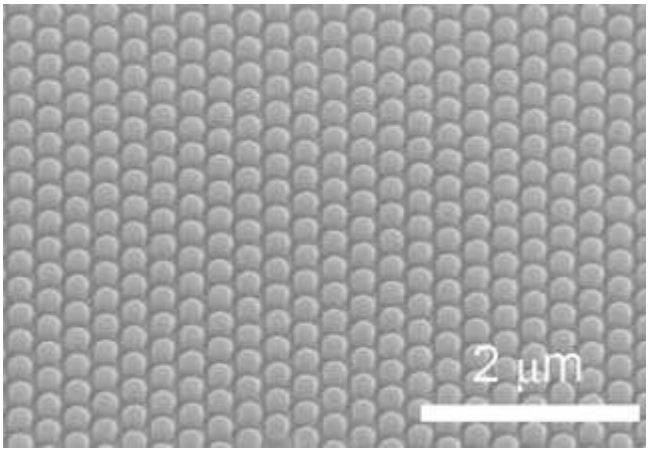

Figure 3.2 SEM image of patterned SU-8 coated with ITO/WO_3 prior to spin-coating active materials. Reprinted with permission from Ref. 129. Copy Right 2013, IOP.

3.2 Experimental Study of Nano-pattern Organic Photovoltaic Devices

3.2.1 Fabrication Technique

The NIL techniques were applied to pattern the active layer directly or substrates to realize nanostructured OPVs. To studied the optical-electrical effects in nanostructured OPVs, we chose NIL to pattern a commonly used negative transparent photoresist SU-8 (MicroChemicals) on glass substrates. As SU-8's optical properties are very close to those of glass, the SU-8/glass combination appears as an optically continuous nanostructured substrate. OPV materials can be casted or evaporated on top of these nanostructured substrates instead of being molded directly in order to avoid previously reported drawbacks of direct patterning of active layers, such as degradation, contamination, non-optimal configurations[107] and morphology changes (discussed below). In addition, this technique is suitable to other photovoltaic systems without modifying molding conditions. The overall fabrication process of the devices is schematically represented step by step in Fig. 3.1. To pattern SU-8, we used Pattern Replication in

Nonwetting Templates (PRINT)[119] with an elastomeric molding material based on perfluoropolyether (PFPE, by Liquidia Technologies) molds, because it can be easily released from the patterned replicas without complex surface functionalization,[5] thus allowing for easy, quick and high quality nano-replication over 6 cm^2. After molding, SU-8 is cured to become a robust layer that can be baked at 200 ^oC without any degradation. We used this process to replicate a two-dimensional hexagonal nano-scale array of sub-visible wavelength posts. The posts are ~180 nm wide and ~180 nm tall with center to center spacing of ~300 nm. On top of SU-8, indium tin oxide (ITO) film (100 nm) with resistivity of ~3×10^{-4} $\Omega\cdot$cm was deposited by pulsed laser deposition (PLD) at 200 ^oC under O_2 pressure of 20 mTorr. Tungsten trioxide (WO_3) was thermally evaporated to form buffer hole-injector[120] and it allows good subsequent spin casting of active polymer blend. Fig. 3.2 shows scanning electron microscopy (SEM) image of patterned substrate prior to spin-coating the blend. To run a complete systematical study, three different thicknesses (12, 22, 32 nm) of WO_3 were evaporated onto both patterned and flat devices prior to spin-coating the blend. The 1,2-Dichlorobenzene solution of P3HT:$PC_{60}BM$ (1:0.8 wt ratio with 25mg/ml P3HT, P3HT by Rieke Metals and $PC_{60}BM$ by Nano-C) was spin-coated at three different speeds as 800 RPM, 1000 RPM and 1200 RPM for 90 seconds with acceleration time of 6s, resulting in 3 different thicknesses (for the non-pattern samples) of ~230 nm, ~180 nm, and ~140 nm, respectively. These values were measured by spectroscopic ellipsometry from 3 different spots of the samples and later confirmed by SEM observations. The films were annealed at 140 ^oC on hot plate for 10 minutes. The flat and patterned films' surface roughness were characterized by tapping mode atomic force microscope (AFM) with root mean square ~2 nm. Calcium

and Aluminum were subsequently evaporated on top of the active layers to form the top electrode. On each sample, six solar cells with active area of 0.136 cm^2 (measured by microscope) and distance of > 0.25 cm between each other were fabricated. Figure 3.3 shows cross sectional SEM image of one patterned OPV device. All device measurements were carried out under purified nitrogen (< 0.1 ppm water and oxygen), except for optical reflection and angular IPCE measurements which were done in air after all other test were completed. AM 1.5 1 Sun measurements (with solar simulator and AM Mass 1.5 Global Filter from Newport, intensity was calibrated by reference solar cell from Newport before and after each measurement) and space charge limited current (SCLC) hole mobility measurements were conducted with a Keithley 2400 source-measure unit. IPCE measurements were conducted under the chopped light from a monochromator (from Newport). The device was connected to a lock-in amplifier to measure the AC voltage signal via a current to voltage preamplifier. Normal incidence reflections were measured using an upright microscope, while angular reflection/IPCE was conducted by using homemade system with calibrated Si detectors. IPCEs were also measured to confirm the exact short-circuit current related to the I–V curves from the solar simulator.

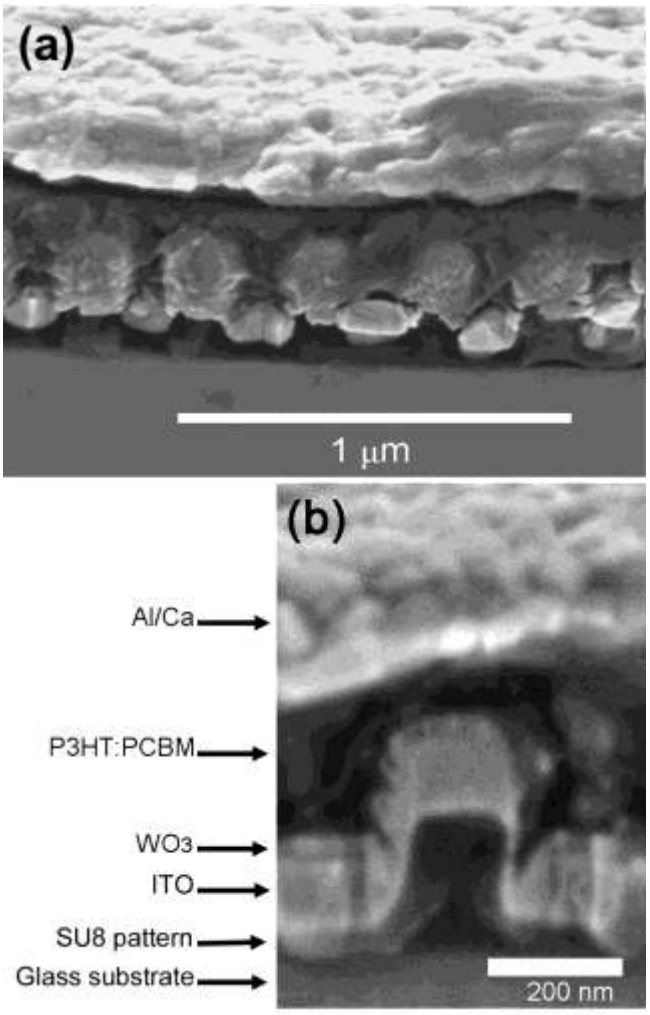

Figure 3.3 Cross-sectional SEM image of nanostructured OPV device. (a) Whole view of the cross-section. (b) Detail image of device configuration. Reprinted with permission from Ref. 129. Copy Right 2013, IOP.

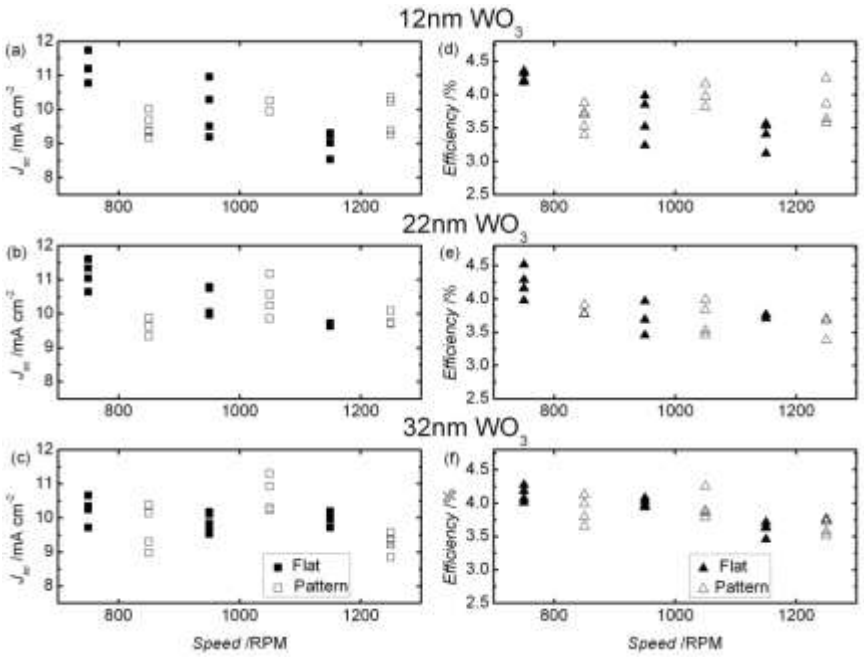

Figure 3.4 All OPV cell's J_{sc} (a ~ c) (solid squares are flat cells and open squares are patterned cells) and efficiencies (d ~ f) (solid triangles are flat cells and open triangles are patterned cells). Under certain fabrication condition, patterned device showed better performance, however no global enhancement. Reprinted with permission from Ref. 129. Copy Right 2013, IOP.

3.2.2 Device performance

Both patterned and flat devices have an open circuit voltage (V_{oc}) of ~ 0.6 V and fill factor (FF) ~ 0.6, with remarkably little difference between samples, and which are comparable to previous reported values in the literature[106,115,120]. Given the commonality of all of these metrics, the key factor that determined the devices' power conversion efficiency was the short circuit current (J_{sc}) only. After selecting out the devices with obvious fabrication quality issues, all of the cells' J_{sc} and efficiencies are shown in Fig. 3.4. Among all the observations, a few trends can be distinguished. In aggregate, the J_{sc} of the flat devices in this experiment decreased with the thickness of the active layer, as did the efficiencies.[113] However, this is not true for the patterned devices. J_{sc} peaks at

1000 RPM in the all the three groups with different thickness of WO_3. While comparing the average result of each group with different thickness of WO_3, we observed performance variations with the WO_3 thickness. But, there is no general trend for all the groups and the differences are in general small.

Focusing on the best performers, the best flat cell's efficiency was 4.52% and the highest J_{sc} is 11.74 mA cm^{-2}, while the best patterned cell's efficiency is 4.25% and the highest J_{sc} is 11.30 mA cm^{-2}. In addition, taking an average of all the cells in one group (i.e., the same WO_3 and blend spinning conditions), the best efficiency of the flat samples is 4.27% and the highest J_{sc} is 11.22 mA cm^{-2}, while the best average efficiency of a similar group of the patterned samples is 3.98% and the highest J_{sc} is 10.69 mA cm^{-2}. All of these figures are well above the average of reported P3HT:PC_{60}BM devices[113]. Furthermore, our nanostructured devices are overall better than the vast majority of previously reported patterned devices which were portrayed as successes in overcoming planar counterparts.[107,110,114–117] However, as can be seen from this complete data set, no significant enhancement is actually found relative to optimized flat devices. Very significantly, the best planar and best patterned devices arise with different fabrication parameters. This shows explicitly that holding fabrication parameters constant as the normalizing factor on comparing patterned and flat cells is misleading.

3.2.3 Angular and Polarization Characterization

In order to understand why the regular flat device still remains the best among all the devices fabricated, we focused first on the optical properties of the devices. As SEM micrographs sample only small areas, in order to judge the quality of the photonic structure and further explore the effects of nanostructures in OPV devices, we studied the

devices' angle dependent reflection and IPCE. For non-normal illumination on nanostructured devices, resonant mode splitting occurs which generates absorption enhancements that show the signature photonic behavior. Simulations of the photonic devices based on the materials and geometrical parameters (Fig. 3.5) predict the presence of quasi-guided modes [121] where strong light confinement should give rise to localized reflection minima. This prediction confirms that the quality and parameters of the experimental devices were close to the idealized structure presented above in Fig. 3.1. Fig. 3.6 shows that the experimentally observed reflection minima at the blend absorption tail move towards λ = 600 nm with incident angle changing from 60^{o} to 30^{o} eventually disappearing. This reflection minimum results in a local, small IPCE enhancement. The local angular IPCE enhancements were found in both polarizations, because the nanostructure geometry is periodic in both lateral dimensions. As expected, this photonic behavior was found in all patterned devices while it was absent in the flat ones. The demonstration of this unmistakable photonic phenomenon confirms faithful replication of the design and that the optical quality and the manufacturing defects are not the reason patterned devices failed to outperform the best flat devices.

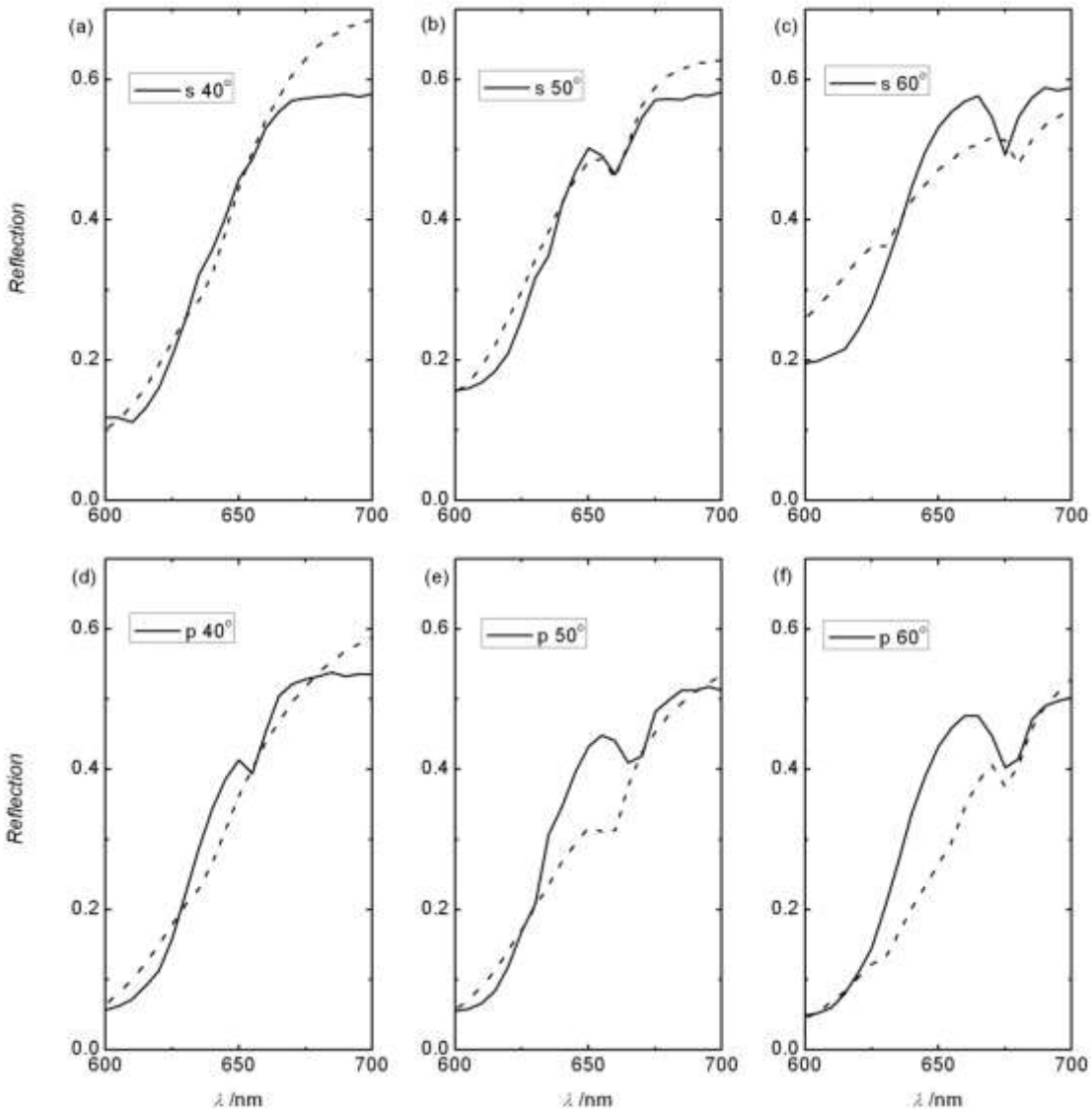

Figure 3.5 Experimental and simulated angular reflections of the patterned device with 12 nm WO_3 and spun at 800 RPM. Solid lines are experimental measurements. Dashed lines are simulated reflections. Mismatch between simulations and experiments beyond $\lambda >$ 650 nm is due to the larger uncertainty in the P3HT absorption constants tail beyond this point.[122] Reprinted with permission from Ref. 129. Copy Right 2013, IOP.

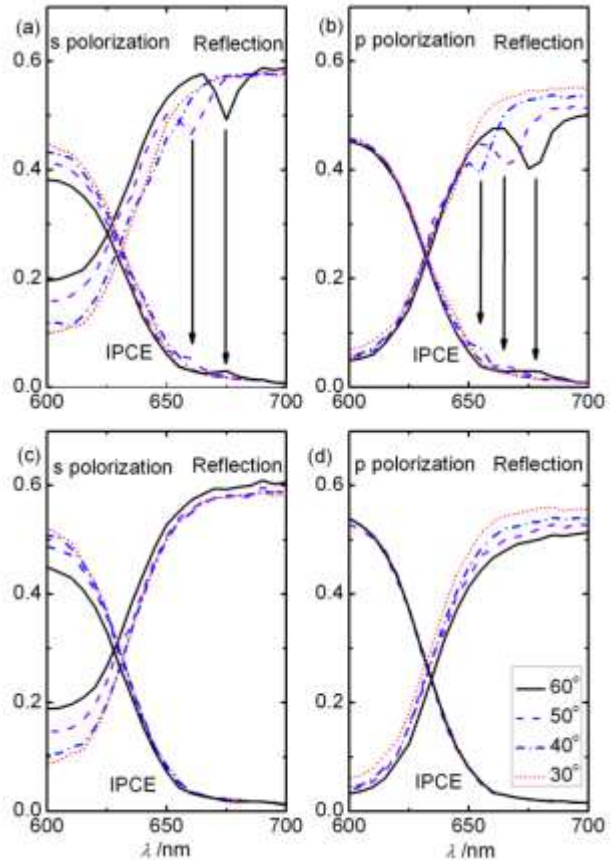

Figure 3.6 Angular Reflections and IPCEs in both p and s polarization of the flat and patterned devices with 12 nm WO_3 and spun at 800 RPM. (a) and (b) are the patterned devices. (c) and (d) are the flat devices. Local IPCE enhancements are indicated by arrows. Reprinted with permission from Ref. 129. Copy Right 2013, IOP.

3.2.4 Normal Incidence Reflection and IPCE

Given the WO_3 and ITO transparencies, to the first order, lower device reflection should correspond to higher absorption in the active layer of patterned devices. Normal incidence reflection measurements and IPCE characterizations are performed on all of the devices. Fig. 3.7 shows both experimental and simulated normal incidence reflections of the device group with 12 nm WO_3. The other two groups with 22 nm and 32 nm WO_3 have similar results. All of the patterned devices exhibit relatively low reflection,

especially at wavelengths ranging from λ ~450 nm to λ ~550 nm where P3HT:$PC_{60}BM$ absorbs strongly. However, the 800 RPM flat devices reached similar levels of low reflection, comparable to all of the patterned ones. When narrowing the comparison to the 800 RPM flat and patterned devices, the flat devices exhibited lower reflection from ~550 nm to 600 nm. Taking all of these observations together showed that the devices from 1000 RPM and 1200 RPM group did benefit optically from nanostructures, but the optimized flat devices at 800 RPM had similar optical performance. From this perspective, while a nanostructured sample could have a lower reflection than a flat sample under certain control parameters, one could not conclude that the nanostructured devices have significant optical enhancement over all possible flat devices. Photonic parameter optimization is needed to obtain an absolute best optical performance. As it will be shown below, this is possible but unfortunately, such photonic optimization is not enough. As it can be appreciated in the 1000 RPM group, the patterned devices have the lowest group reflections but this does not translate into additional electrical current gains (See Fig. 3.8). This discordance also happened in other patterned and flat groups. The exciton generation profile [56] or other carrier transport issues related to geometrical factors may not be favorable for the charge carriers to be swept out despite good FFs and V_{oc}s in the devices.

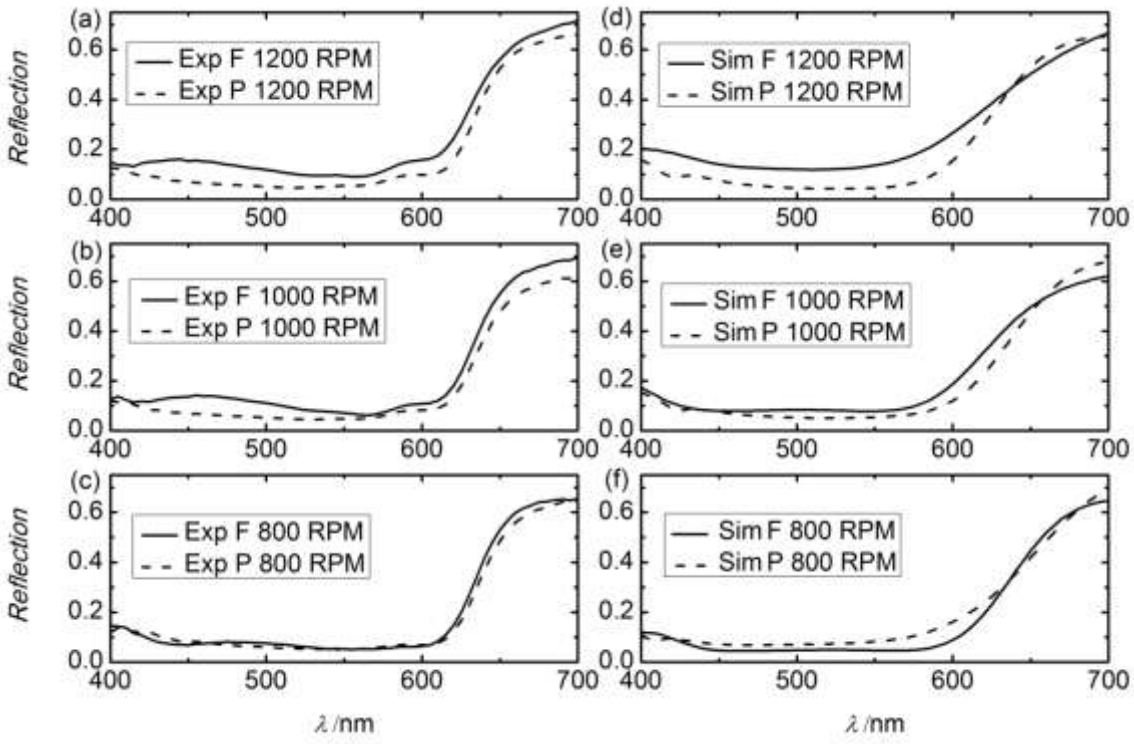

Figure 3.7 Experimental (a ~ c) and simulated (d ~ e） reflections from the glass sides of both the flat and patterned devices with 12 nm WO_3. Solid lines are flat samples' reflections. Dashed lines are patterned samples' reflections. Reprinted with permission from Ref. 129. Copy Right 2013, IOP.

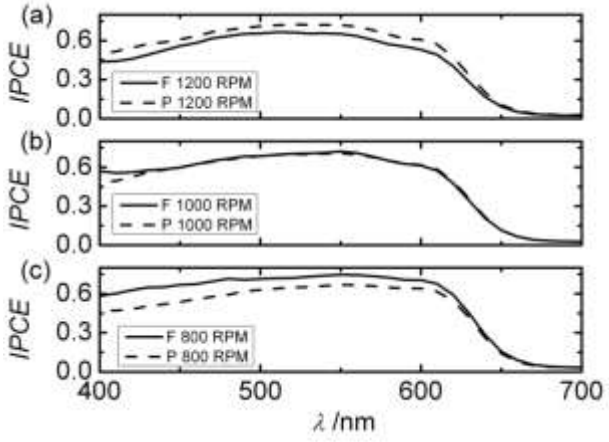

Figure 3.8 IPCEs from glass sides of both the flat and patterned devices with 12 nm WO_3. Solid lines are flat samples' IPCEs. Dashed lines are patterned samples' IPCEs. Reprinted with permission from Ref. 129. Copy Right 2013, IOP.

3.2.5 SCLC Hole Mobility Measurement

We now direct our attention to the electronic integrity of the devices. As discussed before, the holes are believed to be the slower and limiting carriers in the P3HT:PC_{60}BM system [56]. Therefore, evaluation on hole transport both in flat and patterned films are performed by using hole-dominated diodes.[44] The current-voltage characteristics of the hole-only diodes have shown a square dependence of current on voltage (see Fig. 9), from which we can estimated the hole mobility using[44,123]

$$J = \frac{9}{8}\varepsilon_0 \varepsilon \mu_0 \frac{V^2}{L^3} \tag{3.1}$$

where J is the current density, ε_0 is the permittivity of free space, ε (=4) is the dielectric constant of the P3HT:PC_{60}BM blend[124], μ_0 is the mobility, V is the internal built-in voltage, and L is the thickness of the active layer. The flat and patterned devices are found to be characterized by very similar hole mobilities, 6.66×10^{-4} cm^2 V^{-1} s^{-1} and 8.83×10^{-4} cm^2 $V^{-1}s^{-1}$, respectively. (For the patterned device, an average thickness was used as an approximation in this simple formula as the patterning intrinsically induces blend thickness differences.) Although mobilities of the holes and electrons are reported to be enhanced by patterning, the reason for that is not clear.[44] The mobility difference between patterned and flat devices indeed favors the former but only slightly. This together with the good FFs and V_{oc}s lead us to believe that device construction, including morphology, is equally good in the flat and patterned devices. So, the reason behind the unfulfilled overall enhancement must be searched for elsewhere.

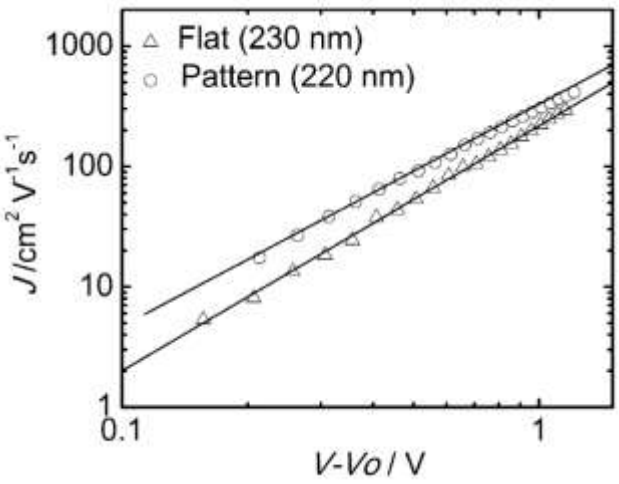

Figure 3.9 SCLC measurement for hole mobility measurement. Solid lines are fittings to equations to obtain estimation of hole mobility. The averaged patterned device thickness is estimated from pattern geometry. Reprinted with permission from Ref. 129. Copy Right 2013, IOP.

3.3 Electro-photonic Simulation of Nanostructured OPV

3.3.1 Demonstration of Trade-off between Light Trapping and Charge Collection

Numerical simulation of the charge transport in organic bulk heterojunction solar cells may shed light on the loss mechanisms in patterned devices and give indications as to why they do not outperform the best flat cells. We used a mathematical model based on an effective medium approximation of the bulk heterojunction material;[125,126] the electron and hole number densities n, p [m^{-3}], and the electric potential ψ [V] in the photoactive material, are related by the classical semiconductor equations.[127] The semiconductor equations form a nonlinear system of three partial differential equations involving charge carrier drift in the electric field, $-\nabla\psi$ [V m^{-1}], as well as diffusion, which yields expressions for the charge carrier fluxes, J_n, J_p [$m^{-2}s^{-1}$]. Poisson's equation for electrostatics relates the electric potential to the charge density $-q(n-p)$ [C m^{-3}],

where q denotes the elementary charge. The source term in this model is given by the net charge carrier generation rate density which incorporates exciton generation due to light absorption, exciton dissociation into free charge carriers, as well as charge carrier recombination to excitons and exciton decay. The boundary values of n, p, and ψ are prescribed; they depend on the bias voltage. A combined electro-photonic simulation, where the exciton generation rate density is computed from an auxiliary optics simulation [121], may be used to evaluate various patterned organic bulk heterojunction solar cells. The full details on this approach shall be reported elsewhere [128] – here we only present simulation results for two 2D patterned bulk heterojunction solar cell devices with ridge-patterned front electrodes. These are chosen as representatives of different light trapping and carrier harvesting characteristics.

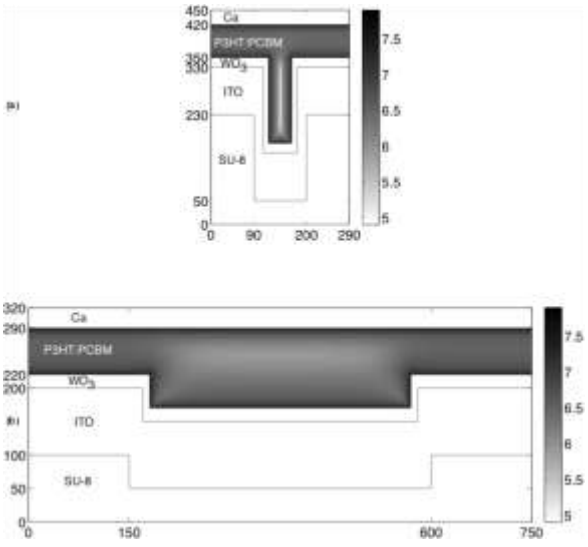

Figure 3.10 Logarithm to base 10 of the electric field strength [V m^{-1}] at maximum power in two bulk heterojunction solar cell devices with ridge-patterned front electrodes. The devices are closed by a glass layer in the front and by an aluminum layer in the back. Length units are nanometers. The electric field is weaker in the ridge part because of the larger distance between the electrodes. The induced losses may outweigh the gain in light absorption achieved by the photonic crystal structure. Reprinted with permission from Ref. 129. Copy Right 2013, IOP.

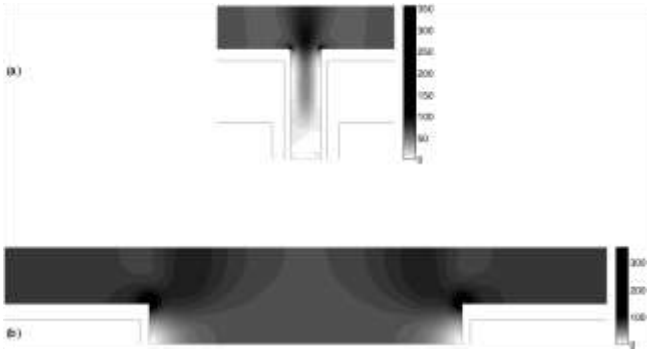

Figure 3.11 Current density [A m^{-2}] at maximum power in the two patterned solar cell devices (a) and (b). The current density is low in regions of the deeper ridge pattern, which deteriorates the charge transport properties of device (a). Reprinted with permission from Ref. 129. Copy Right 2013, IOP.

In Fig 3.10 we show the computed electric field at maximum power in a cross section of the two devices; this figure also illustrates the device geometries, and in Table 1 we summarize computed performance factors. The two patterned solar cell devices have similar amounts of P3HT:PC_{60}BM bulk heterojunction material. While the light absorption in the active material is lower in device (b) than in device (a), device (b) apparently has better charge transport properties than device (a), which ultimately results in higher power conversion efficiency. This indicates that it is not sufficient to focus only on improvements of the optical device properties by employing a photonic crystal structure which enhances the light absorption. These structures may, on the other hand, deteriorate the electrical properties of the device.[118] Both the exciton dissociation and charge carrier collection efficiencies are similar in the devices (a) and (b), whereas the main difference between the two devices is in the collection-to-output efficiency (Table 1). This efficiency factor is computed by comparing the maximum power [W m^{-2}] with the charge carrier collection rate [$m^{-2}s^{-1}$] multiplied by the energy qV_{mp} [J], where V_{mp} [V]

denotes the bias voltage at maximum power. The collection-to-output efficiency is smaller than 1 if charge carriers are collected at the "wrong" electrode, i. e. electrons at the anode or holes at the cathode. The spurious charge carrier flux will decrease the total current through the electrodes and therefore the output power, compared to the value expected from the charge carrier collection rate.

In Fig. 3.11 we show the Euclidean norm of the current density $J = -q(J_n - J_p)$ [A m^{-2}] computed from the steady-state charge carrier fluxes at maximum power for both devices. The current density is low near the electrode in the ridge as well as everywhere in the deeper parts of the ridge region; the current through the electrode boundary will therefore be low in that region. Charge carrier pairs generated in these regions will not be swept out from there, which in the case of device (a), is supposed to lead to a larger spurious flux of electrons through the anode, thus explaining the lower performance despite its better optical features. Even in cases where devices are overall enhanced, the percentage of current increase may not be as much as that of absorption.[44]

Table 3.1 Computed performance factors for the two patterned solar cell devices (a) and (b).

	unit	(a)	(b)
active material volume	10^{-9} $m^3 m^{-2}$	101	96
light absorbed in P3HT:$PC_{60}BM$	W m^{-2}	283	263
short circuit current	A m^{-2}	78.2	93.6
open circuit voltage	V	0.578	0.578

fill factor	–	0.690	0.627
power conversion efficiency	%	3.27	3.55
exciton dissociation efficiency at maximum power	%	82.0	81.0
charge carrier collection efficiency at maximum power	%	85.3	85.1
collection-to-output efficiency at maximum power	%	77.6	96.2

3.3.2 Exploration of Patterning in 2-D Ridge-patterned Back Electrode OPVs

The results above experimentally demonstrate that realizing a global maximum is not a simple task as electrical deterioration counteracts light absorption gains,[129] and the simple comparison by simulation direct us to theoretically explore the effects of patterning. Therefore, we applied the electro-photonic model discussed previously to study both electrical and optical effects arising from patterning a simple grating structure in Poly[[4,8-bis[(2-ethylhexyl)oxy]benzo[1,2-b:4,5-b']dithiophene-2,6-diyl][3-fluoro-2-[(2-ethylhexyl)carbonyl]thieno[3,4-b]thiophenediyl]]:[6,6]-phenyl C_{71}-butyric acid methyl ester (PTB7:$PC_{70}BM$) devices. The PTB7:$PC_{70}BM$ solar cell was demonstrated to have >9% efficiency in experiment.[15] It is found that for the most part, optical absorption improvements are indeed limited by enhanced electrical losses. Optimized device structures that overcome this tradeoff are proposed and their detailed electro-optical characteristics are discussed below. Additionally, the overall conclusions were tested with a distinct set of parameters that represent devices with P3HT: $PC_{60}BM$ blend, the most widely studied OPV system.

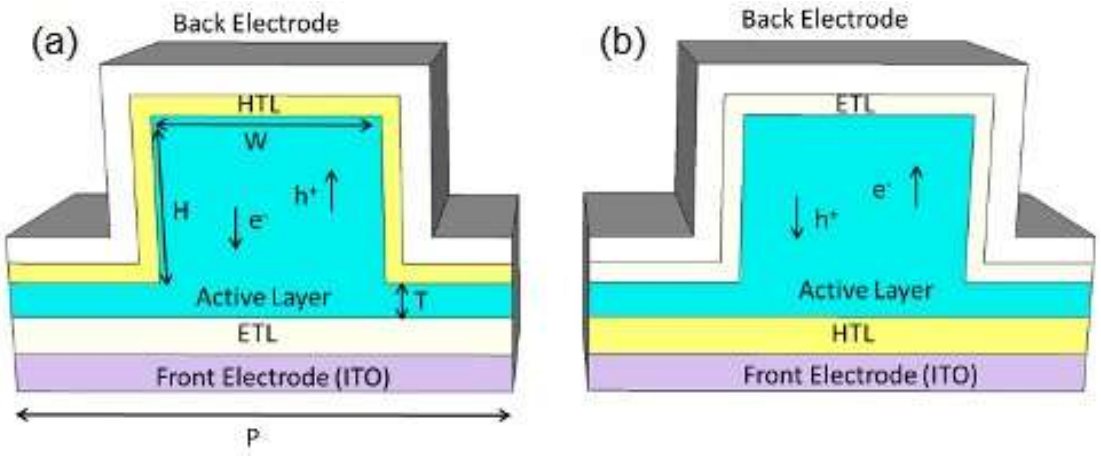

Figure 3.12 Sketch of the inverted and conventional grating structures: (a) In an inverted device, electrons are collected in the front electrode after being selected by the electron transport layer (ETL) and holes are collected in the back electrode after being selected by the hole transport layer (HTL) in the inverted device (b) The opposite charge transport direction define the conventional structure. Dimensions W,T, H and P were varied numerically. Reprinted with permission from Ref. 126. Copy Right 2013, American Institute of Physics.

Table 3.2 Parameters used for Simulation of PTB7:$PC_{70}BM$ devices.

μ_n ($m^2 V^{-1}s^{-1}$)	5.80×10^{-7}	e/h pair separation distance (m)	1.8×10^{-9}
μ_p ($m^2 V^{-1}s^{-1}$)	1.70×10^{-7}	e/h pair decay rate (s^{-1})	2×10^{-4}
Built in Voltage (eV)	1.15	Dielectric constant	3.4

Here we studied 2D ridge pattern/gratings in both inverted and conventional BHJ organic solar cell devices with ridge-patterned back electrodes in the OPV material systems (Fig. 3.12). The devices' electrical properties used in the simulation are listed in Table 3.2 and are estimated based on recent literatures and fittings to experimental results.[87,130–132] Optical properties were obtained from our own ellipsometry measurements. In an inverted (Fig. 3.12a) OPV, the device's structure is a stack of ITO /

poly[(9,9-bis(3 ´-(N,N-dimethylamino)propyl)-2,7-fluorene)-alt-2,7-(9,9–dioctylfluorene)] (PFN)/Blend/tungsten trioxide (WO_3) /Ag (or Al). The conventional (Fig. 3.12b) structure is ITO/PEDOT:PSS/Blend/Ca/Ag(or Al). The choice of electron/hole transport layers (ETL/HTL) and electrodes were studied experimentally.[44,129–131,133–135] We simulated both flat and patterned devices for comparison and discussion.

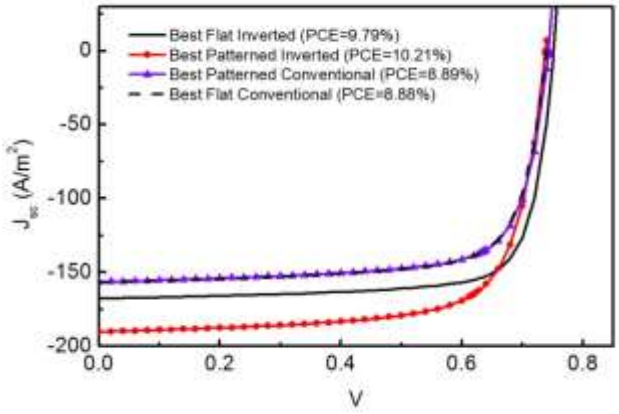

Figure 3.13 Simulated current density vs. applied electric potential characteristics for best performing PTB7:PC_{70}BM (flat and patterned) devices. Reprinted with permission from Ref. 126. Copy Right 2013, American Institute of Physics.

As a benchmark, flat devices were simulated first. PTB7 devices with Ag electrode are used as an example for discussion. (P3HT-based device results are analogous). Calculated short circuit current density and open circuit voltage agree well with previously published experimental results.[113,129–131,134–136] Fig. 3.13 shows the J-V curves of the most efficient PTB7/Ag devices for the conventional and inverted flat devices structures, 8.88% and 9.79% respectively. The slightly higher simulated fill factors (*FF*s) probably result from ignoring the parasitic resistance of substrates,[87,118] which will not affect our discussion of effects from patterning the active layer. In Fig. 3.14, the dilemma

between the light absorption and free carrier transport is clear in the flat case. The optical absorptions approach a maximum value as the thicknesses increase, while the efficiencies start to drop when the active layer become larger than 200 nm thick.

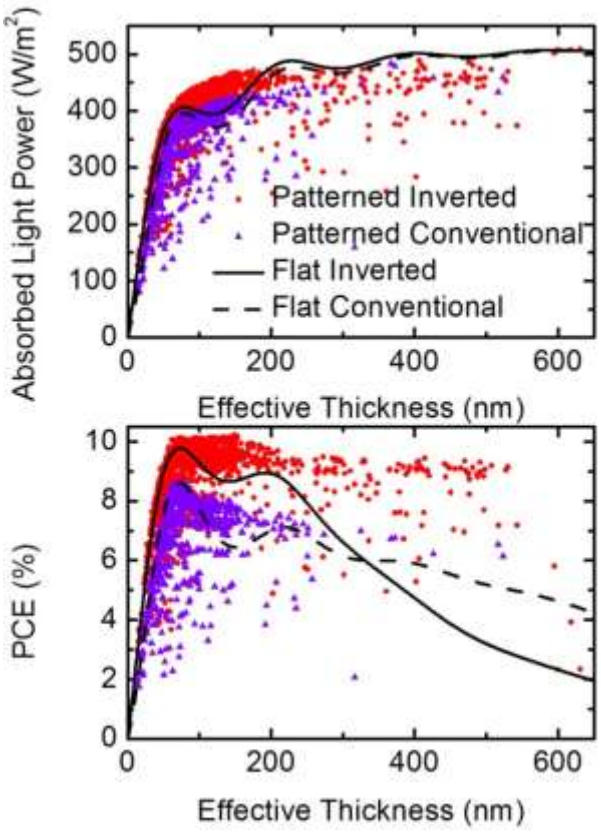

Figure 3.14 Absorption vs. effective thickness (a) and efficiency vs. effective thickness (b) of both inverted (ITO/PFN/PTB7:$PC_{70}BM$/WO_3/Ag) and conventional (ITO/PEDOT:PSS/PTB7:$PC_{70}BM$/Ca/Ag) devices in the flat and patterned structures. Reprinted with permission from Ref. 126. Copy Right 2013, American Institute of Physics.

Fig 3.13 and 3.14 also show the J-V (only the best ones) and overall-efficiency results for patterned conventional and patterned inverted structures after exploring a wide parameter space. The computer algorithm automatically varied four parameters (i.e.

grating period P, ridge height H, width W and flat layer thickness T) and optimized the structures to find the highest possible efficiency in both inverted and conventional devices. Along this optimization process, each simulated structure performance is recorded. To have a clear comparison between patterned and flat devices, the PTB7 devices' absorptions and efficiencies are also plotted against the effective thickness of the active layer, which is the average thickness over one period of the grating. Compared to the optimal flat device, there are many structures that significantly increase the absorption without adding much thickness (See Figure 3.14a). The absorption enhancement spectra of these devices are comparable to previous published experimental results.[137] However, the efficiency can only be improved by a small amount (relative 4%) from 9.79% to 10.21% by grating structures in the inverted case. The efficiency enhancement is more trivial in the conventional case. We can see that as efficiency declines with layer thickness in flat devices, many pattern structures are predicted to be able to maintain above 9% efficiency at large effective thicknesses. However, an enhancement compared to the most efficient flat layer device is found in much fewer grating structures. This is easier to appreciate in Fig. 3.15 (output-power/absorbed-power vs. absorbed-power/input-power), where many patterned structures enhance optical absorption (i.e. absorbed power to input power ratio greater than that of the most efficient flat cell). But, nevertheless the output power to absorbed power ratios are lower than the flat device's value, which means the charge transport is degrading the devices' performance. Hence, the number of patterned devices outperforming the most efficient flat one is actually quite limited. The results of P3HT:$PC_{60}BM$ devices are presented in Fig. 3.16 as well.

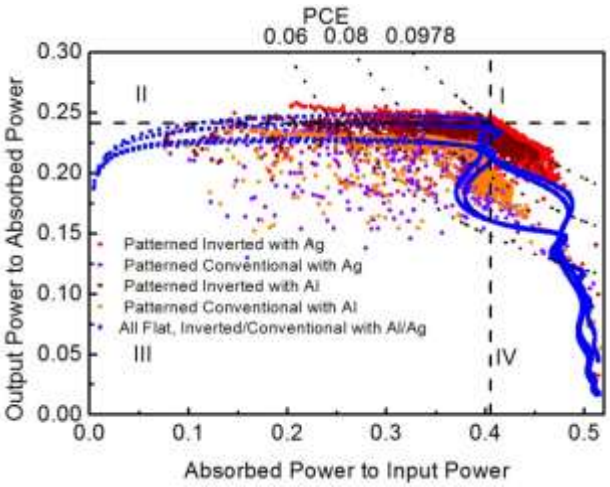

Figure 3.15 Efficiency plots: The flat and patterned PTB7 devices' output power to absorbed power vs. absorbed power to input power. The product of these two values is the efficiency of one device. Intersection of the dash lines marks the best flat device. Region I: both electrical and optical enhancements. Region II: Electrical enhancement but optical deterioration. Region III: both electrical and optical deteriorations. Region IV: optical enhancement but electrical deterioration. Reprinted with permission from Ref. 126. Copy Right 2013, American Institute of Physics.

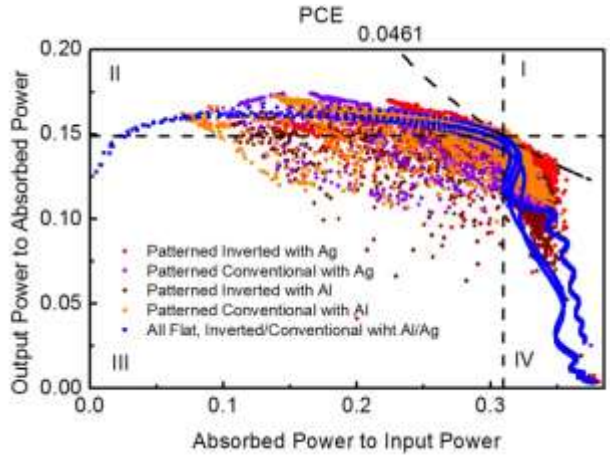

Figure 3.16 Efficiency plots of P3HT:$PC_{60}BM$ devices. Reprinted with permission from Ref. 126. Copy Right 2013, American Institute of Physics.

The overall efficiency in the patterned devices does not follow the absorption increase (or decrease), because the grating structures affect the charge carrier collection as well. Choosing inverted PTB7 OPVs (ITO/PFN/PTB7:$PC_{70}BM/WO_3$/Ag) as an example for

discussion, let us focus on the effective thickness less than 300 nm where the simulation is crowded with high efficiency devices. The computed dissociation probabilities of electron-hole pairs are fairly the same in patterned and flat devices and hence the electrical effect of patterning can be mainly revealed from carrier collection or transport. Fig 3.17 shows that the improvements of light absorption and carrier collection efficiency (number of collected carriers to number of generated carriers, η) do not occur at the same place in most of the cases. Almost all the carrier collections efficiencies of the devices with effective thickness less than 160 nm are deteriorated by patterning, while most of the optical enhancements occur in this range. The carrier collection efficiency is improved by patterning the devices with a large volume but optical enhancement is considerably less. The product of these two ratios is a combination of optical and electrical effects of patterning, which will clearly reflect the possible enhancement in terms of efficiency. The maximum of that value locates at the effective thickness of ~140 nm (Fig. 3.18). It agrees that the largest relative enhancements also occur around 140 nm, where is a local minimum of the efficiencies of the flat devices (Fig. 3.14b).

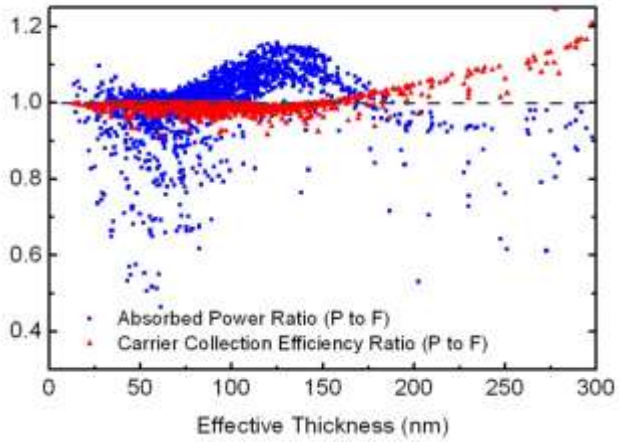

Figure 3.17 The ratios of absorbed power of the patterned devices to that of the flat devices with the same volumes （blue） and the ratios of carrier collection efficiency to that of the flat devices with the same volumes (red). Reprinted with permission from Ref. 126. Copy Right 2013, American Institute of Physics.

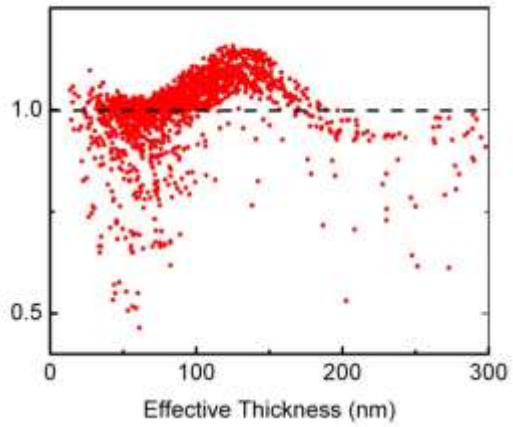

Figure 3.18 Product of the ratios shown in Fig 3.17. Reprinted with permission from Ref. 126. Copy Right 2013, American Institute of Physics.

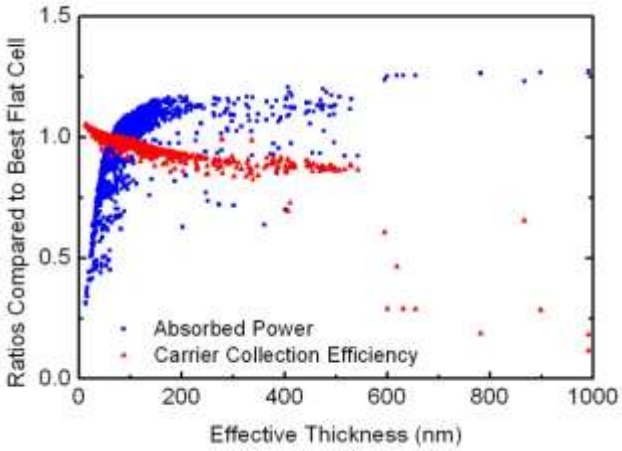

Figure 3.19 The ratios of absorbed power of patterned devices to that of the best flat device and the ratios of carrier collection efficiency to that of the best flat device. Reprinted with permission from Ref. 126. Copy Right 2013, American Institute of Physics.

The comparison between patterned and flat devices with the same volume (i.e. effective thickness) does not necessarily lead to an overall optimal configuration. It is important to compare all the patterned devices against the flat one with the highest efficiency. In Fig. 3.19, similarly one can see that the optical enhancements are limited by the electrical deterioration when the patterned devices were compared against the best flat one. This combined effect makes the best pattern device to be the one with p = 410 nm, h = 210 nm, w = 240 nm, t = 80 nm and effective thickness ~150 nm. Although the best patterned device absorbed 14.7% more power than the best flat one, its η value is 89.17%, which is lower than the η (= 93.75%) of the best flat one. The efficiency only outperforms the best flat device by ~4% (due to a lower V_{oc} as well). This enhancement is considerably less than the 17.5% improvement when compared with a non-optimized flat device of equal active volume (150 nm thickness).

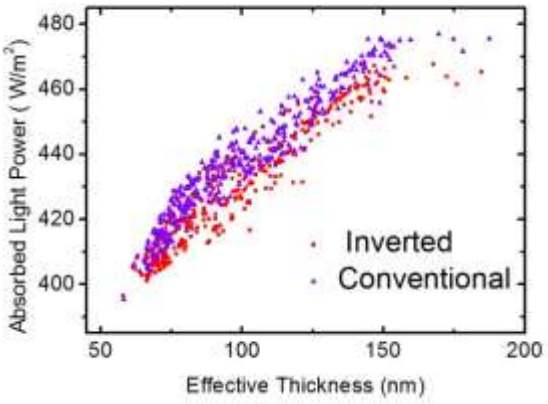

Figure 3.20 Absorbed power of the 400 patterned inverted (ITO / PFN / PTB7:$PC_{70}BM$ / WO_3 / Ag) and conventional (ITO / WO_3 / PTB7:$PC_{70}BM$ / PFN/Ag) structures studied. Reprinted with permission from Ref. 126. Copy Right 2013, American Institute of Physics.

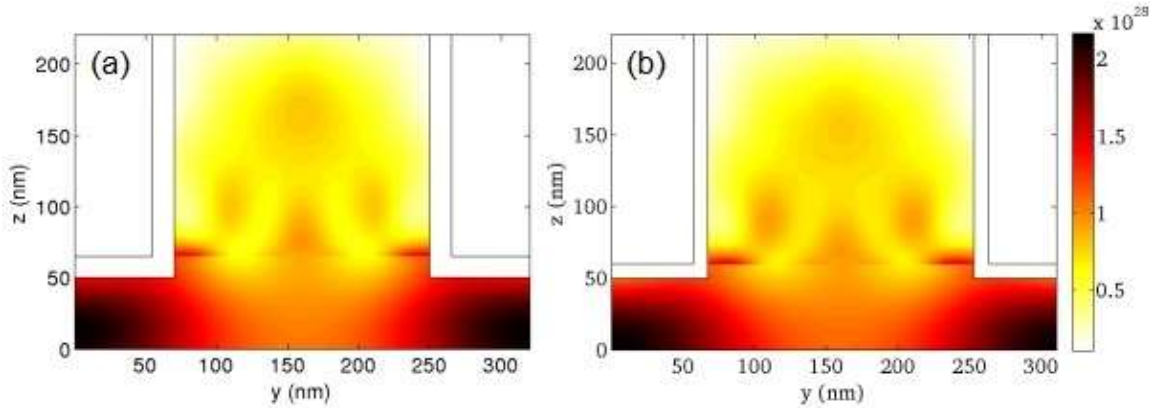

Figure 3.21 Electron-hole pair generation density ($m^{-3}s^{-1}$) profile of active layers in one inverted device (a) (ITO/PFN/PTB7:$PC_{70}BM$/WO_3/Ag) and one conventional device (b) (ITO/WO_3/PTB7:$PC_{70}BM$/PFN/Ag). Reprinted with permission from Ref. 126. Copy Right 2013, American Institute of Physics.

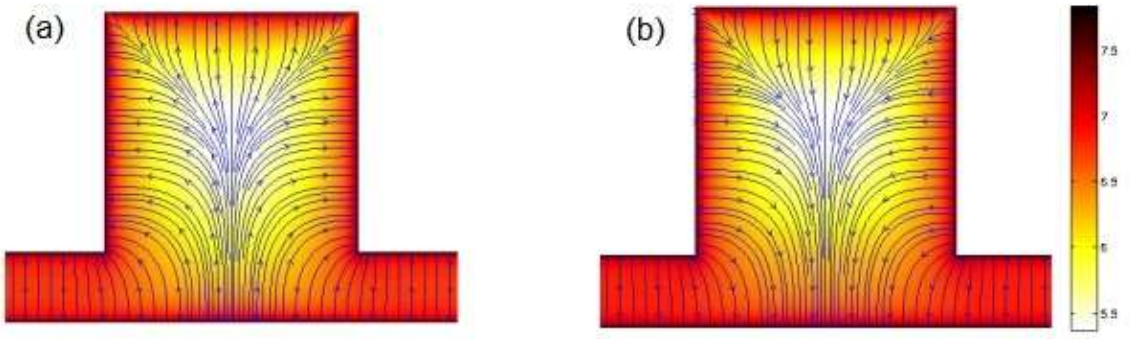

Figure 3.22 Log_{10} of the electric field (V m^{-1}) profile of the inverted (a) and conventional (b) devices shown in Figure 3.22. Reprinted with permission from Ref. 126. Copy Right 2013, American Institute of Physics.

It is observed in Fig. 3.14 and 3.15 that patterning is more beneficial in inverted devices than in conventional configurations. To explore the internal field effects of patterning, we compared inverted (ITO/PFN(10nm)/PTB7:$PC_{70}BM$/WO_3(15nm)/Ag) and conventional (ITO/WO_3(15nm)/PTB7:$PC_{70}BM$/PFN(10nm)/Ag) structures with each other and with flat structures. The blend in either of these two structures absorbs a similar amount of light (Fig 3.20). The difference between the inverted and conventional devices must come from the electrical effects. We simulated 400 nanostructure configurations in which the inverted patterned devices outperform the best flat inverted cell of PTB7: $PC_{60}BM$ in terms of overall efficiency. The electron-hole generation profiles (approximated as charge generation map) and electric field over the cross section of one typical such best structures are plotted in Fig. 3.21 and in Fig. 3.22, respectively. One can see that in the ridge region there is a weak electric field area, populated with many free carriers. This agrees with previous studies and limits enhancement of efficiency by light trapping patterning of OPVs.[118,129] The holes are assumed as slower carriers in this type of devices.[130] Due to the weak electric field in the ridge region, it is closer, and

hence easier for holes in that area to be collected by the back electrode (Ag/Al) on the ridge sides in the inverted devices. In conventional devices, on the other hand, the holes need to go to the front electrode, which is relatively farther away. This, we believe, is one possible reason that inverted patterned devices work better than the conventional ones in most cases (Figure 3.23a).

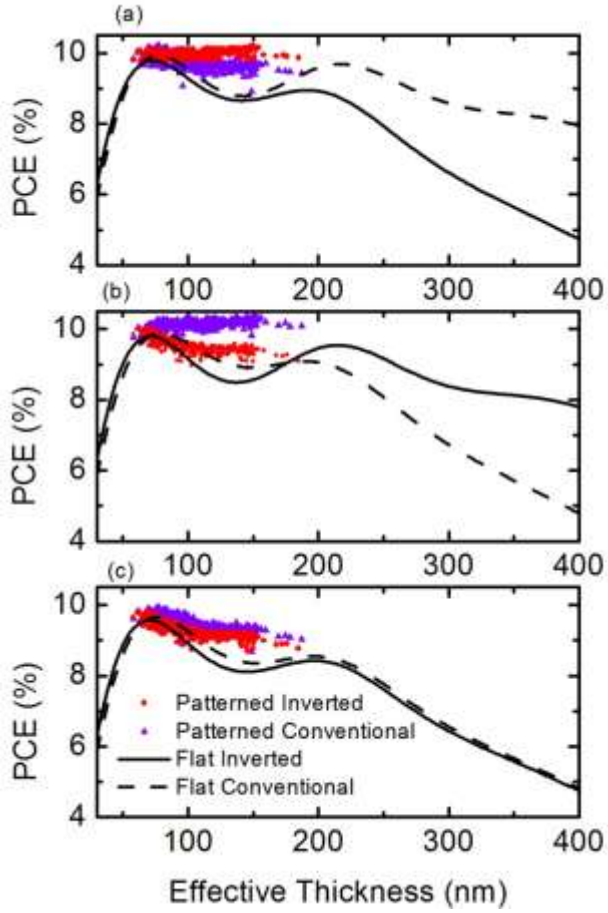

Figure 3.23 Simulations of patterned inverted devices (ITO/PFN/PTB7:$PC_{70}BM$/WO_3/Ag) and conventional devices (ITO/WO_3/PTB7:$PC_{70}BM$/PFN/Ag). Black Solid and dash lines are the flat inverted and conventional devices respectively. Red round dots are the patterned inverted devices and violet triangle dots are the patterned conventional devices. a) electron mobility is greater (μ_n = 5.8×10^{-7} m^2/V s, μ_p = 1.7 $\times10^{-7}$ m^2/V s). b) hole mobility is greater (μ_n = 1.7×10^{-7} m^2/V s, μ_p = 5.8 $\times10^{-7}$ m^2/V s). c) electron and hole moblities are equal (μ_n = 1.7×10^{-7} m^2/V s, μ_p = 1.7 $\times10^{-7}$ m^2/V s). Reprinted with permission from Ref. 126. Copy Right 2013, American Institute of Physics.

The pattern also has important effects in the internal charge current densities. The charge carrier flux is a combination of drift and diffusion contributions,

$$J_n = J_{drift} + J_{diffusion} = \mu_n n \nabla \psi - D_{\mathrm{n}} \frac{dn}{dx} \tag{3.2}$$

$$J_p = J_{drift} + J_{diffusion} = -\mu_p p \nabla \psi - D_p \frac{dp}{dx} \tag{3.3}$$

The D_n and D_p are the diffusion coefficients of electron and hole, respectively. We plot electron/hole flux over the cross section (Fig. 3.24). It is noted that an observable electron back flow is found at the ridge corners in inverted devices while the hole back flow is found in the conventional one. The diffusion current is to the opposite direction of drift current and overwhelms the drift current at those corners. The hole current flux in the conventional case is more affected than the electron current flux in the inverted case, which can be related to the slower hole mobility and hence a smaller drift term. This was confirmed by simply running simulations where the electron and hole mobilities are exchanged as input to the numerical program (Fig. 3.25).

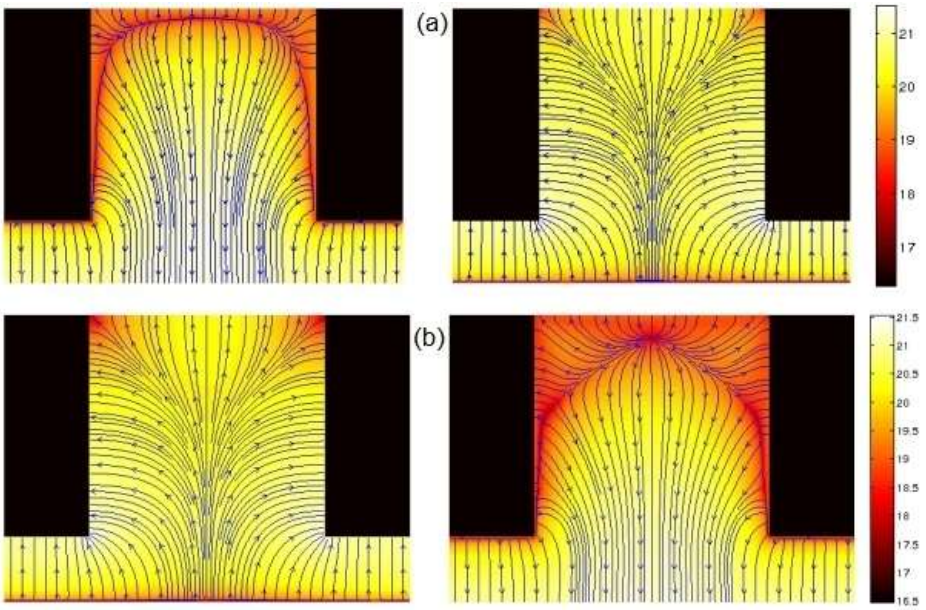

Figure 3.24 Electron (left) and hole (right) flux ($m^{-2}s^{-1}$) (a) inverted devices (b) conventional devices when electron mobility are greater than the hole mobility (μ_n = 5.8×10^{-7} m^2/V s, μ_p = 1.7 $\times10^{-7}$ m^2/V s). Reprinted with permission from Ref. 126. Copy Right 2013, American Institute of Physics.

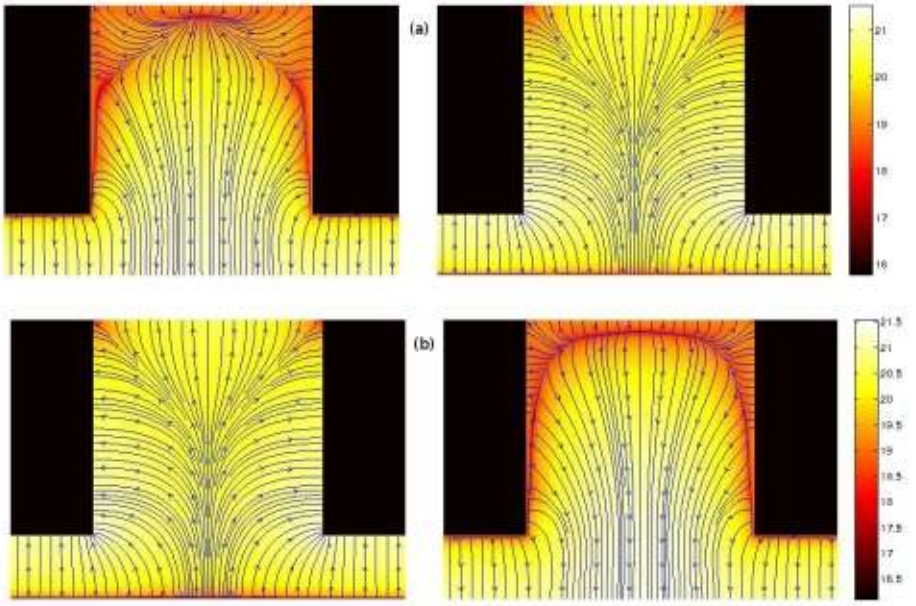

Figure 3.25 Electron and hole flux ($m^{-2}s^{-1}$) (a) inverted (b) conventional when the hole's mobility are greater than the electron's (μ_n = 1.7 $\times10^{-7}$ m^2/V s, μ_p = 5.8×10^{-7} m^2/V s). Reprinted with permission from Ref. 126. Copy Right 2013, American Institute of Physics.

Efficiency goes down faster in flat inverted devices than in flat conventional devices as thickness increases (Fig 3.23a) because the slower charge carriers (i.e. holes) are generated farther away from the back electrode, where holes are collected in the inverted devices.[16,56] In contrast, most of the patterned inverted devices have higher efficiencies comparing with their conventional counterparts. And the most efficient device has an inverted structure. However, if the input hole and electron mobilites are exchanged, the simulation results will be the opposite (Fig. 3.23b). And there is no significant difference between the choice of conventional and inverted structures, if the electron and hole have equal mobilities (Fig. 3.23c). Furthermore, the differences between patterned inverted and conventional devices' efficiencies are larger in the case of greater difference between electron and hole mobilities (Fig. 3.26). These interesting results suggest that when patterning an OPV the mobilities must be considered to determine the optimal strucutre (inverted or conventional) for the material. One should apply the inverted structure to improve preserve carrier collection when patterning OPVs, if the hole is tested to be the slower carrier (Chapter 2).

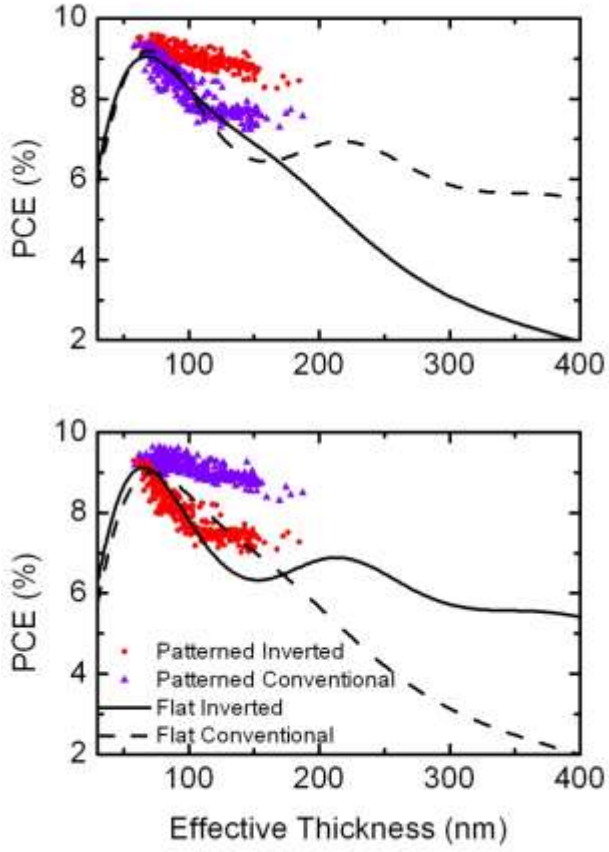

Figure 3.26 Simulations of the inverted devices (ITO/PFN/PTB7:$PC_{70}BM$/WO_3/Ag) and conventional (ITO/WO_3/PTB7:$PC_{70}BM$/PFN/Ag). Black solid and dash lines are the flat inverted and conventional devices respectively. Red dots are the patterned inverted devices and violet dots are the patterned conventional devices. a) Electron mobility is one order of magnitude greater than hole mobility $\mu_n = 1.7\times10^{-7}$ m^2/V s, $\mu_p = 1.7\times10^{-8}$ m^2/V s) b) Hole mobility is one order of magnitude greater than electron mobility ($\mu_n = 1.7\times10^{-8}$ m^2/V s, $\mu_p = 1.7\times10^{-7}$ m^2/V s). Reprinted with permission from Ref. 126. Copy Right 2013, American Institute of Physics.

3.4 Morphology changes due to patterning

Besides the internal electric field non-uniform distribution, the inability of patterned devices to significantly outperform champion non-patterned cells also likely resulted from modifications in the BHJ morphology that occurs during the patterning process. Aspects of the nanoscale morphology including polymer:fullerene compositional

variations and polymer crystallinity are known to be critical in non-patterned devices and could be potentially altered during pattern formation. Results from scanning transmission X-ray microscopy (STXM) shows that 200 nm diameter patterned posts have a higher concentration of $PC_{60}BM$ than the "flash" layer (the flat part in the patterned blend) that connects adjacent posts. Not only does this occur at elevated imprinting temperatures, but it also occurs when patterning at room temperature in the presence of a saturated solvent atmosphere.

Patterns of regio-regular P3HT:$PC_{60}BM$ blends were fabricated using PRINT[119] with an elastomeric molding material based on perfluoropolyether (PFPE). Fig. 3.27 shows patterns of P3HT:$PC_{60}BM$ made using the PRINT technique imaged using both atomic force microscopy (AFM) and scanning electron microscopy (SEM). A hexagonal lattice of posts is formed with a nearest neighbour periodicity of 400 nm and post diameter of 200 nm. Connecting each of the posts is a "flash" layer as labelled in Fig. 3.27c. During the patterning process, the PFPE mold is pressed into a spuncast P3HT:$PC_{60}BM$ film under elevated temperature or in the presence of a saturated solvent atmosphere.

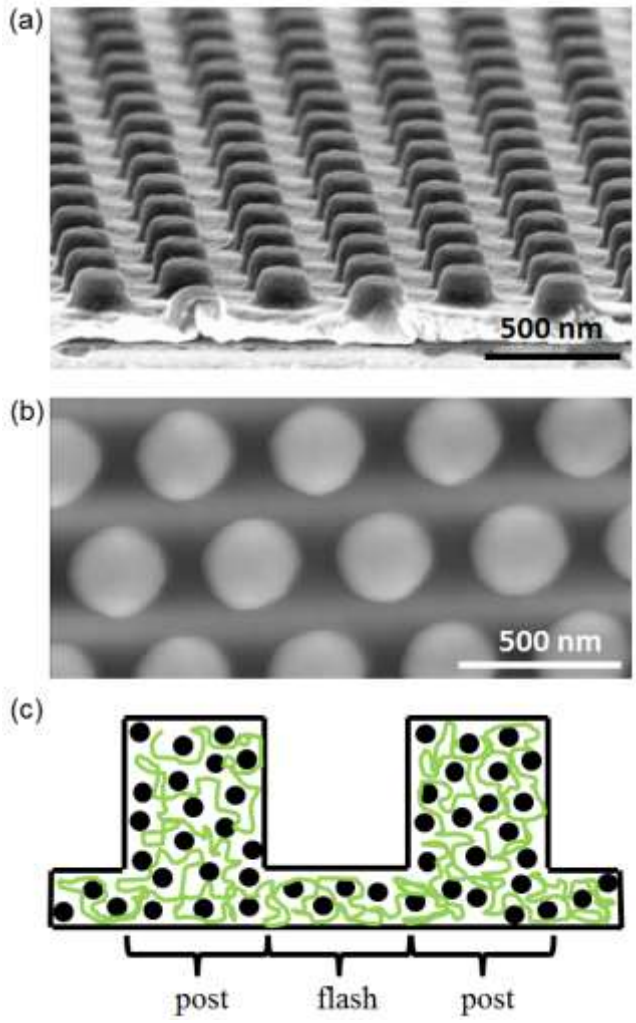

Figure 3.27 (a) SEM and (b) AFM images of patterned RReg P3HT:PCBM photoactive layer. The patterns are comprised of posts spaced by 400 nm in a hexagonal array with 200 nm diameters. Adjacent posts are connected by a residual flash layer as shown in (c) where P3HT polymer chains are green and PCBM molecules are black spheres (not to scale).

Even though very good pattern uniformity is obtained, characterization techniques such as SEM and AFM are not sensitive to the internal morphology of the posts or flash layer. For example, patterning the BHJ blend could cause nonuniformities to arise in terms of composition of P3HT and $PC_{60}BM$. For example, there could still be unintentional preferential migration of one component leading to compositional

differences, though the surface energy of the PFPE stamp is very low. To address this possibility, composition is measured using scanning transmission x-ray microscopy (STXM) utilizing the near edge X-ray absorption fine structure (NEXAFS) spectra of P3HT and $PC_{60}BM$ that have unique spectral features near the carbon 1s absorption edge. This technique has been previously employed to measure absolute composition of $PC_{60}BM$ in P3HT films[138,139] and can resolve features below 50 nm. The combination of microscopy and material sensitivity makes it an excellent technique to assess compositional differences in patterned samples with sub-micron scale features. Fig 3.28a shows optical absorbance of a nanopatterned sample for 284.4 eV incident photon energy. The black area on the right side of the image is an area with no sample, so the incident photon flux can be simultaneously measured to obtain the optical absorbance. Individual posts are clearly resolved with the same feature size and spacing as observed in the SEM image (Fig 3.27a). Differences in optical absorbance are a combination of two effects dictated by the Beer-Lambert law. First, thickness differences between the posts and the flash layer will change the absorbance and second, compositional variations will also lead to absorbance differences depending on the photon energy. The average absorbance is determined separately for posts and regions of the flash layer that are post-free using masks based on histograms of detector counts (Fig. 3.28b). It should be noted that the STXM measurement is done in transmission, so any vertical composition variations will be averaged.

Since a single energy is not enough to distinguish between thickness and compositional differences, ~40 images with different photon energies were acquired to produce average absorbance spectra that represent the post areas and flash layer,

respectively. These spectra are shown in Fig. 3.29 for three different nanoimprinting temperatures. Also shown in Fig. 3.29b are the measured pure material NEXAFS reference spectra of P3HT and $PC_{60}BM$, which reveal the unique spectral fingerprints of each material. Near the absorption edge, the spectra are very different, while well above the edge (e.g., 320 eV), the intrinsic absorption of P3HT and $PC_{60}BM$ is similar. Differences in the measured post and flash spectra for each imprinting temperature are noted especially near the $PC_{60}BM$ absorption peak (~284 eV) where the absorbance is greater for the posts than for the flash layers in all samples. Using the pure material spectra, the absorbance data are fit using an overall scaling factor to account for thickness variations along with a weighted linear combination of the reference spectra following previous methods.[140] Fits are achieved that capture the essential features of the data. As a check, measurement of a non-patterned, planar P3HT:$PC_{60}BM$ film resulted in a $PC_{60}BM$ weight percentage of 42.4%, which is close to the nominal 44.4% expected from the 1:0.8 wt. ratio solution used. It should also be noted that the P3HT pure material reference spectrum used in the fits was acquired from a spuncast film pressed with a featureless (i.e., flat) PFPE mold and is different than a spectrum from a standard spuncast only film. Using either spectrum does not significantly alter the fitted values, but a better fit is achieved using the spectrum corresponding to the pressed P3HT. Finally, an anisotropy factor that accounts for polymer orientational differences is also used in the fit, following previous protocols for fitting P3HT:$PC_{60}BM$ composition.[139]

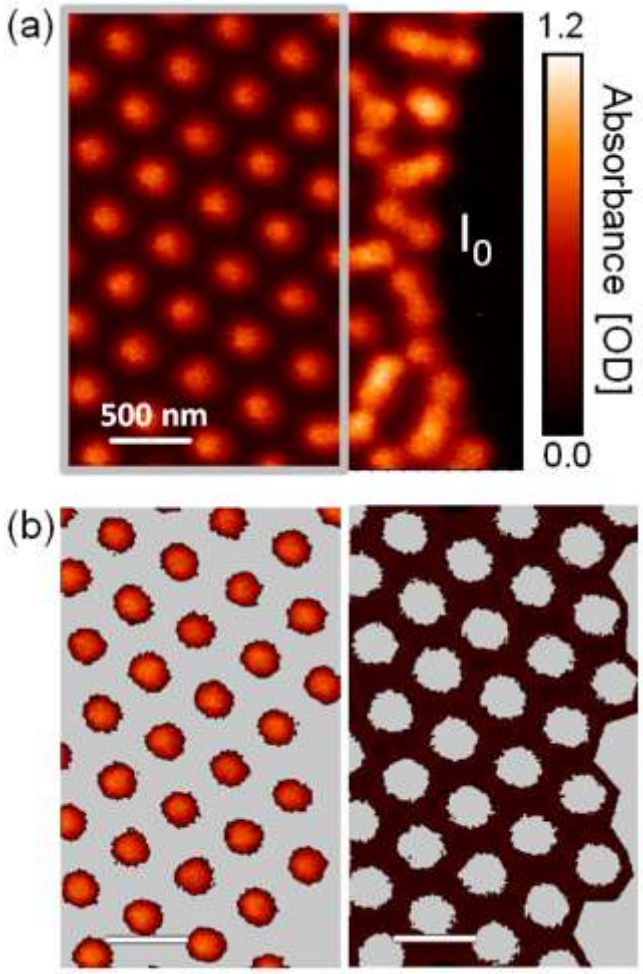

Figure 3.28 (a) Absorbance of photoactive nanopattern for 284.4 eV incident photon energy taken with STXM. Within the image area, a region without nanopattern is used to simultaneously measure the incident photon flux, I_0. (b) Masks that isolate posts (left) and flash (right) are used to determine the average absorbance in the posts and flash layer, respectively.

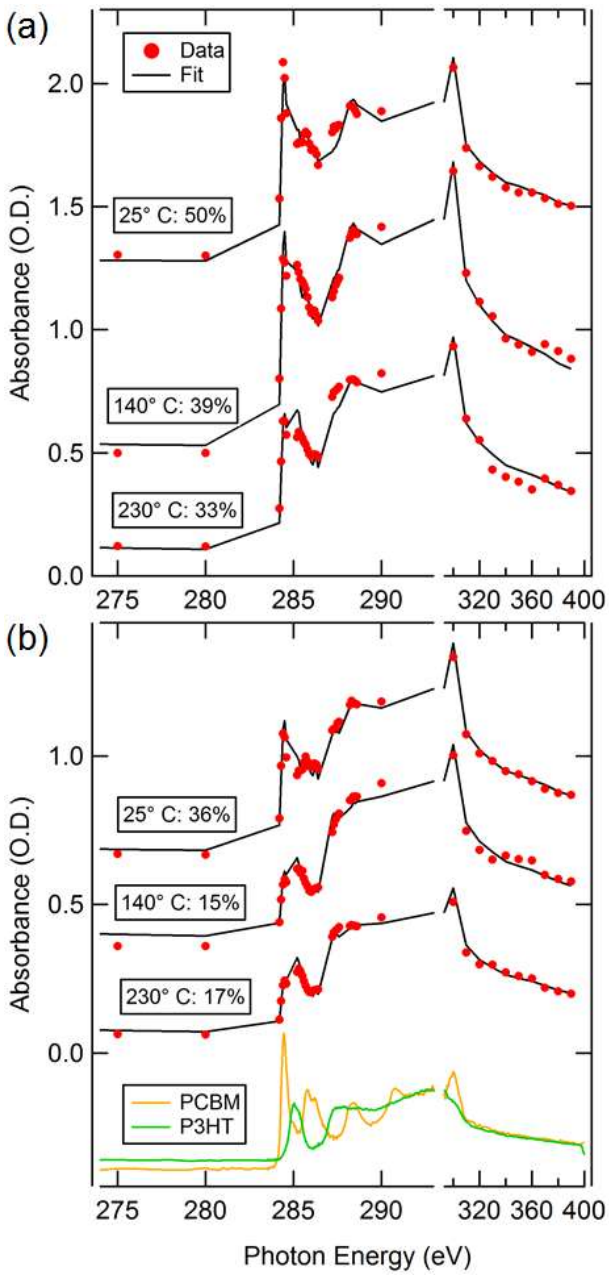

Figure 3.29 Measured absorbance and composition fits for (a) post areas and (b) exposed flash layer for nanopatterns imprinted at different temperatures. Absorbance for each energy corresponds to a separate image using the masking technique described in Fig. 3.27. For all temperatures, there is higher $PC_{60}BM$ percentage by weight in the posts than in the flash layer as labeled. This leads to flash layer composition that is below the optimum for high performance. The spectra for 140 °and 25 ℃ are vertically offset for clarity. Pure material NEXAFS reference spectra for P3HT and $PC_{60}BM$ with unique spectral fingerprints are also shown in (b).

The fits in Fig. 3.29 reveal that the content of $PC_{60}BM$ in the posts is twice the amount by weight than in the flash layer for the nanopattern produced under standard processing conditions at 140 ℃. Furthermore, given the nominal value of $PC_{60}BM$ of 44% based on the solution weight ratio, it is apparent that some $PC_{60}BM$ is removed during the nanoimprinting process. This leaves the composition in the flash layer much lower than the optimum range for high performance between 40-50% $PC_{60}BM$.[141,142] The amount of loss decreases with decreasing temperature and is the least for samples imprinted at room temperature using a saturated solvent atmosphere. We hypothesize that the $PC_{60}BM$ is transferred to the mold, which is a function of temperature. Interestingly, there are still compositional differences between the posts and flash layer even when imprinting without elevated temperature. However, the composition remains nearly inside the range of optimum composition for high performance and should not be detrimental.

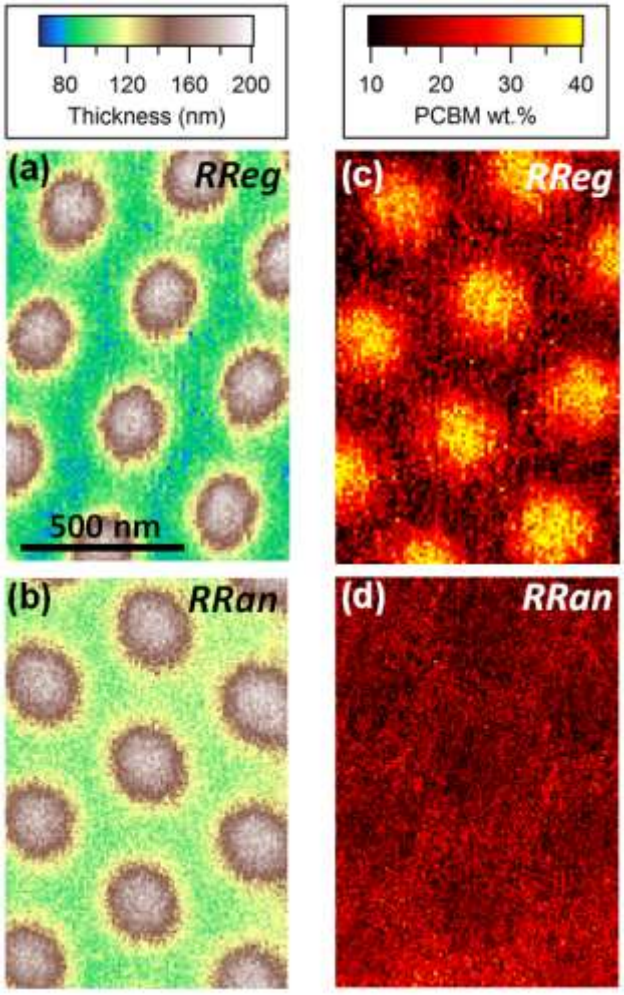

Figure 3.30 (a,b) Thickness and (c,d) composition maps derived from STXM measurements of nanopatterns comprised of $PC_{60}BM$ and (a,c) RReg P3HT and (b,d) RRan P3HT. Both nanopatterns are fabricated at 140 ℃. The composition differences between the posts and the flash layer are minimal in the nanopattern made with amorphous RRan P3HT compared to the nanopattern made with semicrystalline RReg P3HT.

These results are unexpected and reveal that the composition can differ substantially across nanopatterned photoactive layers. Along with the nanoimprinting temperature, the extent of compositional heterogeneity is potentially related to the material properties of the chosen polymer and fullerene. To test the influence of polymer crystallinity in particular, nanopatterns were fabricated using a BHJ film of highly amorphous RRan

P3HT with $PC_{60}BM$ at 140 ℃. Thickness and composition maps are displayed in Fig. 3.30, comparing nanopatterns made with RRan P3HT to those made with RReg P3HT. The maps are calculated using two STXM images with different energy (284.4 eV and 320 eV in this case) following previous methodology.[143] The thickness maps reveal similar feature height, size, and spacing for both RReg and RRan P3HT:$PC_{60}BM$ nanopatterns (Fig. 3.30a,b), supporting the effectiveness of the PRINT technique regardless of material choice. However, in terms of composition, the RReg P3HT:$PC_{60}BM$ pattern (Fig. 3.30c) exhibits differences between the posts and flash layer, in agreement with the fits in Fig. 3.29. On the other hand, the composition map for the RRan P3HT:$PC_{60}BM$ nanopattern (Fig. 3.30d) shows minimal composition differences between the posts and flash layer. While there is still some $PC_{60}BM$ mass loss during nanoimprinting, there is not a drastic compositional difference between the posts and flash layer like for the RReg P3HT:$PC_{60}BM$ nanopattern. This was also the case when imprinting at other temperatures with RRan P3HT (data not shown here). These results indicate that RRan P3HT is not as susceptible to composition variations during the nanoimprinting process.

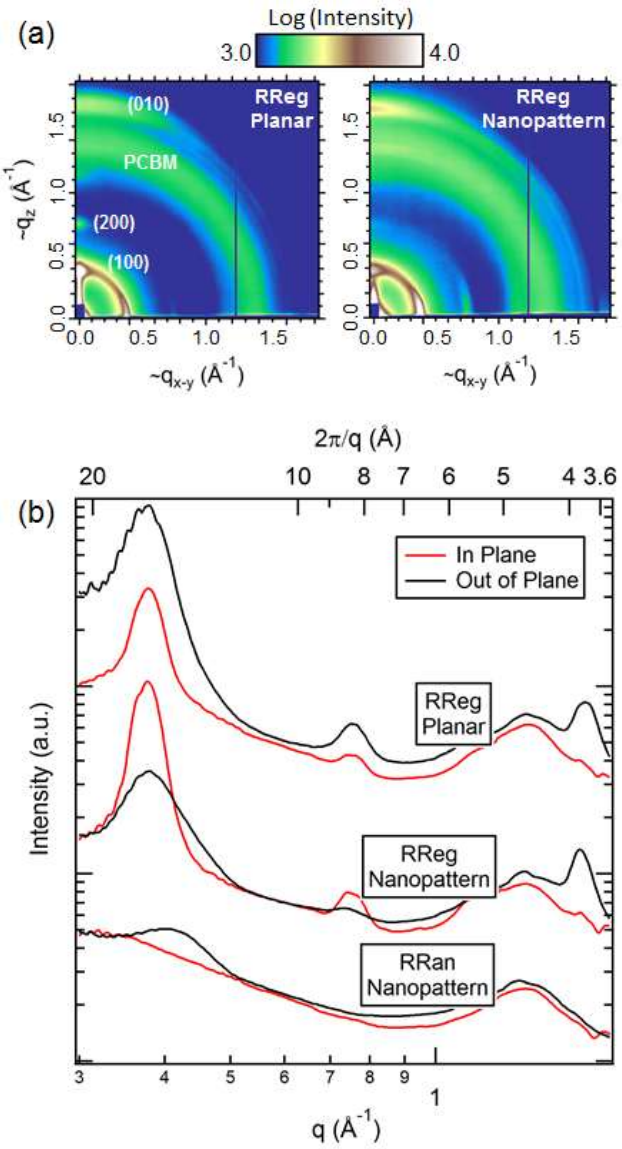

Figure 3.31 GIWAXS scattering data for (a) non-patterned, planar RReg P3HT:$PC_{60}BM$ and RReg P3HT:$PC_{60}BM$ nanopatterned samples, with the important peaks labeled. (b) In plane and out of plane sector averages reveal that nanoimprinting causes P3HT crystals to become more face-on with respect to the substrate compared to the non-patterned planar film. Sector averages are also shown for the RRan P3HT:$PC_{60}BM$ nanopatterned sample that lacks crystal reflections. It should be noted that (a) are not corrected for the missing wedge in the out of plane direction making the axes approximate.

The primary difference between RReg P3HT and RRan P3HT is their tendency, or lack thereof, to crystallize. RRan P3HT is highly amorphous, while RReg P3HT readily

crystallizes. The differences in crystallinity were assessed with grazing incidence wide angle X-ray scattering (GIWAXS) conducted at Beamline 7.3.3 of the Advanced Light Source.[144] Fig. 3.31 shows an absence of P3HT crystal peaks for the RRan P3HT:$PC_{60}BM$ nanopattern as expected, while the RReg P3HT:$PC_{60}BM$ nanopattern exhibits P3HT crystallite reflections in both the lamellar (h00) and π-π stacking (0k0) directions. RReg P3HT is a highly semicrystalline material for which the crystallization dynamics play an important role in influencing the morphological development of BHJ blends.[145,146] The crystallization of P3HT also plays an important role in the compositional measurements shown in Fig. 3.29 and Fig. 3.30. We rationalize the observations as follows. The crystallization of RReg P3HT makes this material very immobile compared to dispersed $PC_{60}BM$ molecules that can move freely, especially at elevated temperature.[147] The RReg P3HT crystals thus form a rigid matrix during the nanoimprinting process where the crystallites are unable to fill the mold voids effectively, leaving them open to excess $PC_{60}BM$ infiltration.

Also noted from Fig. 3.31 are differences in the diffraction between a non-patterned, planar RReg P3HT:$PC_{60}BM$ thin film and a nanopatterned one. The planar film has more intense lamellar reflections in the out of plane direction (~q_z) compared to in plane (~q_{x-y}) as expected.[34] On the other hand, the nanopatterned sample has higher intensity lamellar reflections in the in plane compared to the out of plane direction. This indicates a reorientation of P3HT crystallites to be comparatively more face-on with respect to the substrate with nanoimprinting. In other words, a higher proportion of polymer crystallites are oriented with side chains parallel to the substrate for the patterned sample compared to the non-patterned control. The fraction of P3HT near the mold interface in the posts

likely increases the face-on signal. Reorientation of P3HT crystallites in nanopatterns based solely on RReg P3HT has been recently reviewed,[148] where an enhancement in face-on population as observed here was previously shown in nanogratings of P3HT.[149] A higher population of face-on crystallites with out of plane π-π stacking could improve vertical charge transport[150] for nanoimprinted blends, but this benefit would compete against the negative impact of the compositional heterogeneities discussed above.

3.5 Conclusion

To summarize, a simple, low cost, scalable scheme for fabricating nano-structured solar cells by NIL was demonstrated. Compared with imprinting the active layer, this method appears easier to adapt to most OPV systems. Clear photonic effects were shown and agreed with simulations. Flat and patterned devices were compared from both optical and electrical perspectives. Highly efficient P3HT:PC_{60}BM-based OPV devices were obtained in both flat and patterned devices, although no significant enhancement from the nanostructured devices was noted.

By an electro-photonic model, the performances of flat and patterned grating electrodes in OPV devices were simulated. Optimized 2D grating structures for the active layer patterning are proposed. Additionally, we discussed the tradeoff between light trapping enhancement and charge carrier transport deterioration induced by nanostructures. The nanostructure may not only weaken the local electric field, but also may change the generation profile inside the active layer and hence affect the distance of the free carriers from the electrodes. These effects demonstrated that mere light absorption improvement by patterning devices is not sufficient. The total enhancement is a combination of all electrical and optical effects. Moreover, these results provide

guidance on the choice of polarity of electron/hole current flows in inverted or conventional device structures. There is a greater chance to improve devices' efficiencies in the patterned inverted structures when the hole transport is slower.

At last, the effects to morphology from nano-imprinting were explored. The nanoimprinting submicron features in highly crystalline materials, such as RReg P3HT:$PC_{60}BM$, results in compositional heterogeneity which, in turn, has negative consequences for solar cell efficiency. The compositional differences between the posts and flash layer can be mitigated by using a highly amorphous polymer, such as PTB7. On the other hand, if a highly crystalline polymer is used, like RReg P3HT, then nanoimprinting should be conducted at room temperature. If the induced compositional variations are within the range corresponding to high performance, then there is the potential added benefit of higher mobility in the direction of charge transport due to a greater population of polymer crystals taking a face-on orientation with respect to the substrate.

CHAPTER 4
CONCLUSION AND OUTLOOK

4.1 Why This Thesis is Important

The demand for energy increases every year. The undesirable environmental and climatic consequences from burning fossil fuels, coupled with high oil prices and increasing government supports are driving renewable energy legislation, incentives and commercialization. Solar energy has been considered as one of the most important and promising clean energy technologies. However, to further replace the fossil fuels, increasing efficiency and reducing the cost of manufacturing are crucial for the future commercialization of photovoltaics (solar cells). The major challenge in solar cell technology has been recognized as achieving an efficient absorption of photons with a minimized charge carrier transport losses.

Nanostructures have been proposed to counteract the charge transport losses in a variety of types of solar cells.[10,48,49,151–154] While working to understand the impact of nanostructures on the charge carrier collection, a better description of device performance was first required for a planar cell. One contribution of this thesis is development of a simple method to measure the charge carrier transport length in photovoltaic devices. While field effect transistor (FET) and space charge limited current (SCLC) diode methods have been widely used before, they each have negative aspects. The FET

measurements are parallel to the plane of the film, while both methods involve injecting charges from the contacts in the dark. However, the carriers in working solar cells carriers transport perpendicularly to the plane of the film and are extracted due to photo generation under illumination. In this thesis, the optical absorption profiles in the active layers were utilized to probe charge carrier transports in photovoltaic devices. By this method, the electron transport length was estimated to be ~400 nm in electrodeposited Cu_2O, which must be considered for designing nanostructures in this kind of solar cells. Similar approach was applied to three different BHJ OPV systems and the restrict carrier in each system is identified and the relation between charge transport distance and recombination were discussed as well. Furthermore, with this technique adapted in the conventional transient photocurrent measurement, a two carrier transport process was clearly demonstrated and estimations of electron and hole mobilities were obtained.

Besides the fundamental investigations on physics of charge carrier transport, effects of nanostructures were studied in organic photovoltaic devices. A simple nano-imprinting technique was developed and it is able to be applied to many photovoltaic systems other than OPVs only. High efficient nanostructured P3HT:PC_{60}BM solar cells (>4%) were demonstrated. However, an overall enhancement of efficiency was not observed when compared to the most efficient flat device fabricated, although clear optical improvement is achieved. This drew our attention to the theoretically understanding of impacts of nanostructures to OPVs by applying an electro-photonic simulation tool. The tradeoff between optical absorption improvement and charge carrier collection deterioration was explored. We demonstrated the power and importance of comprehensive electronic-photonic simulation in the optimization of nanostructured OPV. Impact of patterning

process to the composition configuration inside the BHJ OPV was also discussed as another important factor that kept the patterned RReg P3HT OPVs from outperforming the most efficient flat device. And we suggested that possible improvement could be achieved by patterning amorphous material at low temperature.

4.2 Look Forward

4.2.1 Device Physics

In conjunction with a more thorough understanding of fundamental physics, device performances of all kinds of solar cells will continue to progress. The goal of high performance will be guided by a thorough and detailed description of electro-optical process in each type of the solar cell. For instance, there is currently an extensive debate on the voltage dependence of the free carrier generation in BHJ Organic solar cells.[18,19,93,155–158] Even though the precise mechanisms are still being resolved, the field dependence of the photocurrent is widely accepted. Application of larger electric fields inevitably extracts more photocurrent. Novel techniques to enhance the electric field may continue to be demonstrated in the future as a route to boost OPV performance.

Furthermore, with the advance of material engineering, the probing of new material transport properties becomes important and necessary. Although a wide variety of mobility and life-time measurement techniques are available, the pursuite of measuring device under close to the real operating conditions does not stop.[159] The characteristic absorption profile has been demonstrated to be important in measuring free carrier transport and collection process. It should be more developed and incorporated with other techniques in probing the charge carrier transport properties in all kinds of devices, especially in the devices with novel structures (i.e. tandem) or materials.

4.2.2 Application of Nanostructures

As demonstrated in this thesis, photovoltaic devices will not benefit most from nanostructures without carefully considering both optical and electrical effects. With the advances in understanding device physics and precise characterization of charge carrier transport process, optimal nanostructure will be achieved. The total enhancement by photonic nanostructures in PTB7 OPV is demonstrated less than 10%, due to its intrinsic great absorption and short transport length. However, we should not ignore the potential of nanostructures in photovoltaic devices. Organic photovoltaic devices have been demonstrated to have FF greater than 0.5 with thicknesses up to 1 um.[98] On the other hand, the PbS quantum dot solar cell with a broad absorption band (from ~400 nm to ~1400 nm) reached the power conversion efficiency of 5.2% with only ~50% of absorption across most of the regime.[160] Utilization of photonic nanostructures in materials with either superior transport or broad absorption band but relative weak absorption or both will definitely be promising.

References

[1] T. New, P. Scenario, N.P. Scenario, M. East, F. Daiichi, U. States, T.U. States, F. Us, and N. America, *WORLD ENERGY OUTLOOK 2012 FACTSHEET* (2012).

[2] M.A. Green, K. Emery, Y. Hishikawa, and W. Warta, Progress in Photovoltaics: Research and Applications **18**, 346 (2010).

[3] N.S. Lewis, Science (New York, N.Y.) **315**, 798 (2007).

[4] C. Wadia, A.P. Alivisatos, and D.M. Kammen, Environmental Science & Technology **43**, 2072 (2009).

[5] D.-H. Ko, J.R. Tumbleston, A. Gadisa, M. Aryal, Y. Liu, R. Lopez, and E.T. Samulski, Journal of Materials Chemistry **21**, 16293 (2011).

[6] M. Izaki, T. Shinagawa, K.-T. Mizuno, Y. Ida, M. Inaba, and A. Tasaka, Journal of Physics D: Applied Physics **40**, 3326 (2007).

[7] J.J. LOFERSKI, Journal of Applied Physics **27**, 777 (1956).

[8] Y. Liu, H.K. Turley, J.R. Tumbleston, E.T. Samulski, and R. Lopez, Applied Physics Letters **98**, 162105 (2011).

[9] K.P. Musselman, A. Marin, L. Schmidt-Mende, and J.L. MacManus-Driscoll, Advanced Functional Materials **22**, 2202 (2012).

[10] K.P. Musselman, A. Wisnet, D.C. Iza, H.C. Hesse, C. Scheu, J.L. MacManus-Driscoll, and L. Schmidt-Mende, Advanced Materials **22**, E254 (2010).

[11] C.W. Tang, Applied Physics Letters **48**, 183 (1986).

[12] G. Yu, J. Gao, J.C. Hummelen, F. Wudl, and A.J. Heeger, Science **270**, 1789 (1995).

[13] J.J.M. Halls, C.A. Walsh, N.C. Greenham, E.A. Marseglia, R.H. Friend, S.C. Moratti, and A.B. Holmes, Nature **376**, 498 (1995).

[14] G. Li, V. Shrotriya, J. Huang, Y. Yao, T. Moriarty, K. Emery, and Y. Yang, Nat. Mater. **4**, 864 (2005).

[15] Z. He, C. Zhong, S. Su, M. Xu, H. Wu, and Y. Cao, Nature Photonics **6**, 591 (2012).

[16] J.R. Tumbleston, D.-H. Ko, E.T. Samulski, and R. Lopez, Phys. Rev. B **82**, 205325 (2010).

[17] V.D. Mihailetchi, H. Xie, B. de Boer, L.J.A. Koster, and P.W.M. Blom, Adv. Funct. Mater. **16**, 699 (2006).

[18] F.C. Jamieson, T. Agostinelli, H. Azimi, J. Nelson, and J.R. Durrant, J. Phys. Chem. Lett. **1**, 3306 (2010).

[19] S.R. Cowan, N. Banerji, W.L. Leong, and A.J. Heeger, Advanced Functional Materials **22**, 1116 (2012).

[20] C.L. Braun, The Journal of Chemical Physics **80**, 4157 (1984).

[21] L.J.A. Koster, E.C.P. Smits, V.D. Mihailetchi, and P.W.M. Blom, Physical Review B **72**, 085205 (2005).

[22] F. Biccaria, C. Malerbaa, and A. Mittigaa, Solar Energy Materials and Solar Cells **94**, 1947 (2010).

[23] L. Onsager, Phys. Rev. **54**, 554 (1904).

[24] C.L. Braun, The Journal of Chemical Physics **80**, 4157 (1984).

[25] A. A. Bakulin, J.C. Hummelen, M.S. Pshenichnikov, and P.H.M. van Loosdrecht, Advanced Functional Materials **20**, 1653 (2010).

[26] F. Zhang, K.G. Jespersen, C. Björström, M. Svensson, M.R. Andersson, V. Sundström, K. Magnusson, E. Moons, a. Yartsev, and O. Inganäs, Advanced Functional Materials **16**, 667 (2006).

[27] K.G. Jespersen, F. Zhang, A. Gadisa, V. Sundström, A. Yartsev, and O. Inganäs, Organic Electronics **7**, 235 (2006).

[28] M. Tong, N.E. Coates, D. Moses, A.J. Heeger, S. Beaupré, and M. Leclerc, Physical Review B **81**, 125210 (2010).

[29] I.-W. Hwang, C. Soci, D. Moses, Z. Zhu, D. Waller, R. Gaudiana, C.J. Brabec, and A. J. Heeger, Advanced Materials **19**, 2307 (2007).

[30] I.-W. Hwang, J. Young Kim, S. Cho, J. Yuen, N. Coates, K. Lee, M. Heeney, I. McCulloch, D. Moses, and a. J. Heeger, Journal of Physical Chemistry C **112**, 7853 (2008).

[31] C.J. Brabec, G. Zerza, G. Cerullo, S. De Silvestri, S. Luzzati, J.C. Hummelen, and S. Sariciftci, **340**, 232 (2001).

[32] P.E. Shaw, A. Ruseckas, and I.D.W. Samuel, Advanced Materials **20**, 3516 (2008).

[33] A.J. Lewis, A. Ruseckas, O.P.M. Gaudin, G.R. Webster, P.L. Burn, and I.D.W. Samuel, Organic Electronics **7**, 452 (2006).

[34] A.J. Parnell, A.J. Cadby, O.O. Mykhaylyk, A.D.F. Dunbar, P.E. Hopkinson, A.M. Donald, and R.A.L. Jones, Macromolecules **44**, 6503 (2011).

[35] B. Walker, A.B. Tamayo, X.-D. Dang, P. Zalar, J.H. Seo, A. Garcia, M. Tantiwiwat, and T.-Q. Nguyen, Advanced Functional Materials **19**, 3063 (2009).

[36] J.S. Moon, C.J. Takacs, S. Cho, R.C. Coffin, H. Kim, G.C. Bazan, and A.J. Heeger, Nano Letters **10**, 4005 (2010).

[37] M. Dante, A. Garcia, and T.-Q. Nguyen, The Journal of Physical Chemistry C **113**, 1596 (2009).

[38] T. Erb, U. Zhokhavets, G. Gobsch, S. Raleva, B. Stühn, P. Schilinsky, C. Waldauf, and C.J. Brabec, Advanced Functional Materials **15**, 1193 (2005).

[39] D. Chen, A. Nakahara, D. Wei, D. Nordlund, and T.P. Russell, Nano Letters **11**, 561 (2011).

[40] W. Ma, C. Yang, X. Gong, K. Lee, and A.J. Heeger, Advanced Functional Materials **15**, 1617 (2005).

[41] N.C. Cates, R. Gysel, Z. Beiley, C.E. Miller, M.F. Toney, M. Heeney, I. McCulloch, and M.D. McGehee, Nano Letters **9**, 4153 (2009).

[42] D.-H. Ko, J.R. Tumbleston, L. Zhang, S. Williams, J.M. DeSimone, R. Lopez, and E.T. Samulski, Nano Letters **9**, 2742 (2009).

[43] M. Niggemann, M. Glatthaar, A. Gombert, A. Hinsch, and V. Wittwer, Thin Solid Films **451-452**, 619 (2004).

[44] X. Li, W.C.H. Choy, L. Huo, F. Xie, W.E.I. Sha, B. Ding, X. Guo, Y. Li, J. Hou, J. You, and Y. Yang, Advanced Materials **24**, 3046 (2012).

[45] L. Müller-Meskamp, Y.H. Kim, T. Roch, S. Hofmann, R. Scholz, S. Eckardt, K. Leo, and A.F. Lasagni, Advanced Materials **24**, 906 (2012).

[46] K.-Y. Yang, K.-M. Yoon, S. Lim, and H. Lee, Journal of Vacuum Science & Technology B: Microelectronics and Nanometer Structures **27**, 2786 (2009).

[47] K.S. Nalwa, J.-M. Park, K. Ho, and S. Chaudhary, Advanced Materials (Deerfield Beach, Fla.) **23**, 112 (2011).

[48] F. Zhang, T. Song, and B. Sun, Nanotechnology **23**, 194006 (2012).

[49] S.A. Moiz, A.M. Nahhas, H.-D. Um, S.-W. Jee, H.K. Cho, S.-W. Kim, and J.-H. Lee, Nanotechnology **23**, 145401 (2012).

[50] D.H. Wang, J. Seifter, J.H. Park, D.-G. Choi, and A.J. Heeger, Advanced Energy Materials **2**, 1319 (2012).

[51] S. Mokkapati and K.R. Catchpole, Journal of Applied Physics **112**, 101101 (2012).

[52] P. Vukusic and J.R. Sambles, Nature **424**, 852 (2003).

[53] P. Vukusic, J.R. Sambles, and C.R. Lawrence, Proceedings. Biological Sciences / The Royal Society **271 Suppl** , S237 (2004).

[54] P. Taylor, S.J. Wilson, and M.C. Hutley, Optica Acta: International Journal of Optics **29**, 993 (1982).

[55] S. Kinoshita and S. Yoshioka, Chemphyschem : a European Journal of Chemical Physics and Physical Chemistry **6**, 1442 (2005).

[56] J.R. Tumbleston, Y. Liu, E.T. Samulski, and R. Lopez, Advanced Energy Materials **2**, 477 (2012).

[57] L.C. Olsen, F.W. Addis, and W. Miller, Solar Cells **7**, 247 (1982).

[58] W. GARTNER, Phys. Rev **116**, 84 (1959).

[59] S. Siidergren, A. Hagfeldt, and S. Lindquist, J. Phys. Chem. **98**, 5552 (1994).

[60] S.M. Sze, *Physics of Semiconductor Devices* (Wiley, New York, 1981), p. 802.

[61] S.-E. Lindquist, B. Finnström, and L. Tegnér, J. Electrochem. Soc **130**, 351 (1980).

[62] T.M. Clarke and J.R. Durrant, Chemical Reviews **110**, 6736 (2010).

[63] P.W.M. Blom, V.D. Mihailetchi, L.J. a. Koster, and D.E. Markov, Advanced Materials **19**, 1551 (2007).

[64] J.Y. Kim, S.H. Kim, H.-H. Lee, K. Lee, W. Ma, X. Gong, and a. J. Heeger, Advanced Materials **18**, 572 (2006).

[65] S.H. Park, A. Roy, S. Beaupre, S. Cho, N. Coates, J.S. Moon, D. Moses, M. Leclerc, K. Lee, and A.J. Heeger, Nat. Photonics **3**, 297 (2009).

[66] A.J. Moulé and K. Meerholz, Appl. Phys. B **92**, 209 (2008).

[67] L.J.A. Koster, V.D. Mihailetchi, H. Xie, and P.W.M. Blom, Applied Physics Letters **87**, 203502 (2005).

[68] D.W. Sievers, V. Shrotriya, and Y. Yang, Journal of Applied Physics **100**, 114509 (2006).

[69] J.D. Kotlarski, P.W.M. Blom, L.J. A. Koster, M. Lenes, and L.H. Slooff, Journal of Applied Physics **103**, 084502 (2008).

[70] A. Maurano, R. Hamilton, C.G. Shuttle, A.M. Ballantyne, J. Nelson, B. O'Regan, W. Zhang, I. McCulloch, H. Azimi, M. Morana, C.J. Brabec, and J.R. Durrant, Adv. Mater. **22**, 4987 (2010).

[71] D. Credgington, R. Hamilton, P. Atienzar, J. Nelson, and J.R. Durrant, Advanced Functional Materials **21**, 2744 (2011).

[72] C.G. Shuttle, a. Maurano, R. Hamilton, B. O'Regan, J.C. de Mello, and J.R. Durrant, Applied Physics Letters **93**, 183501 (2008).

[73] W. Gaynor, G.F. Burkhard, M.D. McGehee, and P. Peumans, Adv. Mater. **23**, 2905 (2011).

[74] J.-Y. Lee, S.T. Connor, Y. Cui, and P. Peumans, Nano Letters **8**, 689 (2008).

[75] J. Huang, G. Li, and Y. Yang, Advanced Materials **20**, 415 (2008).

[76] J.-Y. Lee, S.T. Connor, Y. Cui, and P. Peumans, Nano Lett. **103**, 1276 (2010).

[77] T. Ameri, G. Dennler, C. Waldauf, H. Azimi, A. Seemann, K. Forberich, J. Hauch, M. Scharber, K. Hingerl, and C.J. Brabec, Adv. Funct. Mater. **20**, 1592 (2010).

[78] S. Nanowire, L. Hu, H.S. Kim, J. Lee, P. Peumans, and Y. Cui, **4**, 2955 (2010).

[79] S. Cowan, R. Street, S. Cho, and A. Heeger, Physical Review B **83**, 1 (2011).

[80] R. Street, S. Cowan, and A. Heeger, Physical Review B **82**, 11 (2010).

[81] R.A. Street, M. Schoendorf, A. Roy, and J.H. Lee, Physical Review B **81**, 1 (2010).

[82] M. Limpinsel, A. Wagenpfahl, M. Mingebach, C. Deibel, and V. Dyakonov, Phys. Rev. B **81**, 085203 (2010).

[83] V.D. Mihailetchi, L.J.A. Koster, J.C. Hummelen, and P.W.M. Blom, Phys. Rev. Lett. **93**, 216601 (2004).

[84] G.F. A. Dibb, T. Kirchartz, D. Credgington, J.R. Durrant, and J. Nelson, The Journal of Physical Chemistry Letters **2**, 2407 (2011).

[85] L.J.A. Koster, M. Kemerink, M.M. Wienk, K. Maturová, and R.A.J. Janssen, Adv. Mater. **23**, 1670 (2011).

[86] R.A. Street, K.W. Song, and S. Cowan, Org. Electron. **12**, 244 (2011).

[87] J.R. Tumbleston, D.-H. Ko, E.T. Samulski, and R. Lopez, Journal of Applied Physics **108**, 084514 (2010).

[88] C. Deibel, Phys. Status Solidi A **2736**, 2731 (2009).

[89] V. Mihailetchi, J. Wildeman, and P. Blom, Physical Review Letters **94**, 1 (2005).

[90] T.J.K. Brenner, Z. Li, and C.R. McNeill, The Journal of Physical Chemistry C **115**, 22075 (2011).

[91] V.D. Mihailetchi, L.J. a. Koster, P.W.M. Blom, C. Melzer, B. de Boer, J.K.J. van Duren, and R. a. J. Janssen, Advanced Functional Materials **15**, 795 (2005).

[92] K. Maturová, S.S. Van Bavel, M.M. Wienk, R.A.J. Janssen, and M. Kemerink, Nano Lett. **9**, 6 (2009).

[93] S. Cowan, A. Roy, and A.J. Heeger, Phys. Rev. B **82**, 245207 (2010).

[94] Z.E. Ooi, R. Jin, J. Huang, Y.F. Loo, a. Sellinger, and J.C. deMello, Journal of Materials Chemistry **18**, 1644 (2008).

[95] C.G. Shuttle, R. Hamilton, B.C. O'Regan, J. Nelson, and J.R. Durrant, Proc. Natl. Acad. Sci. **107**, 16448 (2010).

[96] K. Maturová, S.S. van Bavel, M.M. Wienk, R. a. J. Janssen, and M. Kemerink, Advanced Functional Materials **21**, 261 (2011).

[97] R. Mauer, I.A. Howard, and F. Laquai, Physiccal Chemistry Letters **2**, 1736 (2011).

[98] S.C. Price, A.C. Stuart, L. Yang, H. Zhou, and W. You, Journal of the American Chemical Society **133**, 4625 (2011).

[99] C.R. McNeill, I. Hwang, and N.C. Greenham, Journal of Applied Physics **106**, 024507 (2009).

[100] M.A. Loi, S. Toffanin, M. Muccini, M. Forster, U. Scherf, and M. Scharber, Advanced Functional Materials **17**, 2111 (2007).

[101] M. Hallermann, S. Haneder, and E. Da Como, Applied Physics Letters **93**, 053307 (2008).

[102] K. Vandewal, K. Tvingstedt, A. Gadisa, O. Ingan äs, and J. V Manca, Nature Materials **8**, 904 (2009).

[103] H. Kim, J.Y. Kim, S.H. Park, K. Lee, Y. Jin, J. Kim, and H. Suh, Applied Physics Letters **86**, 183502 (2005).

[104] L. Chen, W.E.I. Sha, and W.C.H. Choy, Optics Express **20**, 8175 (2012).

[105] C. Cocoyer, L. Rocha, C. Fiorini-Debuisschert, L. Sicot, D. Vaufrey, C. Sentein, B. Geffroy, and P. Raimond, Thin Solid Films **511-512**, 517 (2006).

[106] S.-I. Na, S.-S. Kim, J. Jo, S.-H. Oh, J. Kim, and D.-Y. Kim, Advanced Functional Materials **18**, 3956 (2008).

[107] K.S. Nalwa, J.-M. Park, K. Ho, and S. Chaudhary, Advanced Materials **23**, 112 (2011).

[108] M. Niggemann, M. Glatthaar, A. Gombert, A. Hinsch, and V. Wittwer, Thin Solid Films **451-452**, 619 (2004).

[109] M. Niggemann, M. Glatthaar, P. Lewer, C. Müller, J. Wagner, and a. Gombert, Thin Solid Films **511-512**, 628 (2006).

[110] B. Park, M. Kim, and Y. In Lee, Solar Energy Materials and Solar Cells **95**, 1141 (2011).

[111] M.-G. Kang, M.-S. Kim, J. Kim, and L.J. Guo, Advanced Materials **20**, 4408 (2008).

[112] D.H. Wang, J. Seifter, J.H. Park, D.-G. Choi, and A.J. Heeger, Advanced Energy Materials **2**, 1319 (2012).

[113] M.T. Dang, L. Hirsch, and G. Wantz, Advanced Materials **23**, 3597 (2011).

[114] D. Chen, W. Zhao, and T.P. Russell, ACS Nano **6**, 1479 (2012).

[115] X. He, F. Gao, G. Tu, D.G. Hasko, S. Hüttner, N.C. Greenham, U. Steiner, R.H. Friend, and W.T.S. Huck, Advanced Functional Materials **21**, 139 (2011).

[116] S. Rim, S. Zhao, S.R. Scully, M.D. McGehee, and P. Peumans, Applied Physics Letters **91**, 243501 (2007).

[117] Y. Yang, K. Lee, K. Mielczarek, W. Hu, and a Zakhidov, Nanotechnology **22**, 485301 (2011).

[118] W. Vervisch, G. Rivière, S. Vedraine, S. Biondo, P. Torchio, D. Duché, J.-J. Simon, and L. Escoubas, Journal of Applied Physics **111**, 094506 (2012).

[119] J.P. Rolland, B.W. Maynor, L.E. Euliss, A.E. Exner, G.M. Denison, and J.M. Desimone, Journal of American Chemical Society **127**, 10096 (2005).

[120] S. Han, W.S. Shin, M. Seo, D. Gupta, S.-J. Moon, and S. Yoo, Organic Electronics **10**, 791 (2009).

[121] S.G. Tikhodeev, A.L. Yablonskii, E.A. Muljarov, N.A. Gippius, and T. Ishihara, Physical Review B **66**, 1 (2002).

[122] G.F. Burkhard, E.T. Hoke, S.R. Scully, and M.D. McGehee, Nano Letters **9**, 4037 (2009).

[123] P.W.M. Blom, M.J.M. de Jong, and M.G. van Munster, Phys. Rev. B **5**, R656 (1997).

[124] F. Yakuphanoglu and R.S. Anand, Synthetic Metals **160**, 2250 (2010).

[125] L. Koster, E. Smits, V. Mihailetchi, and P. Blom, Physical Review B **72**, 1 (2005).

[126] Y. Liu, C.A. Tippets, C. Kirsch, E.T.S. Sorin Mitran, and R. Lopez, Journal of Applied Physics **113**, 244503 (2013).

[127] W. van Roosbroeck, Bell System Technical Journal **29**, 560 (1950).

[128] C. Kirsch and S. Mitran, J. Appl. Phys. (2012).

[129] Y. Liu, C. Kirsch, A. Gadisa, M. Aryal, S. Mitran, E.T. Samulski, and R. Lopez, Journal of Physics D: Applied Physics **46**, 024008 (2013).

[130] Y. Liang, Z. Xu, J. Xia, S.-T. Tsai, Y. Wu, G. Li, C. Ray, and L. Yu, Advanced **22**, E135 (2010).

[131] Z. He, C. Zhong, X. Huang, W.-Y. Wong, H. Wu, L. Chen, S. Su, and Y. Cao, Adv. Mater. **23**, 4636 (2011).

[132] C. Kirsch and S. Mitran, Journal of Applied Physics **112**, 054502 (2012).

[133] X.H. Li, W.E.I. Sha, W.C.H. Choy, D.D.S. Fung, and F.X. Xie, The Journal of Physical Chemistry C **116**, 7200 (2012).

[134] A. Gadisa, Y. Liu, E.T. Samulski, and R. Lopez, ACS Applied Materials & Interfaces **4**, 3846 (2012).

[135] C. Tao, S. Ruan, G. Xie, X. Kong, L. Shen, F. Meng, C. Liu, X. Zhang, W. Dong, and W. Chen, Applied Physics Letters **94**, 043311 (2009).

[136] K.S. Nalwa, J.-M. Park, K.-M. Ho, and S. Chaudhary, Advanced Materials **23**, 112 (2011).

[137] J. You, X. Li, F. Xie, W.E.I. Sha, J.H.W. Kwong, G. Li, W.C.H. Choy, and Y. Yang, Advanced Energy Materials **2**, 1203 (2012).

[138] B. Watts, W.J. Belcher, L. Thomsen, H. Ade, and P.C. Dastoor, Macromolecules **42**, 8392 (2009).

[139] B.A. Collins, E. Gann, L. Guignard, X. He, C.R. McNeill, and H. Ade, The Journal of Physical Chemistry Letters **1**, 3160 (2010).

[140] B.A. Collins and H. Ade, Journal of Electron Spectroscopy and Related Phenomena **185**, 119 (2012).

[141] A.J. Moulé, J.B. Bonekamp, and K. Meerholz, Journal of Applied Physics **100**, 094503 (2006).

[142] C. Müller, T.A.M. Ferenczi, M. Campoy-Quiles, J.M. Frost, D.D.C. Bradley, P. Smith, N. Stingelin-Stutzmann, and J. Nelson, Advanced Materials **20**, 3510 (2008).

[143] B.A. Collins, Z. Li, J.R. Tumbleston, E. Gann, C.R. McNeill, and H. Ade, Advanced Energy Materials **3**, 65 (2013).

[144] A. Hexemer, W. Bras, J. Glossinger, E. Schaible, E. Gann, R. Kirian, A. MacDowell, M. Church, B. Rude, and H. Padmore, Journal of Physics: Conference Series **247**, 012007 (2010).

[145] D. Chen, F. Liu, C. Wang, A. Nakahara, and T.P. Russell, Nano Letters **11**, 2071 (2011).

[146] B.A. Collins, J.R. Tumbleston, and H. Ade, Journal of Physical Chemistry Letters **2**, 3135 (2011).

[147] N.D. Treat, M.A. Brady, G. Smith, M.F. Toney, E.J. Kramer, C.J. Hawker, and M.L. Chabinyc, Advanced Energy Materials **1**, 82 (2011).

[148] Y. Yang, K. Mielczarek, M. Aryal, A. Zakhidov, and W. Hu, ACS Nano **6**, 2877 (2012).

[149] H. Hlaing, X. Lu, T. Hofmann, K.G. Yager, C.T. Black, and B.M. Ocko, ACS Nano **5**, 7532 (2011).

[150] H. Sirringhaus, P.J. Brown1, R.H. Friend, M.M. Nielsen, K. Bechgaard, B.M.W. Langeveld-Voss, A.J.H. Spiering, R.A.J. Janssen, E.W. Meijer, P. Herwig, and D.M. de Leeuw, Nature **401**, 685 (1999).

[151] H. Kim and K. Yong, Physical Chemistry Chemical Physics : PCCP **15**, 2109 (2013).

[152] M.-J. Jin, X.-Y. Chen, Z.-M. Gao, T. Ling, and X.-W. Du, Nanotechnology **23**, 485401 (2012).

[153] J.-H. Wu, S.-Y. Liu, S. Li, Y. Jiang, G.-P. Ru, and X.-P. Qu, Applied Physics A **109**, 489 (2012).

[154] Y. Yang, K. Mielczarek, M. Aryal, A. Zakhidov, and W. Hu, ACS Nano **6**, 2877 (2012).

[155] M. Mingebach, S. Walter, V. Dyakonov, and C. Deibel, Applied Physics Letters **100**, 193302 (2012).

[156] J. Kniepert, M. Schubert, J.C. Blakesley, and D. Neher, The Journal of Physical Chemistry Letters **2**, 700 (2011).

[157] R. Mauer, I.A. Howard, and F. Laquai, J. Phys. Chem. Lett. **2**, 1736 (2011).

[158] R.A. Marsh, J.M. Hodgkiss, and R.H. Friend, Advanced Materials **22**, 3672 (2010).

[159] A. Baumann, J. Lorrmann, D. Rauh, C. Deibel, and V. Dyakonov, Advanced Materials **24**, 4381 (2012).

[160] E.J.D. Klem, C.W. Gregory, G.B. Cunningham, S. Hall, D.S. Temple, and J.S. Lewis, Applied Physics Letters **100**, 173109 (2012).